THE INFLUENCE OF CATION DOPING ON THE ELECTRONIC PROPERTIES OF $SR_3RU_2O_7$
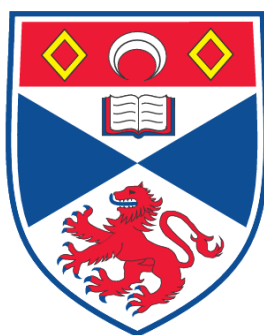
Jason Farrell

A Thesis Submitted for the Degree of PhD
at the
University of St. Andrews

2008

**Full metadata for this item is available in the St Andrews
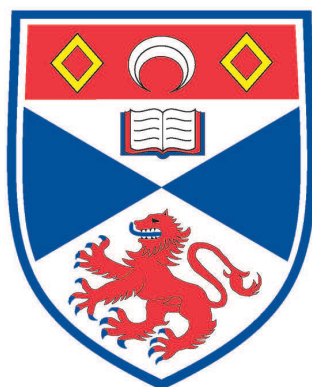Digital Research Repository
at:
https://research-repository.st-andrews.ac.uk/**

**Please use this identifier to cite or link to this item:
http://hdl.handle.net/10023/689**

The Influence of Cation Doping on the Electronic Properties of $Sr_3Ru_2O_7$

Jason Farrell

A thesis submitted for the degree of Doctor of Philosophy at the University of St Andrews

July 2008

Abstract

$Sr_3Ru_2O_7$ is a quasi-two-dimensional metal and has a paramagnetic ground state that is heavily renormalised by electron-electron correlations and magnetic exchange interactions. Inextricably linked to this renormalisation is the *metamagnetism* of $Sr_3Ru_2O_7$ – a rapid rise in uniform magnetisation over a narrow range of applied magnetic field. Knowledge of the zero-field physics is essential to any description of the metamagnetism. Light may be shed on the enigmatic ground state of $Sr_3Ru_2O_7$ by doping the crystal lattice with foreign cations: this is the primary purpose of the original research referred to this thesis, in which studies of some of the electronic properties of crystals of cation-doped $Sr_3Ru_2O_7$ are reported. Single crystals of $Sr_3(Ru_{1-x}Ti_x)_2O_7$ and $Sr_3(Ru_{1-x}Cr_x)_2O_7$ have been synthesised in an image furnace and some of the properties of these crystals have been measured. Evidence that indicates the emergence of a spin density wave as a function of Ti-doping in $Sr_3(Ru_{1-x}Ti_x)_2O_7$ is presented. Time-dependent magnetic irreversibility has been observed in samples of $Sr_3(Ru_{1-x}Cr_x)_2O_7$, thus hinting at the involvement of the RKKY mechanism in these materials. Regarding cation doping *out of* the conducting RuO_2 planes, samples of $(Sr_{1-y}La_y)_3Ru_2O_7$ have been grown and investigated. Both the Sommerfeld coefficient and the Fermi liquid A coefficient of $(Sr_{1-y}La_y)_3Ru_2O_7$ are found to decrease as a function of y ($0 \leq y \leq 0.02$); these observations point towards a reduction in the thermodynamic mass of the Landau quasiparticles. Results from magnetoresistance and magnetisation measurements indicate that the metamagnetism of the $(Sr_{1-y}La_y)_3Ru_2O_7$ series probably cannot be explained by a rigid band-shift model. Also, some aspects of these data imply that the metamagnetism cannot be fully accounted for by a spin fluctuation extension to the Ginzburg-Landau theory of uniform magnetisation.

Declarations

I, Jason Farrell, hereby certify that this thesis, which is approximately 35,000 words in length, has been written by me, that it is the record of work carried out by me and that it has not been submitted in any previous application for a higher degree.

date   signature of candidate

I was admitted as a research student in September 2004 and as a candidate for the degree of Doctor of Philosophy in September 2004; the higher study for which this is a record was carried out in the University of St Andrews between 2004 and 2007.

date   signature of candidate

I hereby certify that the candidate has fulfilled the conditions of the Resolution and Regulations appropriate for the degree of Doctor of Philosophy in the University of St Andrews and that the candidate is qualified to submit this thesis in application for that degree.

date   signature of supervisor

In submitting this thesis to the University of St Andrews I understand that I am giving permission for it to be made available for use in accordance with the regulations of the University Library for the time being in force, subject to any copyright vested in the work not being affected thereby. I also understand that the title and abstract will be published, and that a copy of the work may be made and supplied to any bona fide library or research worker, that my thesis will be electronically accessible for personal or research use, and that the library has the right to migrate my thesis into new electronic forms as required to ensure continued access to the thesis. I have obtained any third-party copyright permissions that may be required in order to allow such access and migration.

date   signature of candidate

Acknowledgements

Contents

3. Sr$_3$(Ru$_{1-x}$Ti$_x$)$_2$O$_7$

4. $Sr_3(Ru_{1-x}Cr_x)_2O_7$

5. $(Sr_{1-y}La_y)_3Ru_2O_7$

1. Introduction

1.1 Background and Motivation

Condensed matter physics is concerned with the macroscopic properties of systems in which the number of constituents is large. A *reductionist* approach to condensed matter physics tries to reconcile the macroscopic behaviour of a system with the microscopic behaviour of its constituent particles. A cornerstone of this reductionist point of view is the many-body Schrödinger equation, $\hat{H}\Psi = i\hbar\dfrac{d\Psi}{dt}$, where the Hamiltonian of the system is $\hat{H}$ and Ψ is the many-particle wavefunction. The Hamiltonian of a system of electrons and ion cores is

$$\hat{H} = -\sum_{j}^{N_e} \frac{\hbar^2}{2m}\nabla_j^2 - \sum_{\alpha}^{N_i} \frac{\hbar^2}{2M_\alpha}\nabla_\alpha^2 - \sum_{j}^{N_e}\sum_{\alpha}^{N_i} \frac{Z_\alpha e^2}{\left|\vec{r}_j - \vec{R}_\alpha\right|}$$
$$+ \sum_{\alpha<\beta}^{N_i} \frac{Z_\alpha Z_\beta e^2}{\left|\vec{R}_\alpha - \vec{R}_\beta\right|} + \sum_{j<k}^{N_e} \frac{e^2}{\left|\vec{r}_j - \vec{r}_k\right|},$$

(1.1)

where R and r refer to the spatial position of ions and electrons, respectively; the ionic and electronic masses are denoted by M and m; Z represents the ionic charges. The first two terms in Equation 1.1 refer to the kinetic energy of the electrons and ions, respectively. The electron-ion and ion-ion Coulomb interactions are accounted for by the third and fourth terms. The final term corresponds to Coulomb interactions between different electrons [1]. The motion of any individual electron is inextricably linked to the motion of every other electron in the system: the electrons are *correlated* with each other and are, therefore, a 'liquid' rather than a non-interacting 'gas' [2].

The Schrödinger equation becomes more difficult to solve as the number of particles in the system becomes large; the ground state of multi-electron atoms, for instance, cannot be deduced unless some approximations (such as screening) are considered [3]. Solving the Schrödinger equation for a macroscopic number of particles is, from a

technical point of view, a near-impossible task. However, it is often possible for condensed matter to arrange into macroscopic states which cannot be predicted from a reductionist approach: such self-organisation is known as *emergence* [1]. Dagotto [4] states that the hallmark of emergent physics is the "*generation of properties that do not preexist in a system's constituents*".

A playground for the exploration of the physics associated with emergence has been provided by *transition metal oxides* (TMOs). Multiple degrees of electronic freedom are known to be simultaneously active in many of these oxides. The electronic properties of these materials are determined by a combination of spin-, charge- and orbital-effects and the electronic degrees of freedom are often coupled strongly to the crystal lattice [5]. Due to the competition between multiple interactions, TMOs may be susceptible (or 'soft') to the emergence of ordered phases of electronic matter. Some of the electronic degrees of freedom of these TMOs may be tuned by external parameters such as magnetic field, pressure or chemical doping and, consequently, many different electronic states may be realised in these materials. Well-known TMOs with complicated phase diagrams are the *cuprates* and *manganites* [4]. The *colossal magnetoresistance* (CMR) effect observed in some manganites is an emergent property believed to arise from competition between ferromagnetic-metallic and antiferromagnetic-insulating electronic phases. Regarding the high-temperature superconductivity observed in some cuprates, the microscopic origin of the pairing mechanism is still unclear; the pseudogap region of the phase diagram and the T-linear resistivity in the 'normal' metallic state are also not fully understood.

Since the discovery of superconductivity in Sr_2RuO_4 in the mid-1990's [6] the *ruthenate* series $(Sr,Ca)_{n+1}Ru_nO_{3n+1}$ ($n = 1, 2, 3, \infty$) has been studied extensively [7, 8, 9]. The $n = 2$ member of the strontium ruthenate series, $Sr_3Ru_2O_7$, has fascinating electronic properties. The metallic ground state of $Sr_3Ru_2O_7$ is not magnetically ordered, although the paramagnetic susceptibility is heavily renormalised by electron-electron correlations and magnetic exchange interactions [10]. As a consequence of very large renormalisation $Sr_3Ru_2O_7$ is thought to be close to a ferromagnetic instability. It is likely that the *metamagnetism* – empirically defined as a super-linear rise in uniform magnetisation as a function of external magnetic field – of $Sr_3Ru_2O_7$ [11] is associated with the heavy renormalisation of the electronic ground state. The

critical end point of this metamagnetism can be depressed towards $T = 0$ and, hence, become a *quantum critical point* (QCP) [12]. The discovery of a QCP in $Sr_3Ru_2O_7$ generated attention throughout the wider condensed matter physics community. Physics associated with QCPs had been studied extensively in the context of heavy-fermion (HF) materials, intermetallics of certain rare earths and actinides that contain $4f$ or $5f$ moments [13]. A second order magnetic phase transition in these HF materials can sometimes be depressed towards $T = 0$ by the application of external pressure or by selective chemical doping. However, the QCP in many of these materials was, quite remarkably, 'protected' by an emergent phase of electronic order in its vicinity. Figure 1.1 shows the (pressure, temperature) plane of the phase diagram of a single crystal of $CePd_2Si_2$. The antiferromagnetic Néel temperature, T_N, of this material is lowered by the application of an external pressure, P. When $P \sim 25$ kbar a dome of superconducting order emerges as $T_N \rightarrow 0$. Although the quantum critical behaviour of $Sr_3Ru_2O_7$ is not associated with a 2nd order phase transition, common physics is likely to be found in the vicinity of QCPs in all correlated electron systems. It was, therefore, desirable to search for emergent electronic order in the vicinity of the $Sr_3Ru_2O_7$ QCP.
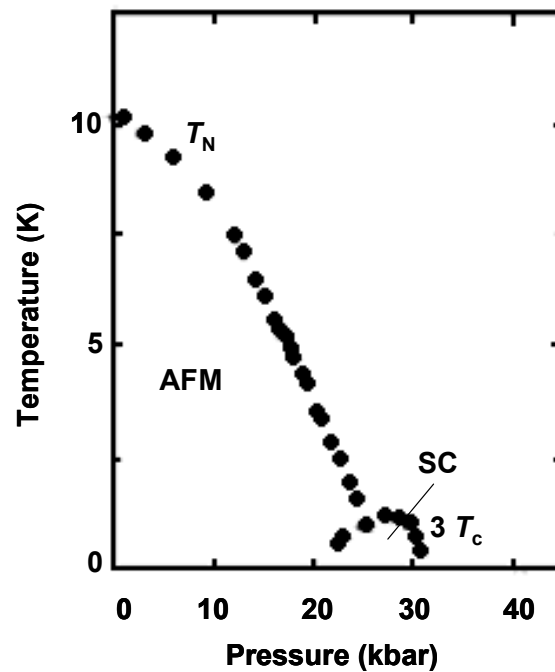
Figure 1.1. The (pressure, temperature) plane of the phase diagram of a high-purity single crystal of $CePd_2Si_2$. From [14].

Grigera *et al.* [15] utilised a number of experimental probes in their investigation of the vicinity of the QCP in ultrapure crystals of $Sr_3Ru_2O_7$. Surrounding the temperature and field at which the QCP had been proposed in more disordered samples in ref. 12 is a region in the (field, temperature) plane enclosed by distinctive phase boundaries, shown in Figure 1.2. These observations indicated that the QCP of $Sr_3Ru_2O_7$ was, like the QCPs of many HF metals, masked by an emergent state of ordered electronic matter. In work which I made a minor contribution to (and some of which is described in the appendix) Borzi *et al.* [16] discovered a remarkable in-plane magnetoresistive anisotropy associated with this novel state. This anisotropy is *not* related to an in-plane lattice anisotropy or to any demagnetisation effects and is, therefore, a consequence of *spontaneous* breaking of the symmetry of the fluid of correlated electrons, such that rotational invariance is lost. This state has been labelled as a correlated electron *nematic,* in contrast to the electron liquid from which it emerges (which retains the four-fold in-plane symmetry of the crystal lattice).
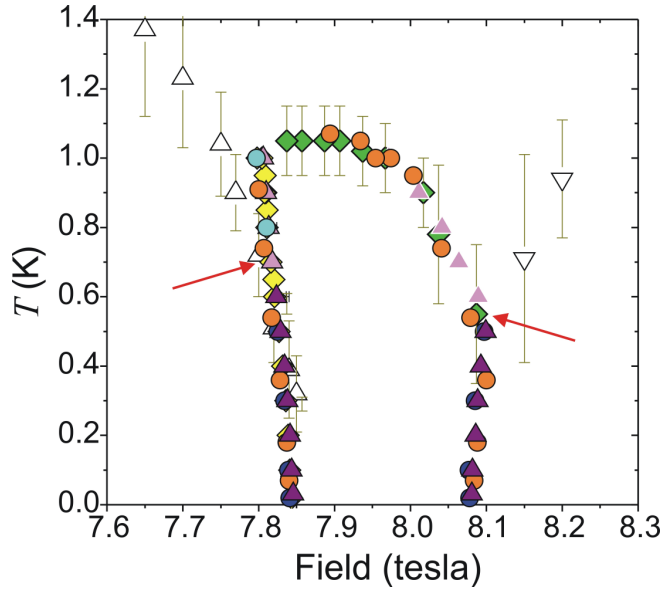
Figure 1.2. The (field, temperature) plane of the phase diagram of a high-purity single crystal of $Sr_3Ru_2O_7$ in the vicinity of the quantum critical endpoint of the metamagnetism. The different symbols correspond to separate measurements of AC susceptibility, thermal expansion, magnetostriction, magnetoresistance and magnetisation. From [15].

It may be possible to shed further light on the ground state of $Sr_3Ru_2O_7$ by doping the crystal lattice with foreign cations: this is the primary purpose of the original research reported in this thesis. It is desirable to investigate if cation doping can trigger magnetic ordering in this 'almost magnetic' metal; research on how doping influences the signatures of metamagnetism in some of the electronic properties is also sought. Reported in this thesis is the growth in an image furnace of crystals of cation-doped $Sr_3Ru_2O_7$ and measurements of some of the electronic properties of these crystals, namely DC magnetisation, molar heat capacity and electrical transport. Prior to the beginning of this research no work on image furnace-grown single crystals of cation-doped $Sr_3Ru_2O_7$ had been reported; a small number of articles have since been published (see section 1.4.5.1).

The measurements reported in this thesis shed much light on the physics associated with $Sr_3Ru_2O_7$. However, it was also anticipated that crystals grown in St Andrews during the execution of this work would be provided to other research groups involved with experimental techniques such as resonant X-ray scattering (RXS), neutron scattering, angle resolved photoemission spectroscopy (ARPES) and scanning tunnelling microscopy (STM). Regarding the research of ruthenates in recent years, these techniques, especially the first three, have complemented measurements of transport, heat capacity and magnetisation. STM measurements of ruthenates have been limited so far but, as discussed in section 3.7, such measurements *have* been made on some of the as-grown crystals referred to in this work.

Three experimental chapters are reported in this thesis, each concerned with substitution of different cations into $Sr_3Ru_2O_7$. Although some aspects of these chapters interlink with each other, each chapter stands alone to a great extent. The purpose of each of these chapters is to provide a comprehensive survey of the DC magnetisation, heat capacity and electrical transport of the series of crystals referred to. The results from these experiments have led to certain conclusions being made; these conclusions are discussed towards the end of each chapter. Another purpose of the three experimental chapters is to provide a basis from which future experiments on crystals grown during this work can be planned, either by the St Andrews group or by collaborating researchers.

Discussed in the remainder of this chapter are some aspects of the interacting electron problem in solids and some general properties of TMOs; a survey of the existing research of ruthenates, $Sr_3Ru_2O_7$ in particular, is also provided. The experimental techniques relevant to this work are described in Chapter 2. Measurements of the electronic properties of crystals in which some of the ruthenium ions have been replaced by TM cations, namely titanium and chromium in $Sr_3(Ru_{1-x}Ti_x)_2O_7$ and $Sr_3(Ru_{1-x}Cr_x)_2O_7$, are reported in chapters 3 and 4, respectively. It is shown in these chapters that magnetic ordering/irreversibility *can* be induced in $Sr_3Ru_2O_7$ by in-plane cation doping. Evidence for the suppression of metamagnetism and the formation a spin density wave as a function of Ti-doping is seen in the $Sr_3(Ru_{1-x}Ti_x)_2O_7$ series. Data in Chapter 4 indicate 'giant moment' magnetism and time-dependent magnetic irreversibility in samples of $Sr_3(Ru_{1-x}Cr_x)_2O_7$; these observations hint that the RKKY mechanism may be important in this series of materials. Reported in Chapter 5 is measurements of crystals with out-of-plane cation doping, namely $(Sr_{1-y}La_y)_3Ru_2O_7$. Measurements reported in this chapter seem to rule out the possibility that the metamagnetism of $Sr_3Ru_2O_7$ can be attributed to a rigid shift of an electronic band through a peak in the density of states near the Fermi level. It is also clear that the metamagnetism of $(Sr_{1-y}La_y)_3Ru_2O_7$ cannot be explained in full by a spin fluctuation extension to the Ginzburg-Landau theory of uniform magnetisation. Finally, work relating to the magnetoresistance of undoped $Sr_3Ru_2O_7$ is included as an appendix to this thesis. Although this final piece of work is not concerned with controlled cation doping it does, however, describe an investigation of the sensitivity of some of the properties of $Sr_3Ru_2O_7$ to quenched crystalline disorder.

1.2 Some Aspects of the Interacting Electron Problem in Solids

1.2.1 Fermi Liquid Theory

Landau [17] postulated that electron-electron interactions may be adiabatically 'switched-on' with respect to the ground state of a Fermi gas, so that there is a one-to-one correspondence between the eigenstates of the electron gas and those of the fluid of correlated electrons – the *Fermi liquid*. A Fermi liquid, like a Fermi gas, has a

Fermi surface separating empty and occupied states in **k**-space at the Fermi energy, E_F. The quantum numbers of the excitations of the Fermi liquid are not independent electrons but are Fermionic *quasiparticles* with well-defined charge and momentum. Unlike the eigenstates of a Fermi gas, Landau quasiparticles are not stationary. The rate of decay, τ^{-1}, of a quasiparticle of energy E is proportional to $(E-E_F)^2$: although a quasiparticle is *never* an eigenstate of a Fermi liquid, those quasiparticles with $E \sim E_F$ are long-lived and are an approximation to the true eigenstates of the electron liquid.

The Sommerfeld theory relevant to a Fermi gas predicts (in the first order of energy) that the electronic component of the heat capacity is proportional to temperature and that the paramagnetic spin susceptibility is independent of temperature [18]. These temperature dependences are also valid for an ideal Fermi liquid. The electronic component of the specific heat capacity, c_v, and the paramagnetic susceptibility, χ, of a Fermi liquid (single band, with an isotropic Fermi surface) are predicted to be

$$c_v = \frac{m^* k_F}{3\hbar^2} k_B^2 T \quad \text{and} \tag{1.2}$$

$$\chi = \frac{m^* k_F}{\pi^2} \frac{1}{1+F_0^a} \mu_B^2, \tag{1.3}$$

where m^* is the thermodynamic quasiparticle mass, F_0^a ($-1 > F_0^a > 0$) is one of the phenomenological Landau parameters in the theory, k_F is the Fermi wave vector and k_B and μ_B are Boltzmann constant and the Bohr magneton, respectively. The electronic heat capacity and the magnetic susceptibility of a Fermi liquid are, therefore, renormalised by factors of m^*/m and $(1+F_0^a)^{-1}m^*/m$ with respect to c_v and χ of a Fermi gas. The $(1+F_0^a)^{-1}$ factor is related to the *Wilson ratio*, R_W, of a paramagnetic Fermi liquid,

$$R_W = 7.3 \times 10^4 \frac{\chi_P}{\gamma} = (1+F_0^a)^{-1}, \tag{1.4}$$

where the Sommerfeld coefficient, γ, is the value of c_v/T extrapolated to $T = 0$ (in units of mJ/mol K^2) and χ_P is the Pauli susceptibility (in units of emu/mol) [19]. A Wilson ratio much greater than one may imply that a paramagnetic susceptibility is enhanced by magnetic exchange interactions, above the enhancement associated with m^*.

The electrical resistance of a Fermi liquid is concomitant with the aforementioned decay rate. Because $(E$-$E_F) \sim k_B T$ [20] the electrical resistivity of a Fermi liquid is therefore proportional to T^2, such that

$$\rho = AT^2, \tag{1.5}$$

where $A = m^* k_B^2 / ne^2 \hbar E_F$. It is straightforward to show that A —generally known as the Fermi liquid A coefficient— is proportional to $(m^*)^2$. In any real metal this T^2 resistivity term will act in addition to the residual resistivity, so that $\rho(T) = \rho_0 + AT^2$ at sufficiently low temperatures.

Fermi liquid theory is valid in a restricted region of phase space near a Fermi surface: if additional phase space can somehow be made available to a system (still in the context of a 'normal' metallic state) it is possible that the Landau quasiparticle picture may breakdown altogether, in which case a *non-Fermi liquid* description of the system may be appropriate. Schofield [21] provides a detailed discussion of non-Fermi liquids.

1.2.2 The Stoner Model

Equation 1.3 indicates that the spin susceptibility of a Fermi liquid is renormalised by the phenomenological $\left(1 + F_0^a\right)^{-1}$ factor in addition to the quasiparticle mass renormalisation. Blundell [22] describes how a Pauli susceptibility may be enhanced by extra splitting of spin-up and spin-down Fermi surfaces. In the presence of an applied magnetic field, H, the exchange-enhanced susceptibility is

$$\chi = \frac{M}{H} = \frac{\chi_P}{1 - Ug(E_F)}, \tag{1.6}$$

where U is some mean-field Coulomb interaction and g is the one-electron density of states. Equation (1.6) is valid for a magnetically-homogeneous system, for $\mathbf{q} = 0$. Metals for which the renormalised $\chi(\mathbf{q})$ peaks close to $\mathbf{q} = 0$ are often said to be *on the verge of a ferromagnetic instability*. If spin-up and spin-down bands are *spontaneously* split, ferromagnetism may occur if $Ug(E_F) > 1$, such that the renormalised χ diverges: this is the Stoner criterion.

1.2.3 Itinerant Electron Metamagnetism

1.2.3.1 A Metamagnetic Crossover from a Peak in *g(E)*

The uniform magnetisation, *M,* of a paramagnetic metal may be expressed in terms of the one-electron density of states in the vicinity of the Fermi energy. At $T = 0$ the magnetisation is:

$$M \propto \int_{E_F + \mu_B B}^{E_F - \mu_B B} g(E)\,\mathrm{d}E \ . \tag{1.7}$$

M will vary linearly with field if *g(E)* varies smoothly near E_F. If, on the other hand, *g(E)* is peaked in the vicinity of E_F, a super-linear rise in magnetisation as a function of external magnetic field *B* will occur – this is known as *metamagnetism* [23]. The field value at which the super-linear rise in *M(B)* is centred upon is known as the *metamagnetic field*, B_M. A metamagnetic *crossover* from a state of low-polarisation (at low field) to a state of higher polarisation (at high field) can be explained by a peak in *g(E)* at $E \approx E_F$. By contrast, a *phase transition* between the states of low- and higher-polarisation cannot be accounted for by a peak in *g(E)* because *M* is expected to *jump* (rather than just rise super-linearly) at $B = B_M$ when a phase transition occurs. A jump in *M(B)* cannot be accounted for by Equation 1.7.

1.2.3.2 Ginzburg-Landau Theory

An external magnetic field breaks the rotational symmetry of a paramagnetic state: metamagnetism does not involve any spontaneous symmetry breaking and cannot incorporate a 2nd order phase transition. Metamagnetism must, therefore, occur via a crossover or a 1st order phase transition from the low-field state into a more highly polarised state at fields above B_M.

If the thermodynamic order parameter of a given system is small in a certain region of its global phase diagram the free energy of the system may be related to an expansion of this order parameter – this is the basis of Ginzburg-Landau theory [24]. The uniform magnetisation is a relevant order parameter for itinerant electron

metamagnetism and an appropriate expression for the singular part of the Gibbs free energy (at $T = 0$) is

$$G = \frac{a}{2}M^2 + \frac{b}{4}M^4 + \frac{c}{6}M^6 - HM, \qquad (1.8)$$

where a, b and c are known as the Landau coefficients [25]. This expansion is valid if M is small compared to the saturation magnetisation of the system. The final term in Equation 1.8 is associated with an applied magnetic field. In the absence of an external field the magnetic behaviour of the system should be invariant under a change in the sign of the magnetisation and, consequently, the first three terms contain only even powers of M. It has been shown that, at $T = 0$, a metamagnetic phase transition can occur if $a > 0$, $b < 0$, $c > 0$ and $3/16 < ac/b^2 < 9/20$ [25].

1.2.3.3 The Influence of Finite Temperatures

Ginzburg-Landau theory provides a framework in which a first order metamagnetic phase transition may be considered but it does not provide any clue to the microscopic origin of such a transition. Binz and Sigrist [26] suggest that a first order metamagnetic phase transition can arise in an itinerant system with a large density of states near E_F due to a van Hove singularity in $g(E)$, along with electrons interacting via an on-site repulsion. These authors also show that the macroscopic susceptibility of such a system peaks at a finite temperature, T_{max}. A peak in $\chi(T)$ of an itinerant metamagnet was also predicted by Millis et al. [27]. It is also known that the finite temperature properties of itinerant electron metamagnets are influenced by thermal fluctuations of the magnetisation. Yamada [25] has shown that such fluctuations can be responsible for a peak in $\chi(T)$ of itinerant metamagnets at $T = T_{max}$, with T_{max} proportional to $a|b|/c$, where the Landau a coefficient is the inverse of the Pauli susceptibility. This model additionally predicts that B_M should increase as a function of temperature, an observation which is qualitatively consistent with the temperature dependence of B_M of various cobalt compounds (see discussion in ref. 25). Regarding the original work described in this thesis, the importance of the variation with temperature of the metamagnetic field is emphasised in Chapter 5.

In the limiting case of $ac/b^2 = 3/16$ in the model of Yamada and Goto [28], a

relationship between the metamagnetic field and the absolute value of the susceptibility at $T = T_{max}$ has been deduced:

$$B_M = \frac{1}{2} M_{ind} \left(\chi^{-1}(T_{max}) - \lambda a \right), \tag{1.9}$$

where λ is a dimensionless factor representing the anisotropy of the spin fluctuations and

$$M_{ind} = \left(\frac{3|b|}{4c} \right)^{\frac{1}{2}} \tag{1.10}$$

is the induced magnetisation at the critical point for the ferromagnetic ($B_M = 0$) state. It is not certain that this model is applicable to all itinerant metamagnets: metamagnetism may not always be adjacent in phase space to a ferromagnetic state. Nonetheless, a relationship between B_M and $\chi(T_{max})$ is explored for the $(Sr_{1-y}La_y)_3Ru_2O_7$ series of materials in Chapter 5 of this thesis.

1.2.4 Quantum Criticality

The previous section introduced the concept of itinerant electron metamagnetism. As discussed in section 1.1, much of the recent excitement associated with $Sr_3Ru_2O_7$ has arisen from the discovery of an ordered phase of electronic matter in the vicinity of the quantum critical point of the metamagnetism of this material. This section introduces some of the basic concepts associated with quantum critical behaviour.

1.2.4.1 2nd Order Quantum Criticality

There are no thermal fluctuations of a thermodynamic order parameter at $T = 0$ but there are *quantum* fluctuations (in both space and time) arising from zero point motion. These quantum fluctuations can compete with internal 'ordering' interactions and give rise to a *quantum phase transition* (QPT). A QPT between two ordered phases at $T = 0$ is driven by the application of some non-thermal control variable, p, such as pressure, chemical doping or magnetic field [29,30]. The critical value, p_c, of the external variable at which the QPT occurs is known as the *quantum critical point* (QCP).
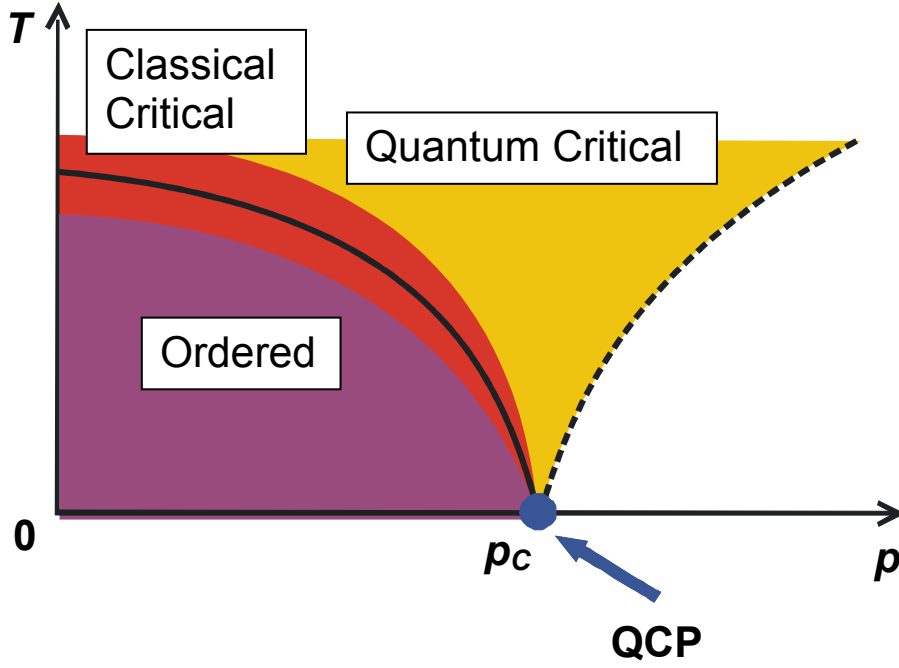
Figure 1.3. An illustration of how the 2nd order T_c of a classical phase transition may be depressed towards a quantum critical point by an external variable, *p*. From [31].

QCPs can sometimes be approached by depressing towards $T = 0$ the transition temperature, T_c, of a 2nd order classical phase transition by the application of a non-thermal control parameter; a sketch of this scenario is provided in Figure 1.3. The classical critical portion of the phase diagram is suppressed as $p \rightarrow p_c$. Thermal population of the modes of the quantum fluctuations occur at finite temperatures above the QCP, leading to a quantum critical 'fan' region of the phase diagram.

Two ordered phases are degenerate at a QCP and the internal energy scales of the system are renormalised to zero as the QCP is approached. In this situation the system can, in principle, be deformed without an energy penalty being incurred and, consequently, high susceptibility to the formation of phases of novel quantum order (such as the superconductivity of $CePd_2Si_2$, section 1.1) may be expected.

1.2.4.2 Quantum Critical Endpoints

Signatures of quantum criticality are not limited to systems with 2nd order classical transitions. An illustration of how a critical end-point (p_{c1}, T^*) of a line of 1st order

transitions may be depressed towards $T = 0$ by the application of another external variable, u, is given in Figure 1.4. A 1st order transition (as a function of p) when $T < T^*$ becomes a crossover (as a function of p) at temperatures above T^*. The value of both T^* and p_{c1} may depend on u: a *quantum critical endpoint* (QCEP) at $(p_{c2}, T^* = 0)$ may occur at some critical value of u. It is expected that the free energy landscape of such a system would be flattened on approach to the QCEP, making the system susceptible to novel phase formation, with quantum fluctuations also playing a crucial role in the physics.
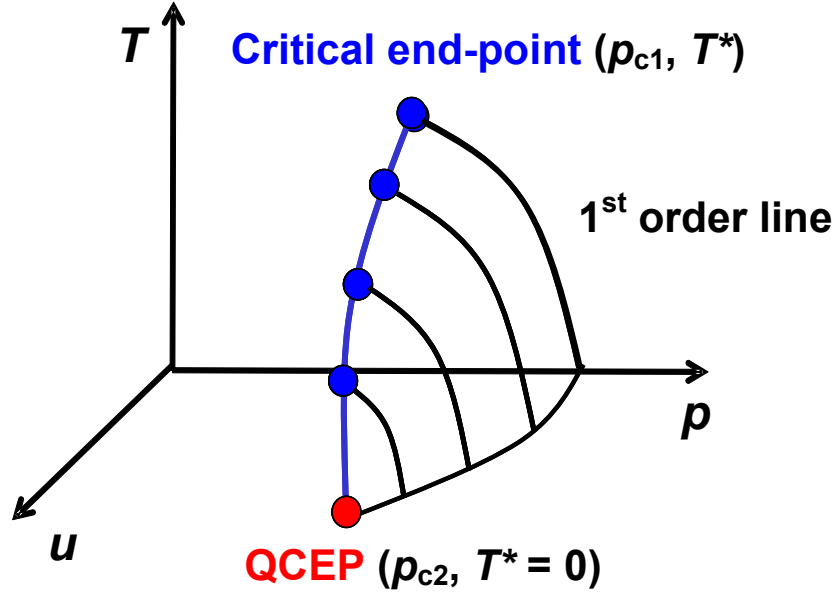
Figure 1.4. A line of 1st order phase transitions may terminate at a critical end point in the (p, T) plane. This critical end point may be depressed towards $T = 0$ and, hence, become a *quantum* critical end point, by a variable u. From [32].

1.3 Transition Metal Perovskites

A wide variety of phases of ordered electronic matter have been discovered in the aforementioned cuprates and manganites, both of which are examples of transition metal oxides. Goodenough [33] and Tsuda *et al.* [34] provide comprehensive descriptions of some of the electronic physics associated with TMOs; Rao and Raveau [35] also explore the chemistry of these oxides. Contained in this section is a survey

of the physics associated with the *perovskite* building block, the foundation of many TMOs including the cuprates and manganites.

1.3.1 Perovskite Crystal Structure

Compared to broadband conductors such as copper or the alkali metals the electronic bandwidth of metals with *d-* or *f*-shell valence electrons is expected to be rather narrow. The kinetic energy of electronic carriers in these materials will be relatively low and it is more likely that electron-electron interactions will play a significant role in the low-energy electronic physics.
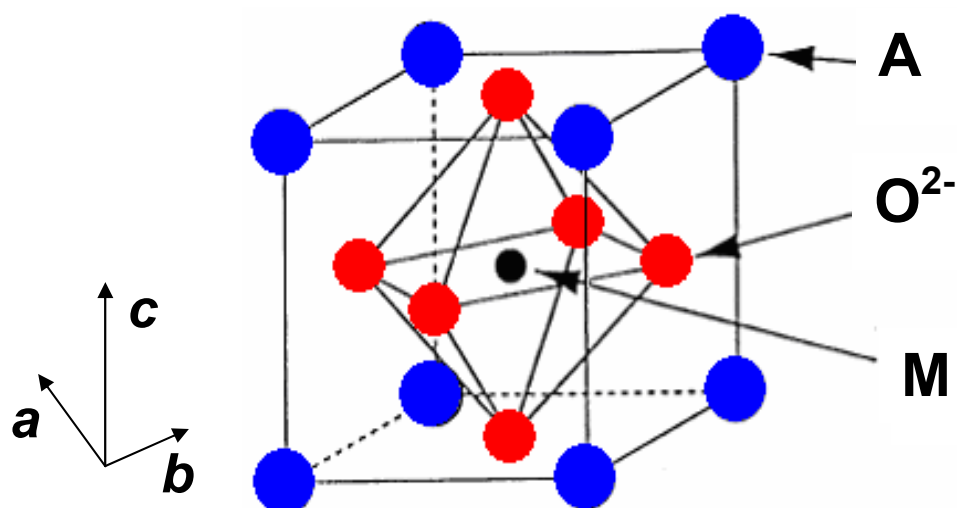
Figure 1.5. The ideal AMO$_3$ perovskite structure.

Transition metal oxides are a class of materials in which the valence electrons arise from atomic *d* shells. Transition metal cations can be incorporated into oxides in many crystal structures – the AMO$_3$ *perovskite* crystal structure (A = alkali metal, alkaline earth or lanthanide cation; M = transition metal cation; O = O^{2-}) is common. Illustrated in Figure 1.5 is the ideal perovskite structure. An A cation is located at the body-centre of an array of corner shared MO$_6$ octahedra. The M-O-M bond angle is 180° and each M-O bond is of equal length. Structural mismatches between A-O and M-O bonds lead to internal stresses which distort the structure of most real

perovskites. The *tolerance factor*, *t*, of an AMO_3 perovskite is defined in terms of the radii [36] of the ions in the crystal:

$$t = \frac{(r_A + r_O)}{\sqrt{2}(r_M + r_O)},$$ (1.11)

where the different *r* refer to the ionic radii of the A-site, M-site and oxygen cations. An ideal perovskite has $t = 1$ but most perovskites are not ideal and, hence, have a distorted structure. Such distortions can be cooperative rotations and/or tilting of the MO_6 octahedra.

1.3.2 Electronic Structure

Although TMOs are nominally ionic materials their electronic structure is not similar to that of textbook ionic solids such as NaCl: *hybridisation* of electronic orbitals from different ions is important in most TMOs. By treating the oxygen anions as point-like charges Khomskii [37] shows that, in the first order of energy, these O^{2-} ions produce a crystalline electric field which lifts the degeneracy of the five (= $2l + 1$) *d*-electron valence orbitals of the TM cation. Such *crystal field splitting* separates these 5 levels into lower and upper manifolds: t_{2g} and e_g respectively; Δ_{CF} is the magnitude of the crystal field splitting between the t_{2g} and e_g levels.

Goodenough [33] points out that the electronic band-structure at the Fermi energy of AMO_3 perovskites can often be attributed to hybridisation between orbitals from the TM and the O ions: the electronic states from the A-site cations are well-removed from E_F and can often be neglected when considering low-energy electronic properties. Overlap between the wavefunctions of the TM *d* electrons and the oxygen $2p$ electrons is known as *p-d hybridisation*. The electronic structure of AMO_3 perovskites is also sensitive to substitution of isovalent cations onto the A-sites. Although such substitution does not add or remove any electronic states at E_F the crystal structure *is* modified and the bond angles and, hence, the *p-d* hybridisation integrals are affected. *Non-isovalent* substitution on the A-site can also add or remove electrons from the band(s) at E_F. Holes can be introduced into the band(s) at the Fermi level if a trivalent cation is replaced by a divalent cation (electrons are introduced if the substitution is *vice versa*).

1.4 Ruddlesden-Popper Ruthenates

The previous section introduced the perovskite crystal structure, the basis of many TMOs. *Ruthenium* ions can be incorporated into the perovskite structure: the Ruddlesden-Popper series of layered *ruthenates*, $(Sr,Ca)_{n+1}Ru_nO_{3n+1}$ (n = 1, 2,…., ∞), has attracted much attention in recent years, especially since the discovery of superconductivity in Sr_2RuO_4 (n = 1) [6]. Towards the large-n end of the strontium ruthenate series are situated $SrRuO_3$ and $Sr_4Ru_3O_{10}$, both of which display ferromagnetic ordering. It is unsurprising that $Sr_3Ru_2O_7$, with an n-value between that of paramagnetic Sr_2RuO_4 and these ferromagnetic ruthenates, may be described as 'nearly magnetic' or 'on the verge of ferromagnetism'.

A detailed discussion of the existing research of $Sr_3Ru_2O_7$ is provided in section 1.4.5: evidence of the heavily renormalised ground state is referred to and the metamagnetic features in some of the electronic properties are discussed in detail. Reference is also made to the novel ordered phase in the vicinity of the quantum critical endpoint of the metamagnetism. The electronic band structure of $Sr_3Ru_2O_7$ is related to that of Sr_2RuO_4 – a discussion of the origins of these band structures is provided; reference is also made to the importance of electron-electron and electron-lattice interactions in ruthenates. Finally, previous studies of cation-doped $Sr_3Ru_2O_7$ are described.

1.4.1 Overview

The ideal crystal structures of some of the Ruddlesden-Popper ruthenates are shown in Figure 1.6. The number of layers of corner-shared RuO_6 octahedra is n; the effective dimensionality of the electronic structure changes from 2D (n = 1) to 3D (n = ∞): $Sr_3Ru_2O_7$ (n = 2) has a *bilayer* crystal structure and the electronic structure is often described as "quasi-2D". The ruthenium ions are nominally in the tetravalent state, with the four $4d$ valence electrons of each Ru^{4+} ion contained within the t_{2g} manifold (the ruthenium e_g orbitals are unoccupied). Ru^{4+} t_{2g} states are hybridised with oxygen $2p$ states to form π-type bands at the Fermi level.

16

The electronic states arising from Sr^{2+} or Ca^{2+} ions are believed to be well-removed from the Fermi level yet, for any given n, the electronic properties of the Sr and Ca end-members of the series are remarkably different. Ca_2RuO_4, for example, is an antiferromagnetic insulator while Sr_2RuO_4 is a paramagnetic metal. The primary effect of Ca/Sr alloying on the A-site is believed to be the modification of the electronic structure near the Fermi level due to structural distortions. Ca^{2+} has a smaller ionic radius than Sr^{2+} and, hence, structural distortions (relative to the ideal structure) are more severe in calcium ruthenates than in strontium ruthenates. These structural distortions are thought to be responsible for further splitting of the t_{2g} levels and modification of the low-energy electronic properties.
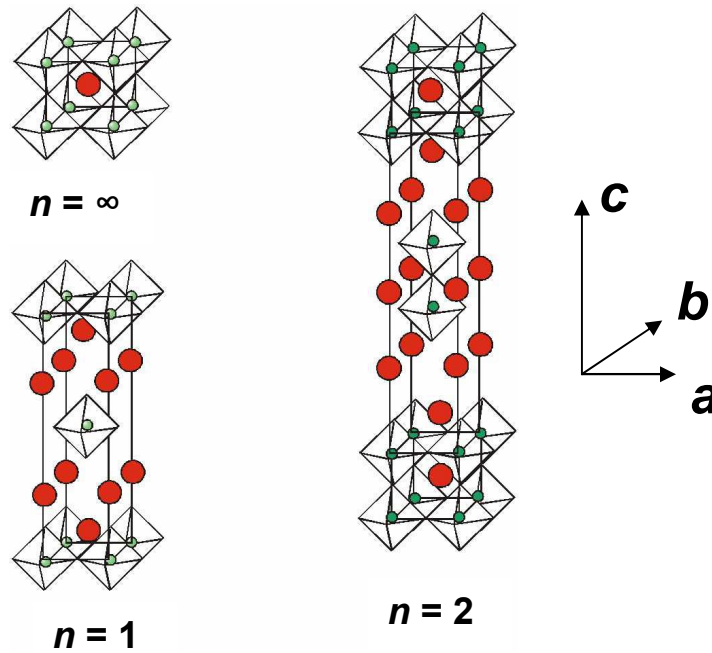
Figure 1.6. The ideal structures of some of the $(Sr,Ca)_{n+1}Ru_nO_{3n+1}$ Ruddlesden-Popper layered perovskite ruthenates. The large circles represent Sr^{2+} or Ca^{2+} cations; each Ru^{4+} cation (smaller circles) is surrounded by 6 O^{2-} ions. From [38].

1.4.2 Sr_2RuO_4

Maeno *et al.* [6] synthesised Sr_2RuO_4 because this single-layer ruthenate is isostructural to $La_{2-x}Sr_xCuO_4$, the first high-T_c cuprate superconductor to be

discovered. A superconducting T_c of ~ 1 K in polycrystalline Sr_2RuO_4 was reported in this study; a later study showed that the optimum T_c of 1.5 K in ultrapure single crystals was depressed towards $T = 0$ by greater amounts of quenched crystalline disorder [39]. This sensitivity to disorder indicated that the superconducting condensate is anisotropic in **k**-space and the superconductivity of Sr_2RuO_4 is, therefore, referred to as *unconventional* (i.e. not *s*-wave) [40].

The superconducting condensate of Sr_2RuO_4 emerges from a two-dimensional Fermi liquid normal state [41]; the electrical resistivity in-plane (current $\parallel$ *ab*) and out-of-plane (current $\parallel$ *c*) is proportional to T^2 at low temperatures. However, as is expected for an exemplary quasi-2D metal, the hybridisation of electronic orbitals *between* the conducting planes is much weaker than the hybridisation within these planes. Consequently, the in-plane resistivity of Sr_2RuO_4 is always much lower than the out-of-plane resistivity. The residual resistivity of a Sr_2RuO_4 crystal referred to in ref. 40 is 1 μΩcm in-plane and approximately 2 mΩcm along the *c*-axis; the values when $T = 300$ K are $\rho_{ab} = 120$ μΩcm and $\rho_c = 15$ mΩcm.

The Fermi surface of Sr_2RuO_4 is composed of three quasi-cylindrical bands: two of these bands, β and γ, are electron-like and a (hole-like) band, α, has its sheets centred about Brillouin zone corners. The main features of the Sr_2RuO_4 valence band-structure can be explained quite straightforwardly by considering nearest-neighbour hybridisation between Ru 4*d* and O 2*p* orbitals; Bergemann *et al.* provide an excellent discussion of this. A more comprehensive discussion of the band structure of quasi-2D ruthenates —Sr_2RuO_4 and $Sr_3Ru_2O_7$— is provided in section 1.4.5.1.

1.4.3 SrRuO₃ and Sr₄Ru₃O₁₀

The $n = \infty$ strontium ruthenate, $SrRuO_3$, is an itinerant ferromagnet with a Curie temperature of approximately 160 K and a saturation magnetic moment of ~ 1.6 μ_B/Ru. Mackenzie *et al.* [42] measured a resistivity proportional to T^2 at temperatures below approximately 10 K in high-quality thin films of $SrRuO_3$ and Shubnikov-de Haas (SdH) measurements revealed 2 Fermi surface sheets with quasiparticle masses of 4.5 and 6.1 m_e. It was therefore concluded that the ground state of $SrRuO_3$ is a

Fermi liquid. Alexander *et al.* [43] reported de Haas-van Alphen (dHvA) oscillations in a single crystal of $SrRuO_3$; this study indicated at least six fundamental frequencies of oscillation, with effective masses ranging from 4 to 7 m_e.

It is unsurprising that the magnetic character of $Sr_4Ru_3O_{10}$ ($n = 3$) is intermediate between that of a ferromagnet ($SrRuO_3$) and a paramagnet with metamagnetism ($Sr_3Ru_2O_7$). Zhou *et al.* [44] synthesised crystals of $Sr_4Ru_3O_{10}$ in an image furnace with a residual in-plane resistivity of approximately 6 $\mu\Omega$cm; a resistivity proportional to T^2 at low temperatures pointed towards a Fermi liquid ground state. Magnetisation measurements have indicated field-induced metamagnetic behaviour when $B \parallel ab$ and ferromagnetic behaviour when $B \parallel c$. The coexistence of interlayer ferromagnetism and intralayer metamagnetism has been confirmed by a number of studies [45, 46].

1.4.4 Calcium Ruthenates

Ca_2RuO_4 is a Mott-Hubbard insulator which undergoes a transition from an antiferromagnetic ground state to a paramagnetic state at $T_N = 113$ K [47]. A transition from the insulating state into a metallic state also occurs at $T = 357$ K [48]. The ground state of Ca_2RuO_4 has also been shown to be orbitally-ordered and to have strong magneto-structural coupling [49, 50].

Some initial reports [51, 52] claimed that the ground state of $Ca_3Ru_2O_7$ was insulating but a metallic ground state with approximately 0.001 free carriers per ruthenium was observed in high-quality single crystals [53, 54]. A 2nd order transition from the low temperature antiferromagnetic state into a paramagnetic state occurs at $T_N = 56$ K; a 1st order structural phase transition also occurs at $T = 48$ K.

$CaRuO_3$ is a paramagnetic metal with a low temperature resistivity proportional to $T^{3/2}$: a non-Fermi liquid ground state has been suggested for $CaRuO_3$ [55]. Schultz *et al.* [56] suggest that spin fluctuations arising from a quantum critical point may be important to the ground state physics of $CaRuO_3$.

1.4.5 $Sr_3Ru_2O_7$

Polycrystalline $Sr_3Ru_2O_7$ was synthesised by Williams and colleagues in 1991 [57] but Cava *et al.* [58] were first to report the electronic properties of powdered $Sr_3Ru_2O_7$. A maximum in $\chi(T)$ at approximately 20 K was observed and the susceptibility was proportional to $1/T$ at high temperatures. Ikeda *et al.* [10] reported a resistivity proportional to T^2 at low temperatures in single crystals of $Sr_3Ru_2O_7$ grown in an image furnace; no evidence of magnetic ordering of the electronic ground state was found in this study. The in-plane resistivity of these crystals varied between 3 $\mu\Omega$cm ($T = 0$) and 230 $\mu\Omega$cm ($T = 300$ K). The out-of-plane resistivity of $Sr_3Ru_2O_7$ was found to be much larger, as expected for a quasi-2D metal: ρ_c varied between 1 mΩcm and 8 mΩcm over the same range of temperatures.
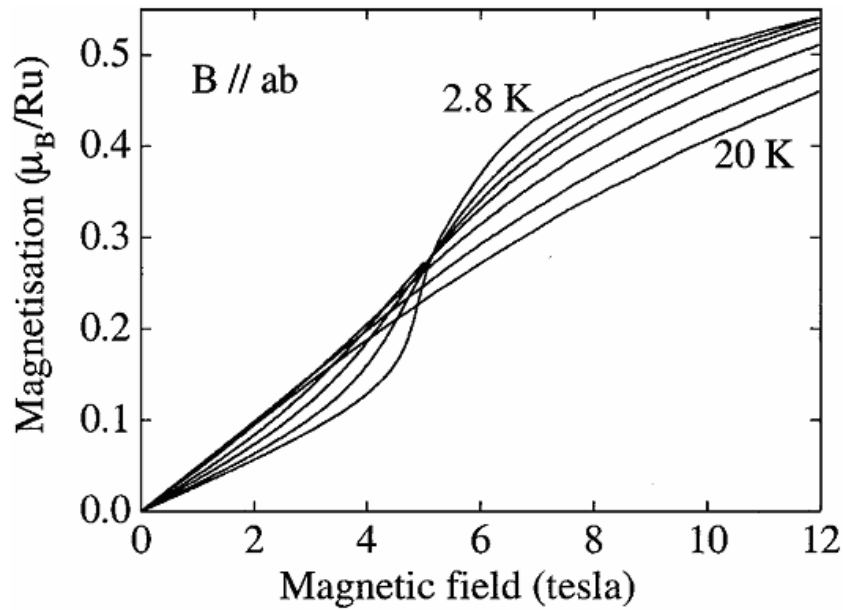
Figure 1.8. The magnetisation of $Sr_3Ru_2O_7$ as a function of magnetic field. From [11].

The Sommerfeld coefficient of the crystals in ref. 10 was 110 mJ/(Ru mol K^2), that is, significantly larger than the same quantity in single crystals of other metallic ruthenates, namely Sr_2RuO_4, $SrRuO_3$ and $CaRuO_3$. A zero-field Wilson Ratio of approximately 10 was deduced from a combination of C/T and $\chi(T)$ at low temperatures. It was therefore concluded that $Sr_3Ru_2O_7$ is a Fermi liquid on the verge

of ferromagnetism: the electronic ground state is heavily renormalised by electron-electron correlations and also by magnetic exchange interactions.

Perry *et al.* [11] discovered metamagnetism in $Sr_3Ru_2O_7$, shown in Figure 1.8. When $T = 2.8$ K a super-linear rise in the magnetisation as a function of field was observed for fields of $B_M = 5.5$ ($\parallel ab$) and 7.7 Tesla ($\parallel c$). Ohmichi and co-workers [59] found that the primary metamagnetic field (the field at which the largest change in magnetic moment occurs) evolved smoothly with field angle, θ, from 5.1 Tesla for $B \parallel ab$ to 7.7 T when $B \parallel c$. A secondary metamagnetic feature also varied smoothly with θ, from $B_{ab2} = 5.8$ T to $B_{c2} = 13.2$ T.
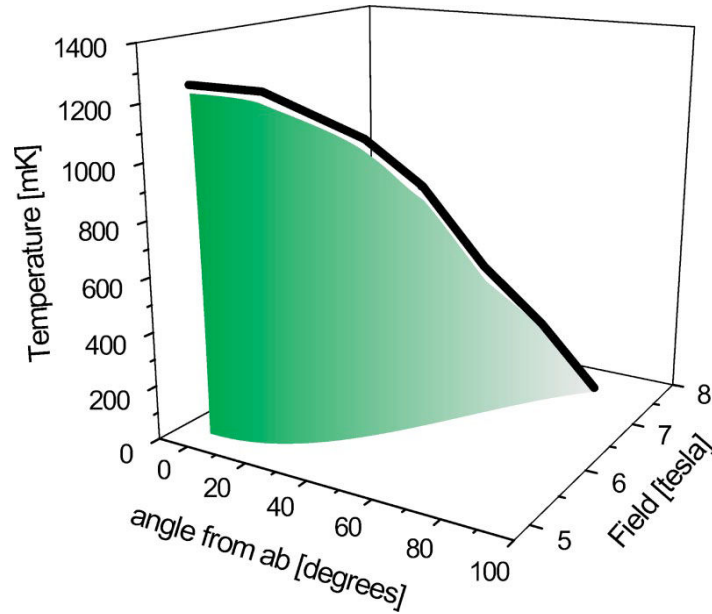
Figure 1.9. The empirically-defined phase diagram of the metamagnetism of $Sr_3Ru_2O_7$, inferred from measurements of AC susceptibility. The solid line and the sheet arise from measurements of the real and imaginary parts of the susceptibility, respectively. From [12].

Grigera *et al.* [12] studied the differential magnetic susceptibility of $Sr_3Ru_2O_7$ as a function of temperature, magnetic field and field angle. The variation with θ of the critical endpoint, (B_M, T^*), of the primary metamagnetism is shown in Figure 1.9. When $B \parallel ab$ $B_M = 5.1$ Tesla and $T^* = 1.25$ K. When the external magnetic field was aligned within a few degrees of the crystalline c-axis the metamagnetic critical endpoint was $(B_M = 7.8$ T, $T^* \leq 50$ mK), with the upper limit of T^* equal to the base

temperature of the dilution refrigerator used in this experiment. Grigera and co-workers noted that a T^* of zero corresponds to a quantum critical endpoint of the metamagnetism. Figure 1.9 can be compared directly with Figure 1.4, with the magnitude and the angle of the external magnetic field playing the role of p and u, respectively.

The possibility of quantum critical metamagnetic behaviour was indicated by Perry and co-workers [11] in their study of the temperature-dependent component of the resistivity ($\rho = \rho_0 + A T^\alpha$). For $B \parallel ab$ they showed that Fermi liquid behaviour ($\alpha = 2$) was observed at temperatures below approximately 10 K at high and low fields. When $B \sim B_M$ the Fermi liquid region was suppressed below their 2.5 K base temperature of measurement.
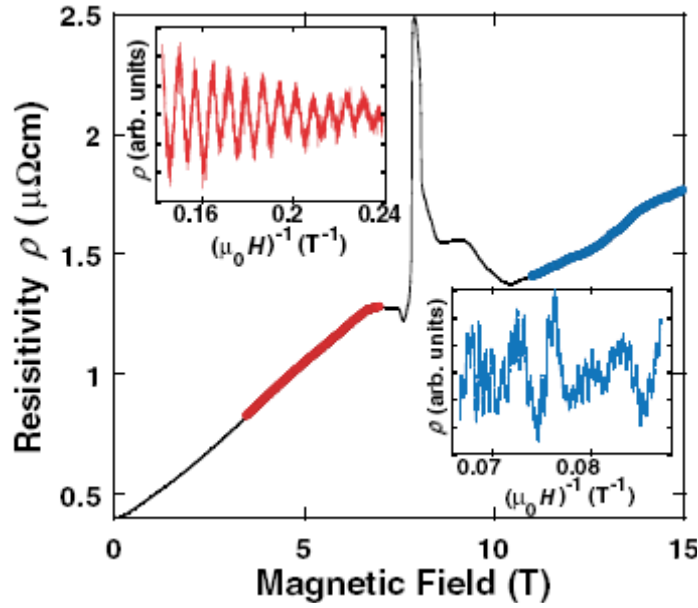
Figure 1.10. The magnetoresistance ($B \parallel c$) of Sr$_3$Ru$_2$O$_7$. SdH oscillations are seen at low- and high-fields. The steep sidewalls in $\rho(B)$ are coincident in field with the 1st order phase boundaries of the electronic state indicated in Figure 1.2. From [62].

It was suggested that non-Fermi liquid behaviour ($\alpha < 2$) was due to proximity to a quantum critical point. Measurement of the molar heat capacity, C, provided experimental support for the existence of critical fluctuations. When $B = 7.7$ T $\parallel c$-

axis, close to the metamagnetic field, the electronic component of C/T was found to diverge logarithmically as a function of T at low temperatures. In a further study at temperatures down to 100 mK Grigera *et al.* [60] measured the temperature dependence of the resistivity at different magnetic field values. In addition to confirming the suppression of the Fermi liquid behaviour in the vicinity of B_M they also deduced that the Fermi liquid A coefficient increased sevenfold as the field ($\parallel c$-axis) was increased from zero towards $B_M = 7.85$ Tesla. These observations pointed towards a divergence of the masses of some (or possibly all) of the Landau quasiparticles upon approach to a quantum critical endpoint of the metamagnetism.

The crystals studied in ref. 60 had a residual in-plane resistivity of approximately 3 $\mu\Omega$cm, a value that is quite low compared to ρ_0 of many other metallic TMOs. Perry and Maeno [61] reported the growth of $Sr_3Ru_2O_7$ crystals with an even lower residual resistivity, less than 0.5 $\mu\Omega$cm. The electronic mean free path of these ultraclean single crystals was sufficiently large for Perry *et al.* [62] to measure SdH oscillations and for Borzi and colleagues [63] to detect dHvA oscillations. These measurements indicated a clear difference in the frequency of quantum oscillations at high and low fields, thus hinting at a topographical change of the Fermi surface when $B = B_M$. It was also shown in ref. 62 that, for fields close to B_M, a well-defined region of magnetic field bounded by 1st order phase transitions is evident at low temperatures. Steep 'sidewalls' in $\rho(B)$, shown in Figure 1.10, enclose this region at temperatures below approximately 1 K. Further measurements of AC susceptibility, magnetisation, magnetostriction, thermal expansion and resistivity [15] showed that, surrounding the temperature and field at which a QCP had been proposed in more disordered samples in ref. 12 is a region in the (field, temperature) plane enclosed by phase boundaries, discussed in section 1.1.

The discovery of a new phase of electronic matter in the vicinity of QCP was a significant breakthrough. Evidence of this phase was not seen in dirtier $Sr_3Ru_2O_7$ crystals: sensitivity to crystalline disorder was evidence that this emergent electronic state was anisotropic in **k**-space. Measurements of electrical and thermal conductivity [64] indicated that the Wiedemann-Franz law was not violated within this phase, despite the suppression of Fermi liquid behaviour. Borzi *et al.* [16] discovered an *in-plane* magnetoresistive anisotropy associated with this phase. Elastic neutron

scattering measurements showed that the four-fold symmetry of the crystal structure in the *ab*-plane is unchanged in the region of phase space in which the resistive anisotropy was observed. AC susceptibility measurements on a variety of sample shapes also ruled out field-alignable magnetic domains due to shape-dependent demagnetisation effects as a source of this anisotropy. It was therefore concluded that the in-plane magnetoresistive anisotropy is *intrinsic* to the emergent state of correlated electron matter. An in-plane anisotropy in ref. 16 was also observed *away* from the QCP, when the external magnetic field was aligned parallel to the *ab*-planes of the crystal. Heat capacity data taken cooling down at the central field of this feature [65] show a logarithmic divergence of C/T down to 1 K, giving good evidence that this feature, like that for $B \parallel c$, is related to quantum criticality.

It has also been desirable to investigate how the metamagnetism of $Sr_3Ru_2O_7$ is linked to the heavily renormalised electronic ground state. Capogna *et al.* [66] probed the magnetic fluctuations of $Sr_3Ru_2O_7$ ($\rho_{ab0} \approx 3 \ \mu\Omega cm$) with inelastic neutron scattering (INS) measurements at zero-field. At low temperatures these fluctuations are incommensurate but cross over to ferromagnetic fluctuations at temperatures above approximately 20 K, a similar temperature to T_{max}. By studying the nuclear magnetic resonance of $Sr_3Ru_2O_7$ Kitagawa *et al.* [67] showed that the quantum critical fluctuations associated with the metamagnetism are *antiferromagnetic* in their nature which, in some respects, is at odds with the idea of metamagnetism being adjacent in phase space to a *ferromagnetic* state. Ramos and colleagues [68] performed INS measurements on high-quality crystals at large fields and found ferromagnetic *and* incommensurate fluctuations associated with the metamagnetism. Iwaya *et al.* [69] used scanning tunnelling microscopy (STM) to study the spectroscopic features of the metamagnetic criticality. At zero-field two sharp peaks in the quasiparticle DOS were seen on a meV scale near E_F. A *qualitative* change in these features was observed as an external magnetic field was varied across B_M. In addition, the spectral weight transfer on the meV scale as a function of magnetic field could not be reconciled with a Stoner-type scenario in which the chemical potential of a one-electron band is Zeeman-shifted by a magnetic field. This study indicated that the metamagnetism of $Sr_3Ru_2O_7$ cannot be explained in a rigid band-shift theory; the authors of ref. 69 speculate that spin fluctuations may be important to the metamagnetism of $Sr_3Ru_2O_7$.

1.4.5.1 The Band Structure of Quasi-2D Ruthenates

The electronic band structure at the Fermi level of both Sr_2RuO_4 and $Sr_3Ru_2O_7$ is due to hybridisation between ruthenium and oxygen orbitals. The band structure of the bilayer ruthenate can be related to that of Sr_2RuO_4, the main features of which can be explained quite straightforwardly. This section contains a discussion of how the Fermi surface of Sr_2RuO_4 arises and, in addition, a scheme for predicting the band structure of $Sr_3Ru_2O_7$ is also described. The influence of electron-electron correlations on some of the electronic properties of these materials is also discussed in this section.

(a)   (b)
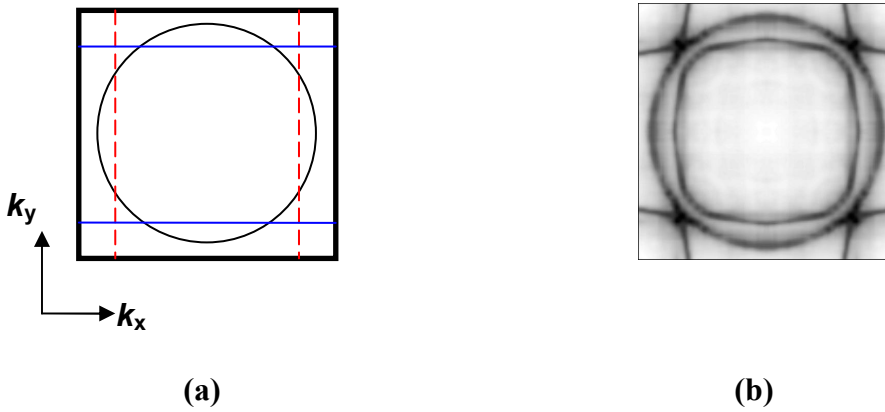
Figure 1.11. (a) A sketch of a 'toy' Sr_2RuO_4 Fermi surface in first Brillouin zone in the (k_x, k_y) plane. The circle, the solid lines and the dashed lines arise from hybridisation between Oxygen 2p orbitals and Ruthenium $4d_{xy}$, $4d_{zx}$ and $4d_{yz}$ orbitals, respectively. (b) The Fermi surface of Sr_2RuO_4 revealed by an ARPES experiment [70].

Sr_2RuO_4 has an ideal body-centred-tetragonal (K_2NiF_4) structure – each in-plane Ru-O-Ru bond angle is 180° and the electronic structure at the Fermi level is entirely due to π-type hybridisation between Ru $4d$ t_{2g} and O $2p$ orbitals. Each Ru $4d_{xy}$ orbital hybridises with 4 nearest-neighbour O $2p$ orbitals to produce a two-dimensional band – a circle in the (k_x, k_y) plane of the Brillouin zone. Each Ru $4d_{zx}$ and $4d_{yz}$ orbital hybridises with only two nearest-neighbour O $2p$ orbitals to produce bands which disperse in one dimension only – straight lines in the (k_x, k_y) plane. So that the underlying fourfold symmetry is respected, four of these lines must be incorporated into each Brillouin zone. The sketch in Figure 1.11(a) shows how these features may

be arranged in the first Brillouin zone. The lines arising from the d_{xz}/d_{zy}-O hybridisation form 4 pockets which enclose the zone corners. In any real electronic structure such pockets would correspond to hole-like Fermi surfaces. By contrast, any sheet which is centred about the zone centre would be an electron-like Fermi surface. Hybridisation gaps would be expected to appear near the sharp corners and, in addition, the remainder of the one-dimensional lines would be reconstructed into a sheet around the centre of the zone. Overall, measurements of the 'toy' Fermi surface in Figure 1.11 (a) would be expected to indicate two electron-like bands and one hole-like band. Figure 1.11(b) shows the Fermi surface of Sr_2RuO_4 deduced from photoemission experiments. 2 bands (gamma and beta) are centred about the centre of the Brillouin zone; pockets (alpha) enclose each corner of the Brillouin zone. The true Sr_2RuO_4 band structure is therefore qualitatively consistent with the predictions of a simple model involving nearest-neighbour hybridisation between Ru 4d t_{2g} and O 2p orbitals.

(a)   (b)
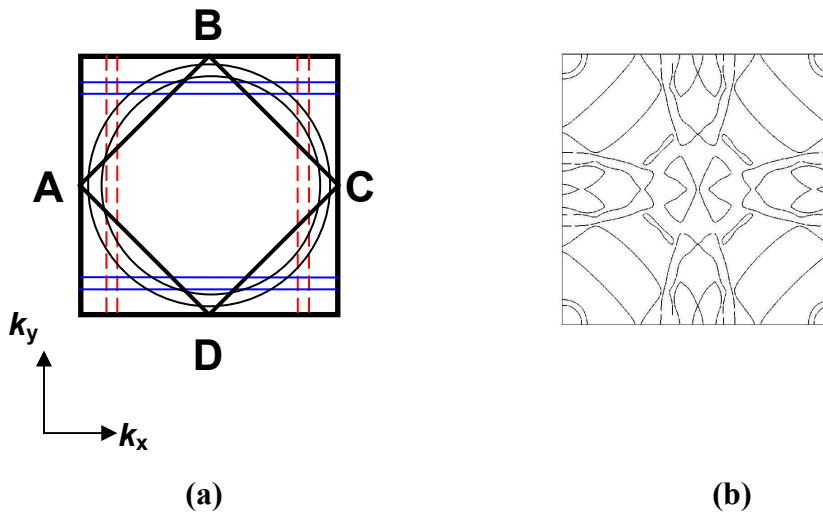
Figure 1.12. (a) A sketch of a 'toy' $Sr_3Ru_2O_7$ Fermi surface; ABCD is the new Brillouin zone which arises because of structural distortions. (b) The Fermi surface of $Sr_3Ru_2O_7$ predicted by Singh and Mazin; from [72].

The shape of each sheet of the Fermi surface of Sr_2RuO_4 predicted by calculations involving the local density approximation (LDA) [71] is in good agreement with experimental measurements. However, such calculations did not fully account for the effects of electron-electron correlations. Quasiparticle masses of 3.4, 7 and 16 m_e for

the α, β and γ sheets have been measured in quantum oscillation experiments; these values are enhanced above the band masses by factors of 3, 3.5 and 5.5, respectively. The renormalisation of the quasiparticle masses is one of the main effects of electron-electron interactions. Such renormalisation occurs because electron-electron interactions cause the slope of a band (in an $E(k)$ picture) near the Fermi energy to be changed from its bare (or 'band-only') value.

$Sr_3Ru_2O_7$ is also a quasi-2D metal and, to a first approximation, its band structure can be assumed to be like that of Sr_2RuO_4 but with double the electron count per unit cell (because of the *two* ruthenium ions). Hence, a 'toy' $Sr_3Ru_2O_7$ Fermi surface should look like Figure 1.11 (a) but with twice the number of lines. A sketch of this Fermi surface is given in Figure 1.12(a).

The crystal structure of $Sr_3Ru_2O_7$ is not ideally tetragonal: the in-plane Ru-O-Ru bond angle is approximately 164° and the a and b lattice parameters are slightly different —5.498 and 5.501 angstroms, respectively— such that the crystal structure is orthorhombic [72, 73]. The unit cell in real space is doubled and, therefore, the area of first Brillouin zone in k-space is half the area of the Sr_2RuO_4 Brillouin zone. The $Sr_3Ru_2O_7$ Brillouin zone is also rotated by 45°; this new zone corresponds to ABCD in Figure 1.12 (a). All Fermi surface sections must be folded into this new Brillouin zone. Singh and Mazin calculated the Fermi surface of $Sr_3Ru_2O_7$; a diagram of this is shown in Figure 1.12(b). Some of the 'double line' features are clear in this diagram; some small electron and hole pockets are also evident – the presence of these is beyond the scope of the simple Sr_2RuO_4-like model of the band structure. Overall, the approximation of $Sr_3Ru_2O_7$ as a quasi-2D metal in which large parts of the Fermi surface arise from π-type hybridisation between ruthenium and oxygen orbitals is not unreasonable.

1.4.5.2 Electron-Electron and Electron-Lattice Coupling

One challenge in the physics of correlated electron metals is to distinguish between different contributions to the quasiparticle mass enhancement. Renormalisation can occur because of electron-electron correlations and/or coupling of the electrons to collective modes, such as modes of the lattice. An investigation with ARPES [74]

shed light on the nature of the many-body renormalisation in Sr_2RuO_4. The entire bandwidth of the gamma band, rather than simply the dispersion near the Fermi level, was found to be renormalised by electron-electron correlations. This observation indicated that these correlations are highly localised in real space (renormalisation over a large range of k implies a small range in real space). In addition, effects of electron-phonon coupling on the low-energy electronic properties were found to be much less significant than the electron-electron interactions.

Many studies of the $Ca_{2-x}Sr_xRuO_4$ system have indicated a strong magnetostructural coupling in this series of ruthenates. The electronic structure near E_F of both the calcium and strontium ruthenates is believed to be due only to Ru-O hybridisation. On the other hand, calcium substitution is known to cause severe distortions of the ideal tetragonal crystal structure. The relative extent of electron-lattice and electron-electron coupling in ruthenates is a matter of interest. It is known that the p-d hybridisation paths in ruthenates are inextricable with the crystal lattice: in a study of the optical conductivity of many ruthenates Lee et $al.$ showed how p-d charge transfer excitations are related to phonon modes [75]. Regarding $Sr_3Ru_2O_7$, a large renormalisation of quasiparticle masses due to e-e interactions is implied by the large Sommerfeld coefficient; it is also postulated in ref. 16 that the nematic phase of $Sr_3Ru_2O_7$ may arise because of weakly-screened Coulomb interactions between electrons. By contrast, entry into this nematic phase has associated with it strong signatures in the magnetostriction, a clear signal of strong electron-lattice coupling. Overall, it is probable that e-e and e-latt interactions in ruthenates can have comparable effects. Consequently, how these two effects compete or cooperate with each other is not always clear. It is unsurprising that, in a similar manner to manganites and cuprates —in both of which multiple interactions are believed to be simultaneously active— many electronic phases can be realised in ruthenates.

1.4.5.3 Cation Doping Studies

Only a few studies have reported cation-doping of single crystals of $Sr_3Ru_2O_7$. Mathieu et $al.$ [76] studied some of the properties of single crystals of $Sr_3(Ru_{1-x}Mn_x)_2O_7$ ($x < 0.2$). The paramagnetic metallic ground state of $Sr_3Ru_2O_7$ was turned into an antiferromagnetic insulating state by doping with a small concentration of Mn

ions. Furthermore, the wavevector of the magnetic ordering was found to be $\mathbf{Q} \sim$ (0.25 0.25 0) in the (h k l) notation.

The manganese ions in $Sr_3(Ru_{1-x}Mn_x)_2O_7$ may exist as Mn^{3+} or Mn^{4+}, both of which have a nonzero effective magnetic moment. Hooper *et al.* [77] investigated single crystals of $Sr_3(Ru_{1-x}Ti_x)_2O_7$ ($x < 0.1$) in which the titanium cations are thought to be in the *nonmagnetic* Ti^{4+} ($3d^0$) state. Sharp features in the magnetoresistance of $Sr_3Ru_2O_7$ in the vicinity of B_M were smeared out by a small amount ($x = 0.005$) of Ti-doping. The peak in the DC susceptibility of $Sr_3Ru_2O_7$ at $T_{max} \sim 16$ K was also shifted to lower temperatures as a function of Ti-doping. It was also shown that a small amount of Ti-doping induced an upturn in C/T at temperatures below approximately 6 K.

1.5 References

[1] R. B. Laughlin and D. Pines, Proc. Nat. Acad. Sci. **97**, 28 (2000)

[2] D. Pines and P. Nozières, *The Theory of Quantum Liquids*, W. A. Benjamin (1966)

[3] H. Haken and H. C. Wolf, *The Physics of Atoms and Quanta* (6th Edition), Springer (2000)

[4] E. Dagotto, Science **309**, 257 (2005)

[5] Y. Tokura and N. Nagaosa, Science **288**, 462 (2000)

[6] Y. Maeno, H. Hashimoto, K. Yoshida, S. Nishizaki, T. Fujita, J. G. Bednorz and F. Lichtenberg, Nature **372**, 532 (1994)

[7] R. J. Cava, Dalton Trans. 2979-2987 (2004)

[8] G. Cao, C.S. Alexander, S. McCall, J.E. Crow and R.P. Guertin, Mat. Sci. Eng. B **63**, 76 (1999)

[9] S. G. Ovchinnikov, J. Mag. Mag. Mat. **258**, 210 (2003)

[10] S. Ikeda, Y. Maeno, S. Nakatsuji, M. Kosaka and Y. Uwatoko, Phys. Rev. B **62**, R6089 (2000)

[11] R. S. Perry, L. M. Galvin, S. A. Grigera, L. Capogna, A. J. Schofield, A. P. Mackenzie, M. Chiao, S. R. Julian, S. I. Ikeda, S. Nakatsuji, Y. Maeno and C. Pfleiderer, Phys. Rev. Lett. **86**, 2661 (2001)

[12] S. A. Grigera, R. A. Borzi, A. P. Mackenzie, S. R. Julian, R. S. Perry and Y. Maeno, Phys. Rev. B **67**, 214427 (2003)

[13] J. Flouquet, G. Knebel, D. Braithwaite, D. Aoki, J-P. Brison, F. Hardy, A. Huxley, S. Raymond, B. Salce and I. Sheikin, C. R. Physique **7**, 22 (2006)

[14] N. D. Mathur, F. M. Grosche, S. R. Julian, I. R. Walker, D. M. Freye, R. K. W. Haselwimmer and G. G. Lonzarich, Nature **394**, 39 (1998)

[15] S. A. Grigera, P. Gegenwart, R. A. Borzi, F. Weickert, A. J. Schofield, R. S. Perry, T. Tayama, T. Sakakibara, Y. Maeno, A. G. Green and A. P. Mackenzie, Science **306**, 1154 (2004)

[16] R. A. Borzi, S. A. Grigera, J. Farrell, R. S. Perry, S. J. S. Lister, S. L. Lee, D. A. Tennant, Y. Maeno and A. P. Mackenzie, Science **315**, 214 (2006)

[17] L. D. Landau, Sov. Phys. –JETP **5**, 101 (1957)

[18] J. Singleton, *Band Theory and Electronic Properties of Solids*, Oxford University Press (2001)

[19] R. H. McKenzie, arXiv:cond-mat/9905044v2

[20] N. W. Ashcroft and N. D. Mermin, *Solid State Physics*, Thomson Learning (1977)

[21] A. J. Schofield, Comtemp. Phys. **40**, 95 (1999)

[22] S. J. Blundell, *Magnetism in Condensed Matter*, Oxford University Press (2001)

[23] E. P. Wohlfarth and P. Rhodes, Phil. Mag. **7**, 1817 (1962)

[24] V.L. Ginzburg and L.D. Landau, Zh. Eksp. Teor. Fiz. **20**, 1064 (1950)

[25] H. Yamada, Phys. Rev. B. **47**, 11211 (1993)

[26] B. Binz and M. Sigrist, Europhys. Lett. **65**, 816 (2004)

[27] A. J. Millis, A. J. Schofield, G. G. Lonzarich and S. A. Grigera, Phys. Rev. Lett. **88**, 217204 (2002)

[28] H. Yamada and T. Goto, Physica B **346**, 109 (2004)

[29] P. Coleman and A. J. Schofield, Nature **433**, 226 (2005)

[30] A. J. Schofield, Physics World **16(8)**, 23 (2003)

[31] A. P. Mackenzie, private communication

[32] R. S. Perry, private communication

[33] J. B. Goodenough, *Localized to Itinerant Electronic Transition in Perovskite Oxides*, Springer (2001)

[34] N. Tsuda, K. Nasu, A. Fujimori and K. Siratori, *Electronic Conduction in Oxides* (2nd Edition), Springer (2000)

[35] C. N. R. Rao and B. Raveau, *Transition Metal Oxides* (2nd Edition), Wiley (1998)

[36] R. D. Shannon, Acta Crystallogr. A **32**, 751 (1976)

[37] D. Khomskii in *Spin Electronics*, edited by M. Ziese and M. J. Thornton, Springer (2001)

[38] R. S. Perry, PhD Thesis, University of Birmingham (2001)

[39] A. P. Mackenzie, R. K. W. Haselwimmer, A. W. Tyler, G. G. Lonzarich, Y. Mori, S. Nishizaki and Y. Maeno, Phys. Rev. Lett. **80**, 161 (1998)

[40] A. P. Mackenzie and Y. Maeno, Rev. Mod. Phys. **75**, 657 (2003)

[41] A. P. Mackenzie, S. R. Julian, A. J. Diver, G. J. McMullan, M. P. Ray, G. G. Lonzarich, Y. Maeno, S. Nishizaki and T. Fujita, Phys. Rev. Lett. **76**, 3786 (1996); C. Bergemann, A.P. Mackenzie, S.R. Julian, D. Forsythe and E. Ohmichi, Adv. Phys. **52**, 639 (2003)

[42] A. P. Mackenzie, J. W. Reiner, A. W. Tyler, L. M. Galvin, S. R. Julian, M. R. Beasley, T. H. Geballe and A. Kapitulnik, Phys. Rev. B **58**, R13318 (1998)

[43] C. S. Alexander, S. McCall, P. Schlottmann, J. E. Crow and G. Cao, Phys. Rev. B **72**, 024415 (2005)

[44] M. Zhou, J. Hooper, D. Fobes, Z. Q. Mao, V. Golub and C. J. O'Connor, Mat. Res. Bull. **40**, 942 (2005)

[45] M. K. Crawford, R. L. Harlow, W. Marshall, Z. Li, G. Cao, R. L. Lindstrom, Q. Huang and J. W. Lynn, Phys. Rev. B **65**, 214412 (2002)

[46] G. Cao, L. Balicas, W. H. Song, Y. P. Sun, Y. Xin, V. A. Bondarenko, J. W. Brill, S. Parkin and X. N. Lin, Phys. Rev. B **68**, 174409 (2003)

[47] S. Nakatsuji, S. Ikeda and Y. Maeno, J. Phys. Soc. Jpn. **66**, 1868 (1997)

[48] C. S. Alexander, G. Cao, V. Dobrosavljevic, S. McCall, J. E. Crow, E. Lochner and R. P. Guertin, Phys. Rev. B **60**, R8422 (1999)

[49] I. Zegkinoglou, J. Strempfer, C. S. Nelson, J. P. Hill, J. Chakhalian, C. Bernhard, J. C. Lang, G. Srajer, H. Fukazawa, S. Nakatsuji, Y. Maeno and B. Keimer, Phys. Rev. Lett. **95**, 136401 (2005)

[50] M. Kubota, Y. Murakami, M. Mizumaki, H. Ohsumi, N. Ikeda, S. Nakatsuji, H. Fukazawa and Y. Maeno, Phys. Rev. Lett. **95**, 026401 (2005)

[51] G. Cao, S. McCall, J. E. Crow and R. P. Guertin, Phys. Rev. Lett. **78**, 1751 (1997)

[52] H. L. Liu, S. Yoon, S. L. Cooper, G. Cao and J. E. Crow, Phys. Rev. B **60**, R6980 (1999)

[53] F. Baumberger, N. J. C. Ingle, N. Kikugawa, M. A. Hossain, W. Meevasana, R. S. Perry, K. M. Shen, D. H. Lu, A. Damascelli, A. Rost, A. P. Mackenzie, Z. Hussain and Z.-X. Shen, Phys. Rev. Lett. **96**, 107601 (2006)

[54] N. Kikugawa, A. Rost, F. Baumberger, N. J. C. Ingle, M. A. Hossain, W. Meevasana, K. M. Shen, D. H. Lu, A. Damascelli, A. P. Mackenzie, Z. Hussain and Z. X. Shen, J. Mag. Mag. Mat. **310**, 1027 (2007)

[55] L. Klein, L. Antognazza, T. H. Geballe, M. R. Beasley and A. Kapitulnik, Phys. Rev. B **60**, 1448 (1999)

[56] M. Schultz, L. Klein, J. W. Reiner and M. R. Beasley, Physica B **378**, 490 (2006)

[57] T. Williams, F. Lichtenberg, A. Reller and J. G. Bednorz, Mat. Res. Bull. **26**, 763 (1991)

[58] R. J. Cava, H. W. Zandbergen, J. J. Krajewski, W. F. Peck, B. Batlogg, S. Carter, R. M. Fleming, O. Zhou and L. W. Rupp, J. Solid State Chem. **116**, 141 (1995)

[59] E. Ohmichi, Y. Yoshida, S. I. Ikeda, N. V. Mushunikov, T. Goto and T. Osada, Phys. Rev. B **67**, 024432 (2003)

[60] S. A. Grigera, R. S. Perry, A. J. Schofield, M. Chiao, S. R. Julian, G. G. Lonzarich, S. I. Ikeda, Y. Maeno, A. J. Millis and A. P. Mackenzie, Science **294**, 329 (2001)

[61] R. S. Perry and Y. Maeno, J. Cryst. Growth **271**, 134 (2004)

[62] R. S. Perry, K. Kitagawa, S. A. Grigera, R. A. Borzi, A. P. Mackenzie, K. Ishida and Y. Maeno, Phys. Rev. Lett. **92**,166602 (2004)

[63] R. A. Borzi, S. A. Grigera, R. S. Perry, N. Kikugawa, K. Kitagawa, Y. Maeno and A. P. Mackenzie, Phys. Rev. Lett. **92**, 216403 (2004)

[64] F. Ronning, R. W. Hill, M. Sutherland, D. G. Hawthorn, M. A. Tanatar, J. Paglione, L. Taillefer, M. J. Graf, R. S. Perry, Y. Maeno and A. P. Mackenzie, Phys. Rev. Lett. **97**, 067005 (2006)

[65] R. S. Perry, T. Tayama, K. Kitagawa, T. Sakakibara, K. Ishida and Y. Maeno, J. Phys. Soc. Jpn. **74**, 1270 (2005)

[66] L. Capogna, E. M. Forgan, S. M. Hayden, A. Wildes, J. A. Duffy, A. P. Mackenzie, R. S. Perry, S. Ikeda, Y. Maeno and S. P. Brown, Phys. Rev. B **67**, 012504 (2003)

[67] K. Kitagawa, K. Ishida, R. S. Perry, T. Tayama, T. Sakakibara and Y. Maeno, Phys. Rev. Lett. **95**, 127001 (2005)

[68] S. Ramos, E. M. Forgan, C. Bowell, S. M. Hayden, A. J. Schofield, A. Wildes, E. A. Yelland, S. P. Brown, M. Laver, R. S. Perry and Y. Maeno, Physica B (in press)

[69] K. Iwaya, S. Satow, T. Hanaguri, N. Shannon, Y. Yoshida, S. I. Ikeda, J. P. He, Y. Kaneko, Y. Tokura, T. Yamada and H. Takagi, Phys. Rev. Lett. **99**, 057208 (2007)

[70] A. Damascelli, D. H. Lu, K. M. Shen, N. P. Armitage, R. Ronning, D. L. Feng, C. Kim, Z. X. Shen, T. Kimura, Y. Tokura, Z. Q. Mao and Y. Maeno, Phys. Rev. Lett. **85**, 5194 (2000)

[71] T. Oguchi, Phys. Rev. B **51**, 1385 (1995)

[72] D. J. Singh and I. I. Mazin, Phys. Rev. B **63**, 165101 (2001)

[73] H. Shaked, J.D. Jorgensen, O. Chmaissem, S. Ikeda and Y. Maeno, J. Solid State Chem. **154**, 361 (2000)

[74] K. M. Shen, N. Kikugawa, C. Bergemann, L. Balicas, F. Baumberger, W. Meevasana, N. J. Ingle, Y. Maeno, Z.-X. Shen and A. P. Mackenzie, Phys. Rev. Lett. **99**, 187001 (2007)

[75] J. S. Lee, Y. S. Lee, T. W. Noh, S. Nakatsuji, H. Fukazawa, R. S. Perry, Y. Maeno, Y. Yoshida, S. I. Ikeda, J. Yu and C. B. Eom, Phys. Rev. B **70**, 85103 (2004)

[76] R. Mathieu, A. Asamitsu, Y. Kaneko, J. P. He, X. Z. Yu, R. Kumai, Y. Onose, N. Takeshita, T. Arima, H. Takagi and Y. Tokura, Phys. Rev. B **72**, 092404 (2005)

[77] J. Hooper, M. H. Fang, M. Zhou, D. Fobes, N. Dang, Z. Q. Mao, C. M. Feng, Z. A. Xu, M. H. Yu, C. J. O'Connor, G. J. Xu, N. Andersen and M. Salamon, Phys. Rev. B **75**, 060403 (2007)

2. Experimental Techniques

The aforementioned novel electronic phase in $Sr_3Ru_2O_7$ was observed in *ultrapure single crystals*. Single crystals are desirable in many condensed matter experiments because grain boundaries can obscure intrinsic anisotropies in the elastic and electronic properties of materials. Furthermore, the requirement for very *clean* single crystals is not limited to ruthenates – magnetic field-induced superconductivity in URhGe [1] and quantum oscillations in YBCO [2] are two examples of discoveries made possible by having very clean single crystals. Crystal growth procedures are, therefore, worthy of discussion alongside the experimental results reported in this thesis.

Two categories of crystal growth are *solution growth* —the growth of a solute from a melt of a different composition to that of the desired crystal— and *melt growth*, which involves a liquid-solid phase transition at some melting temperature, T_M. Regarding solution growth, single crystals of ruthenates have previously been grown using the *flux method*, in which components of the desired material are reacted in a solvent. Strontium ruthenates, for example, have been synthesised from RuO_2, $SrCO_3$ and a $SrCl_2$ flux contained within a platinum crucible [3,4]. The major advantage of the flux method is that the desired material can be grown at a temperature which is much less than its melting point; the flux method is particularly useful for materials which melt incongruently. However, impurities from both the flux and the crucible may contaminate the as-grown single crystals. To minimise crystalline contamination it is desirable to grow strontium ruthenate single crystals directly from a melt containing only atoms of strontium, ruthenium and oxygen.

Growth directly from the melt occurs in the *floating zone* (FZ) method of crystal growth, in which infra-red radiation generated within an *image furnace* melts a ceramic rod of the desired material, so that a single crystal can be extracted from the melt. The major advantage of this method is that no crucible or solvent are required and the probability of impurity contamination is therefore low. The most challenging

factor associated with the FZ method is that many interdependent experimental control variables must be optimised simultaneously.

This chapter provides a description of how an image furnace works and how single crystals of $Sr_3Ru_2O_7$ have been grown. The structural properties of as-grown crystals have been measured with X-ray diffraction; the content of dopant ions in crystals of cation-doped $Sr_3Ru_2O_7$ has been ascertained with energy dispersive X-ray analysis; both of these experimental techniques are described in this chapter. Also described is the cryogenic equipment used to measure the electronic properties of as-grown crystals.

2.1 Crystal Growth

2.1.1 The Phase Diagram of a Reactive, Incongruent System

The purpose of this section is to consider some of the issues associated with the chemical phase diagram of a reactive, incongruently melting system, such as $Sr_3Ru_2O_7$. Atkins [5] provides an excellent discussion of the phase diagrams of multi-component systems; Perry [6] also provides a description similar to that which is given here.

The Gibbs phase rule relates the number of intensive variables of a system, F, to the number of components, C, and the number of phases, P, of the system:

$$F = C - P + 2 \qquad\qquad (2.1)$$

$Sr_3Ru_2O_7$ is known to melt *incongruently* – it melts into its components but cannot itself form a liquid; P is therefore equal to 1. $Sr_3Ru_2O_7$ is a binary (C = 2) system because its components are SrO and RuO_2. Accordingly, the number of intensive variables for $Sr_3Ru_2O_7$ is three: temperature, pressure and the composition of the SrO/RuO_2 mixture. During image furnace growth pressure is usually chosen to be kept constant. Figure 2.1 shows a sketch of the phase diagram of a two-component, reactive, incongruently melting system. The two starting components are A and B; C

is the desired component. At the peritectic point a liquid, L, is in equilibrium with two solid phases. It is clear that simply melting together a stoichiometric mixture of A and B and then cooling this mixture will *not* result in C being produced: C must be extracted directly from the C + L region of the phase diagram. Extracting C will change the composition of this region and, hence, there is a possibility that removing C will cause a shift away from this area of the phase diagram. Furthermore, it is essential that a *non*-stoichiometric ratio of A and B is mixed together; account must also be taken of possible evaporation of either A or B. For $Sr_3Ru_2O_7$ these factors were explored in much detail by Perry and Maeno [7].
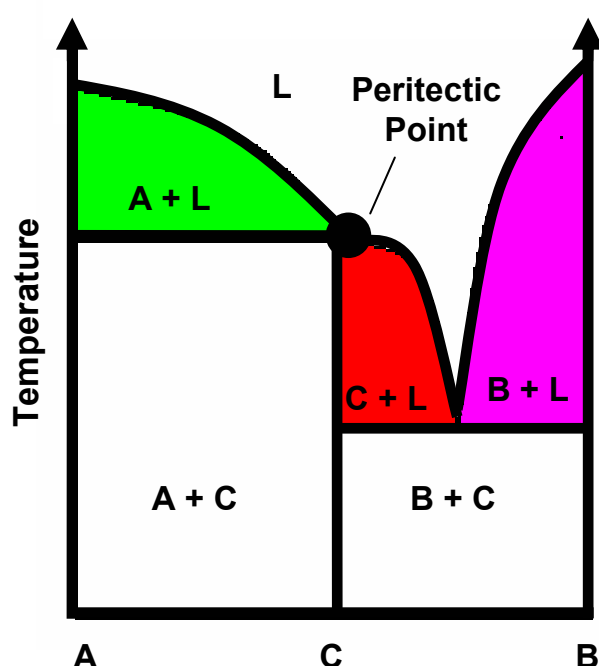
Figure 2.1. The phase diagram of a reactive, incongruent system. Copied from [6].

2.1.2 Material Preparation

A cylindrical rod of ceramic material, known as a *feed rod*, is required in the FZ method. Described here is a procedure for synthesising a strontium ruthenate feed rod from $SrCO_3$ and RuO_2 powders. Aside from a change in the starting materials the same procedure has been used to prepare feed rods of cation-doped $Sr_3Ru_2O_7$, referred to in chapters 3-5. $SrCO_3$ is hygroscopic so, prior to its use alongside RuO_2, must be

dried; drying in air in a box furnace at $T = 400°C$ for approximately 5 hours is suitable. RuO_2 and dried $SrCO_3$ powders were ground together in air with an agate mortar and pestle. The solid state reaction between strontium carbonate and ruthenium oxide is

$$a \cdot SrCO_3 + b \cdot RuO_2 = Sr_aRu_bO_{a+2b} + a \cdot CO_2 \ . \qquad (2.2)$$
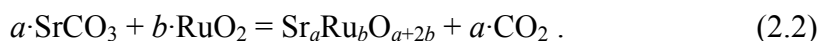
At the high temperatures (2000 – 2500°C) typical within an image furnace RuO_2 has a high vapour pressure and is susceptible to evaporation. To compensate for this evaporation an *excess* of RuO_2 must be incorporated into the initial mixture of powders. A growth parameter, $n = 2b/a$, may be defined: empirical values are $n = 1.15$, 1.68 and 1.9 for Sr_2RuO_4 [8], $Sr_3Ru_2O_7$ [7] and $Sr_4Ru_3O_{10}$ [9], respectively. The total mass of powders used in each synthesis was approximately 10 grams. After being ground for approximately 20 minutes the mixed powder was compressed into a cylindrical pellet of 2cm diameter, 1cm depth. This pellet was placed on a pre-prepared strontium ruthenate 'bedding pellet' inside an alumina crucible and baked in air in a box furnace at $T = 1200°$ C for 16 hours. The purpose of the bedding pellet is to ensure that no aluminium from the crucible diffuses into the main pellet during the heating period.

The baked pellet was cooled in air to room temperature and then ground into a fine powder; this powder was then placed inside a Latex balloon. The manufactured Latex balloons were covered with a fine, powdered coating so, in order to minimise contamination, this coating was scrubbed off with an ethanol-soaked fine tissue. The clean balloon was then coated with a layer of the ruthenate powder and was then filled with the remaining powder. The balloon was then tied at both ends, placed inside a water-filled pressure cell and subjected to a hydrostatic pressure of 40 MPa. This pressure was then reduced to zero and the balloon was removed from the pressure cell. The balloon was then cut open and the rod-shaped compacted powder was removed.

The ruthenate rods were found to be very fragile and could break when being removed from the pressure cell. Figure 2.2 shows three ways of mounting a powder-filled balloon prior to it being placed in the water-filled pressure cell. In the initial

period of research the balloon (~ 8cm length) was fixed with string within a hollow metal cylinder. On removal from the pressure cell the balloon was gently dragged out of this cylinder, cut open and the rod was then removed. Approximately 40 % of the rods made with this method remained intact after removal from the balloon: the rod often broke when the balloon was dragged out of the cylinder or when the rod was pushed out of the balloon. In an attempt to overcome this problem a different mounting technique was used: the balloon was tied down to a flat metal surface (a 15cm steel rule) before being placed in the pressure cell. The probability of successful rod manufacture was ~ 50%, a slight improvement on the previous method, but still unacceptable. A major breakthrough was made when a *stretched* filled balloon was mounted on the outside of a narrow metal cylinder: approximately 90% of the oxide rods made by this method have remained intact after compression and removal from the balloon. This method is a reliable way of manufacturing ruthenate rods; rods of other oxides such as $Dy_2Ti_2O_7$ and $YTiO_3$ (which must be prepared from *unreacted* constituents) have also been manufactured by other researchers with a similar rate of success. The stretched balloon retracts very rapidly when cut at one end and the oxide rod has been found to sometimes break, but rarely. It has been possible to produce very long rods (15 - 20 cm) on a regular basis.
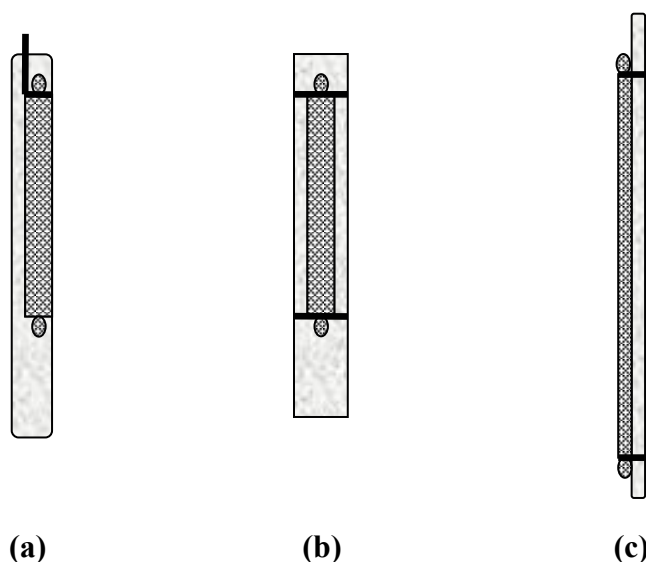

(a)   **(b)**   **(c)**

Figure 2.2. Three ways of mounting a powder-filled balloon prior to its immersion in a hydrostatic pressure cell. (a) shows a balloon within the cross-section of a thin-walled metal cylinder; (b) shows the balloon tied to a flat metal surface; (c) shows a stretched balloon tied to the outside of a metal cylinder.

In preparation for use in the image furnace each feed rod was placed on a pre-prepared strontium ruthenate bedding powder (on top of an alumina plate) and then sintered at $T = 1420°C$ for 2 hours, in air.

2.1.3 Image Furnace Growth

A photograph of the St Andrews image furnace is shown in Figure 2.3. The feed rod was suspended from a metal hook on the upper spindle; a seed (which may be a previously grown single crystal or another sintered rod) was mounted coaxially with respect to the feed rod in an alumina holder on the lower spindle. The metal hook was made from a platinum wire; Chromel wire was used to fix in place both the feed rod and the seed. Each of the spindles was connected to motors which permit vertical translation and also rotation around the vertical axis. The spindles, feed rod and seed crystal were contained within a transparent quartz tube in which an atmosphere (from a gas cylinder) could be established. The purpose of the metallic cold-trap is to provide a surface onto which evaporated oxide material can condense. The cold-trap is especially useful in crystal growths during which significant evaporation of constituent material occurs; some evaporated material will condense onto the inner surface of the quartz tube during such growth runs. The cold trap prolongs the period of time over which the quartz tube remains reasonably transparent to IR radiation.

The quartz tube is located within an ellipsoidal mirrored cavity: infra-red radiation from 2 halogen bulbs (placed at the foci of this cavity) was focused from the gold-plated mirrors towards a ~ 1 cm^3 region at the centre of the cavity at which a 'hot zone' was established. This hot-zone was monitored by a CCD camera linked to a computer.

The experimental variables in the FZ method may be classified as *primary* (which are chosen to be fixed prior to crystal growth) or *secondary* (which may be altered during the growth process). The primary variables are the atmospheric content and pressure, P, and the speed at which the lower spindle moves downwards – the *growth speed*, V_1. The secondary variables are the lamp power, W, the rotational speed of the rods, ω

(the upper and lower rotational speeds need not be equal), and the speed at which the upper spindle moves downwards – the *feed speed*, V_2. Varying the feed speed is a helpful way of promoting stability in the molten zone: if the zone looks to be too wide (relative to the seed) V_2 can be reduced; V_2 may be increased if the molten zone is at the threshold of collapse. Angular thermal gradients are suppressed by counter-rotating the upper and lower spindles during a growth run.
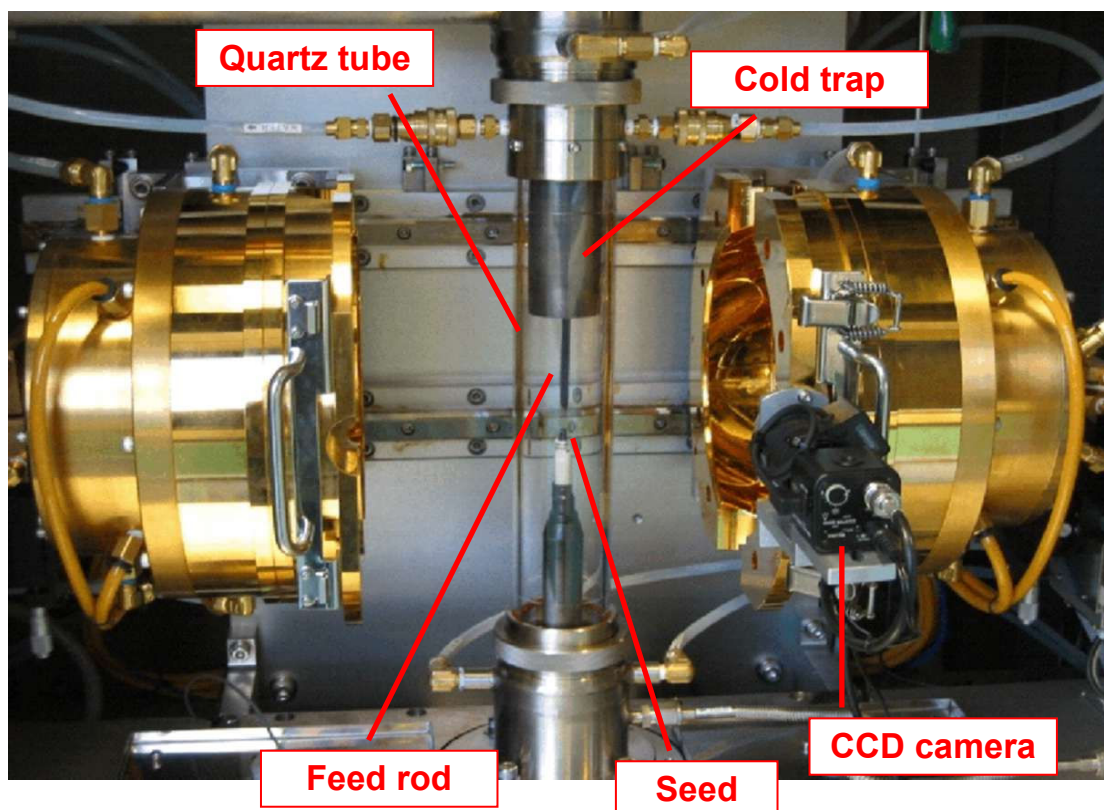
Figure 2.3. A photograph of the St Andrews image furnace. The two elliptic mirrors are closed together when the furnace is operating. A halogen bulb (not clear in the photograph) is located at the focal point of the each of the elliptic mirrors.

A stable molten zone occurs when the rate of material entering the zone is equal to the rate of material being deposited onto the seed plus the rate of evaporation. In growth runs involving non-volatile materials the secondary growth variables do not need to be changed often. By contrast, it is necessary to alter the secondary growth parameters many times during ruthenate growth runs. Varying the lamp power leads to a concomitant variation in temperature. If the temperature is too high the molten zone

will have a low viscosity and the grown crystal will be rather wide – material may actually leak out of the molten zone and down the sides of the seed crystal. On the other hand, the intermediate zone will not be wholly molten if the temperature is too low. Temperature is not monitored directly in the image furnace so the user must judge the stability of the molten zone. As a ruthenate growth proceeds RuO_2 evaporates onto the quartz tube which, consequently, becomes less transparent: the lamp power must be gradually increased during a growth run.
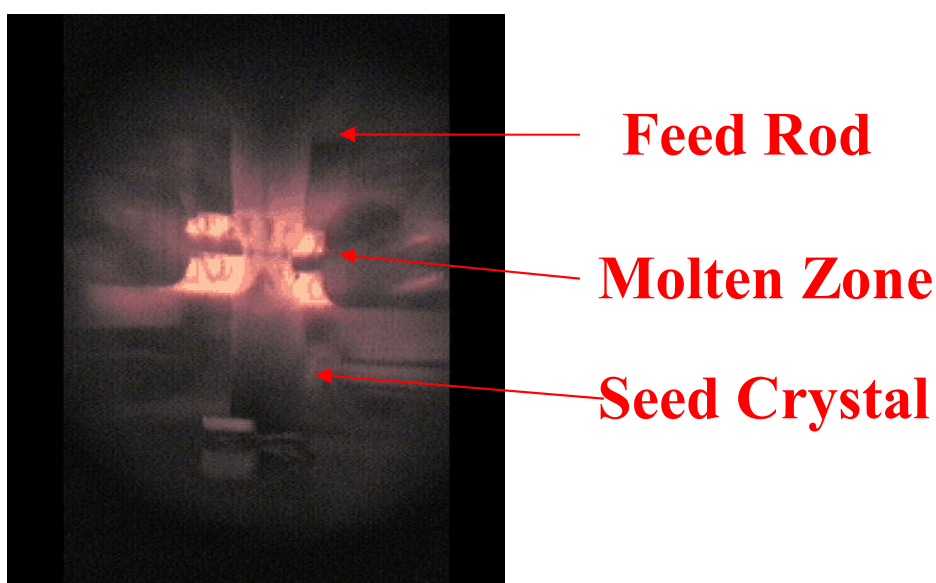
Figure 2.4. An image of the 'hot region' established within an image furnace.

The image furnace used for the growth of all crystals referred to in this thesis was supplied by NEC Machinery Corporation (SCI-MDH-11020). The hot-zone was observed via a CCD camera; this camera was linked to software which also allowed the lamp power and the various spindle speeds to be controlled. To initiate crystal growth the tip of the feed rod was lowered into the hot zone; the lamp power was then increased until this tip melted. The tip of the seed crystal was then raised upwards and connected with the liquid zone: this molten zone was observed to 'float' between the feed rod and the seed; crystal growth could then proceed. The liquid zone will not collapse if its surface tension is sufficient; an example of a molten zone is shown in Figure 2.4. The seed was lowered with velocity V_1 so that molten material was pulled out of the hot zone; the feed rod was simultaneously moved downwards with velocity V_2 so that the molten zone was continually replenished.

To become familiar with the image furnace and the floating zone method, the first few months of research involved the growth of crystals of Sr_2RuO_4. RuO_2 is evaporated onto the quartz tube during a Sr_2RuO_4 growth run but it was not necessary to use a cold trap: $n = 1.15$ for Sr_2RuO_4 corresponds to approximately 5% of the mass of feed rod being evaporated. Although RuO_2 could be seen on the inner surface of the quartz tube at the end of a Sr_2RuO_4 growth run, the tube was still transparent to IR radiation. The growth conditions for Sr_2RuO_4 were $V_1 = 45$ mm/hr, $V_2 \sim 32$ mm/hr, $\omega \sim 30$ rpm, $P \sim 3$ bars. Single crystals of Sr_2RuO_4 were grown quite straightforwardly and repeatedly and could be cleaved easily with a scalpel blade parallel to the *ab*-planes. These planes can be identified by the unaided eye because they are highly reflective of background light.

2.1.4 Growth of $Sr_3Ru_2O_7$ Crystals

Crystals of $Sr_3Ru_2O_7$ are more difficult to grow than Sr_2RuO_4 because a greater percentage of RuO_2 is evaporated during the growth process (due to the higher melting temperature of $Sr_3Ru_2O_7$) and, therefore, a stable molten zone is difficult to establish. $n = 1.33$ for $Sr_3Ru_2O_7$ corresponds to approximately 10% of the mass of the feed rod being evaporated during the growth process. It is therefore essential to use a cold-trap during a $Sr_3Ru_2O_7$ growth run. Furthermore, multi-layer ruthenates such as $Sr_3Ru_2O_7$ and $Sr_4Ru_3O_{10}$ are more susceptible than Sr_2RuO_4 to stacking faults and the probability of 'intergrowth' phases (i.e. different n in section 1.4.1) in these ruthenates is significant.

Attempts were made to grow crystals of $Sr_3Ru_2O_7$ in an image furnace, following the procedures described in the previous two sections and using the same primary growth parameters given by Perry and Maeno [7]: $n = 1.68$, $V_1 = 15$ mm/hr and $P = 10$ bars of a 90% Ar/10 % O_2 atmosphere. However, the growth of $Sr_3Ru_2O_7$ was problematic. Like the as-grown crystals of Sr_2RuO_4, the as-grown crystals of $Sr_3Ru_2O_7$ had four faces and could be cleaved with a scalpel blade parallel to the *ab*-planes quite easily. However, unlike the smooth, uninterrupted *ab*-planes of their Sr_2RuO_4 counterparts, the *ab*-planes of these as-grown $Sr_3Ru_2O_7$ crystals appeared heavily distorted to the

unaided eye. In particular, many striations – defect-lines at an angle of approximately 60° to the direction of crystal growth – were seen on the *ab*-planes. Additionally, the cleaving with a scalpel blade of these crystals was not as clean as the cleaving of Sr_2RuO_4 – small chunks of the crystal were observed to crumble away from the scalpel blade. Figure 2.5 shows the X-ray diffraction pattern obtained from a crushed sample of one of these as-grown crystals. The (0 0 2), (0 0 4) and (1 0 1) diffraction peaks of the bilayer phase are visible at $2\theta \sim 8$, 17 and 23°, respectively, but foreign, intergrowth peaks at $2\theta \sim 6$, 12, 18 and 22° are also evident. These peaks can be attributed to the (0 0 2), (0 0 4), (0 0 6) reflections of $Sr_4Ru_3O_{10}$ and the (1 0 1) reflection of $SrRuO_3$, respectively.
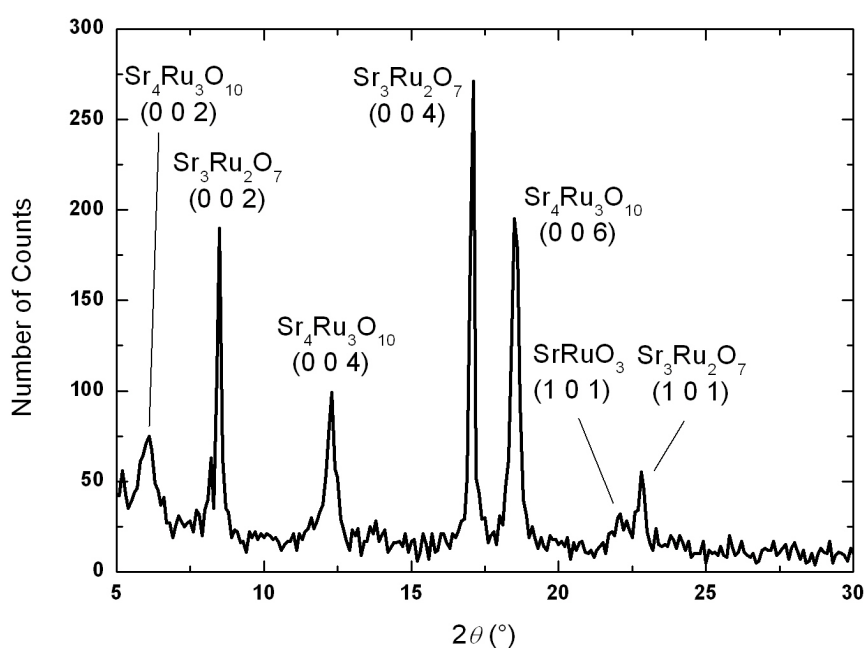
Figure 2.5. The X-ray diffraction pattern of a crystal of nominally-$Sr_3Ru_2O_7$, grown with $V_1 = 15$ mm/hr.

It was clear that these intergrowths arose because, in terms of the Sr-Ru-O phase diagram, the molten zone within the image furnace was not adjacent to the $Sr_3Ru_2O_7$ solid phase. Six attempts were made to grow $Sr_3Ru_2O_7$ using the original conditions. It was suspected that an unstable molten zone arose because radiation was not being distributed evenly throughout the hot-zone of the furnace. Growth attempts were made with pristine quartz tubes *and* also with tubes which had been used a number of times (and in which some recrystallisation of the quartz could be seen). Changing the

quartz tube did not have a noticeable effect on the as-grown crystals. An investigation of the crystal growth parameters was then initiated.
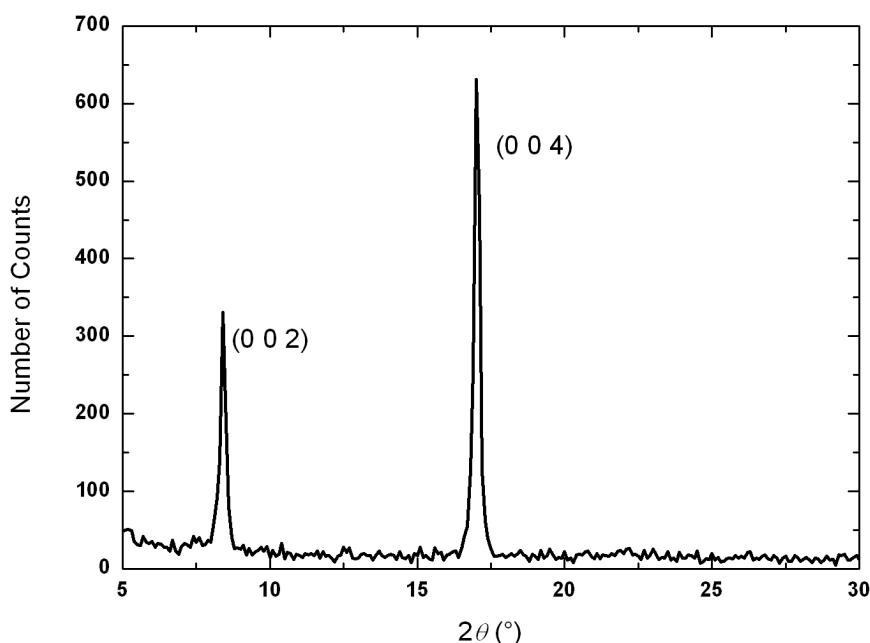
Figure 2.6. The X-ray diffraction pattern of a nominally-$Sr_3Ru_2O_7$ crystal, grown with $V_1 = 25$ mm/hr.

No attempt was made to change the content or pressure of the atmosphere. In particular, a large pressure is necessary to suppress RuO_2 evaporation. The initial RuO_2 excess *was* varied: various *n* values between 1.6 and 1.8 were tried, but no major changes to the as-grown crystals were evident. RuO_2 powder supplied by a different manufacturer was also used in the starting mixture, but no significant visual change of the as-grown crystals was apparent and Sr_2RuO_4 and $Sr_4Ru_3O_{10}$ intergrowths were also evident in X-ray diffraction patterns of these crystals.

A major breakthrough was made when the growth speed was changed from its original value of 15 mm/hr. The *n* parameter was changed back to 1.68 and growth runs with $V_1 = 5$ and 10 mm/hr were attempted. The product of these growth-runs was, in terms of crystalline quality, worse than the 15 mm/hr attempts: no faces could be seen on the outside of the deposited material which, furthermore, could not be

44

cleaved easily with a scalpel blade. A growth run with $V_1 = 25$ mm/hr was then tried. The crystals yielded from this run were of a *much* higher crystalline quality than any of the other as-grown crystals. The *ab*-planes of these crystals were very smooth, although a low density of minor interruptions were clear to the unaided eye. Relatively large pieces of single crystal were obtained from this growth run, with the high-quality *ab*-planes uninterrupted for a few centimetres along the direction of growth. Figure 2.6 shows the X-ray diffraction pattern of a crushed single crystal obtained from this growth run. No Sr_2RuO_4 or $Sr_4Ru_3O_{10}$ diffraction peaks are evident, hence confirming the relatively high crystalline quality.

Increasing the growth speed tends to narrow the molten zone and, hence, reduce the rate at which RuO_2 is evaporated. However, the previous batches of as-grown crystals did appear to be particularly Ru-deficient: the RuO_2 evaporation (deduced by measuring the masses of the feed- and seed-rods before and after growth) was always found to be approximately 10% of the mass of the initial feed rod, consistent with work in ref. 7. However, growth parameters are interdependent: varying any one of these parameters impinges on the others. All crystals of $Sr_3Ru_2O_7$ and cation-doped $Sr_3Ru_2O_7$ referred to in this thesis were obtained with a growth speed of 25 mm/hr. High-quality crystals have *not* always been obtained when growing at this speed – some of the as-grown crystals contained a significant intergrowth content. All of the Ti- and La-doped $Sr_3Ru_2O_7$ crystals (referred to in chapters 3 and 5, respectively) were found to contain an appreciable content (~ 1 - 10 molar percent) of $SrRuO_3$ and $Sr_4Ru_3O_{10}$ intergrowths. Also, the residual in-plane resistivity of the best $Sr_3Ru_2O_7$ crystals referred to in this thesis is 1.1 μΩcm, significantly larger than the 0.4 μΩcm measured in ultraclean crystals [7], thus hinting at some structural defects due to intergrowths. No further attempts were made to alter the growth speed (by small amounts, say 1mm/hr); the $Sr_3Ru_2O_7$ crystals yielded from some of the 25 mm/hr growth runs were judged to be worthy of further study and are referred to in the appendix. Furthermore, it was expected that the cation-doping levels proposed for the work described in this thesis would enhance *significantly* the residual resistivity, because of additional elastic scattering. Overall, the 1.1 μΩcm $Sr_3Ru_2O_7$ resistivity baseline was deemed to be acceptable.

2.2 Chemical Characterisation

2.2.1 X-ray Diffraction

The X-ray diffraction patterns shown in Figures 2.5 and 2.6 were obtained with a Philips X-ray diffractometer in the School of Chemistry at the University of St Andrews. The bilayer $Sr_3Ru_2O_7$ crystal structure has a series of characteristic X-ray lines related to its lattice parameters by the Bragg condition, $n\lambda = 2d\sin\theta$. If intergrowth ruthenate phases such as Sr_2RuO_4, $SrRuO_3$ or $Sr_4Ru_3O_{10}$ are present in appreciable amounts in nominally-$Sr_3Ru_2O_7$ crystals, some of the characteristic X-ray lines of these structures should be evident in an X-ray diffraction pattern.

X-ray diffraction patterns of all crystals referred to in this thesis were obtained from a small mass (~ 20 mg) of crushed as-grown crystal, fixed with ethanol onto an aluminium plate. This plate was subsequently placed into a slot in the chamber of the diffractometer and irradiated with Cu K_α X-rays ($\lambda = 0.154$ nm). The X-ray detector could be scanned through the scattering angle, 2θ, between 5 and 90° by controlling with a software package.

2.2.2 Energy Dispersive X-ray Analysis

There is no *a priori* reason why the concentration of dopant ions in crystals of cation-doped $Sr_3Ru_2O_7$ should be equal to the nominal concentration of these ions (i.e. in the starting mixture of powders). It was, therefore, necessary to measure the doping level of each as-grown crystal. One way of making such a measurement is to use *Electron Probe Microanalysis*, in which a focused beam of high energy electrons is bombarded into the sample under investigation. Some of these electrons cause inner-shell ionisation of the constituent atoms of the sample. As a result of such ionisation an X-ray photon is emitted each time an inner shell vacancy is created. Each atom in the Periodic Table has a *characteristic* set of X-ray lines: identification of the constituent atoms is made possible by detecting the X-rays emitted from the sample. Furthermore,

quantitative analysis of sample composition is possible if the intensities of the X-ray lines from the sample are compared to the intensities of X-ray lines from materials of a known composition.
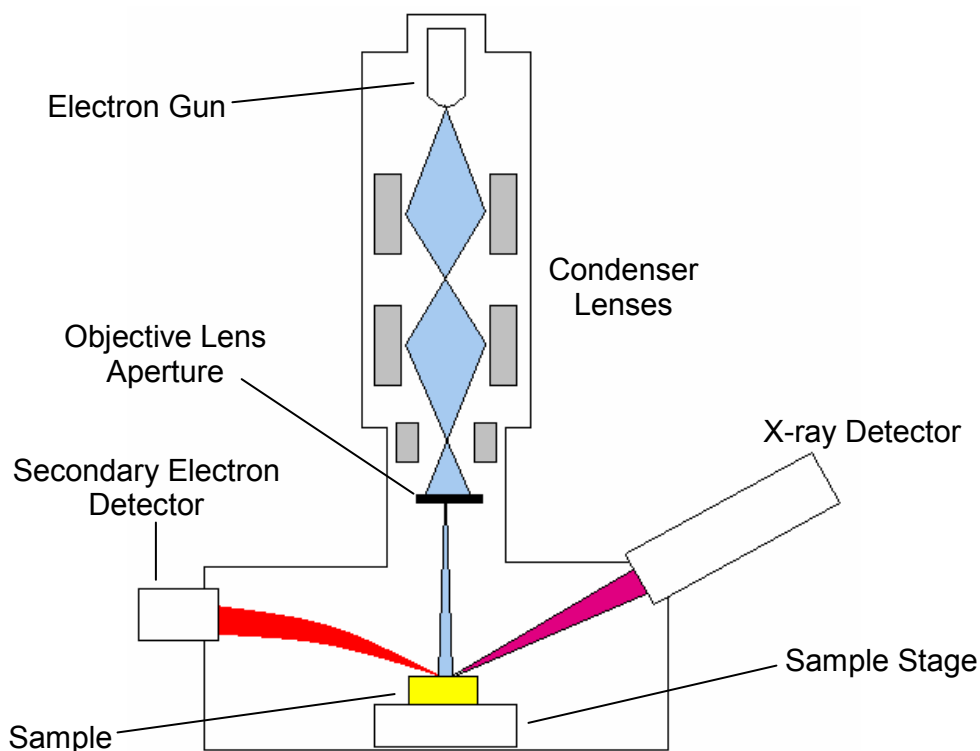
Figure 2.7. A schematic of an electron microprobe with an energy dispersive X-ray detector. Adapted from diagrams in [11] and [12].

The emitted X-rays can be detected as a function of their wavelength or their energy. The latter type of detection, known as *Energy Dispersive X-ray Analysis* (EDX), has been used to quantify the content of dopant ions in the cation-doped $Sr_3Ru_2O_7$ crystals referred to in this thesis. EDX measurements were made in the School of Chemistry at the University of St Andrews with a JEOL JSM 5600 Scanning Electron Microscope (SEM) in conjunction with an X-ray detector and INCA analysis software from Oxford Instruments.

Reed [10] describes in much detail how a typical electron probe system works; Figure 2.7 shows a schematic of an electron probe system. The electron gun is a tungsten filament heated to ~ 2700 K by passing a current through it; a high voltage (typically 10 - 30 kV) applied to his filament causes thermionic emission. Electrons are then

accelerated towards the sample to be investigated; the electron beam is focussed by magnetic lenses onto a plane at which the sample is located. Penetration of the electron beam into the sample leads to the generation of characteristic X-rays in addition to a Bremsstrahlung background. The X-rays emitted from a sample are incident upon a solid state detector, the central component of which is a semiconductor crystal, immersed in a Dewar of liquid nitrogen (to reduce thermal noise).

For quantitative microanalysis the X-ray spectra of samples of a known composition, known as *standards*, must be measured in addition to the spectra of the unknown samples; the electron beam current must also be known. Crystals of $Sr_3Ru_2O_7$ doped with lanthanum, chromium or titanium cations are referred to in this thesis: $BaTiO_3$ (for Ti-doped $Sr_3Ru_2O_7$) and $LaCrO_3$ (for La- and Cr-doped $Sr_3Ru_2O_7$) were used as standards, both of which were highly-polished and mounted in metallic epoxy. A high-purity crystal of Sr_2RuO_4 (with a measured superconducting T_c of approximately 1.4 K, similar to the optimum value) was used as the standard for ruthenium and strontium ions.

For each batch of cation-doped $Sr_3Ru_2O_7$ a crystal was mounted on the same surface as the appropriate standard. Care was taken to ensure that the exposed *ab*-plane of the crystal was horizontal and, hence, normal to the direction of the electron beam. Furthermore, a fine copper mesh was mounted alongside the unknown sample; the sample and mesh were then mounted on conductive carbon double-sided adhesive discs and placed onto the metallic standard block. This block was then placed into the microscope chamber, which was subsequently evacuated. The accelerating voltage across the tungsten filament was then set to 30 kV. Smooth surface areas were located with the SEM secondary-electron imaging software. The *working distance*, the distance between the pole piece of the magnetic condenser lens and the plane onto which the electron beam is focussed, was always set to 20 mm, the distance for which microanalysis is optimised in this system. Prior to the measurement of an unknown sample or a standard, an X-ray spectrum of the copper mesh was recorded and the INCA software subsequently reported the beam current as "100 %". The X-ray spectrum of the standard was then acquired over a four-minute period; the X-ray spectrum of the unknown sample was subsequently measured, also over a four minute

period. Finally, the spectrum of the copper mesh was recorded again and the INCA software reported the beam current as a percentage of the previous measurement. The beam current was typically found to vary by up to ± 5% over the ~ 15 minute period in which grid-standard-sample-grid measurements were made. For each unknown sample, at least five X-ray spectra were recorded, from different regions of the surface. EDX measurements have been made on at least three crystals from each batch.
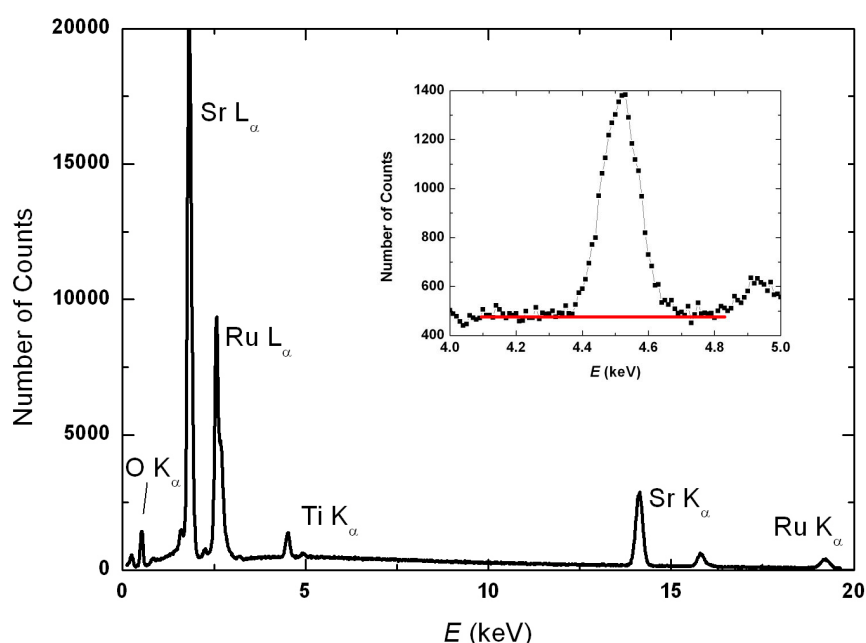
Figure 2.8. The X-ray spectrum of a crystal of $Sr_3(Ru_{1-x}Ti_x)_2O_7$. The inset shows the titanium K_α peak in more detail; a solid line has been placed through the X-ray background, taken to be independent of E in this range of energies.

The X-ray spectrum of a $Sr_3(Ru_{1-x}Ti_x)_2O_7$ crystal is shown in Figure 2.8. Characteristic peaks are clearly seen above the Bremsstrahlung background. The inset to Figure 2.8 shows the titanium K_α peak in more detail. For quantitative analysis a background must be subtracted – in the example shown a constant background of 480 ± 20 counts has been assumed. Regarding $(Sr_{1-y}La_y)_3Ru_2O_7$ spectra it is also reasonable to subtract an energy-independent background from the lanthanum L_α peak at $E = 4.6$ keV. The K_α peak of chromium is located at 5.4 keV, in an energy range over which the number of background counts decreases slowly as a function of E: it

has been found for $Sr_3(Ru_{1-x}Cr_x)_2O_7$ X-ray spectra that the background is proportional to $-E$ in the region of the Cr K_α peak.

Characteristic X-ray intensities are, to a first approximation, proportional to the mass concentration of the particular element in the unknown material [10]. This approximation arises because incident electrons lose their kinetic energy mainly through interactions with *orbital* electrons of atoms in the material, the number of which is approximately proportional to atomic mass. Incident electrons therefore penetrate an approximately constant mass in different materials. The intensity, I, of a given characteristic peak has been taken as the sum of counts over the FWHM of the peak. For $Sr_3(Ru_{1-x}Ti_x)_2O_7$ the concentration, x, of titanium cations was deduced from the following equation:

$$\frac{I_{Sample}}{I_{Standard}} = \frac{2xM_{Ti}/M_{Sample}}{M_{Ti}/M_{Standard}}, \qquad (2.3)$$

where the intensity of the Ti K_α peak from the sample and the $BaTiO_3$ standard is I_{Sample} and $I_{Standard}$, respectively. Molar masses are denoted by M; the molar mass of $BaTiO_3$ and $Sr_3(Ru_{1-x}Ti_x)_2O_7$ is 233.21 and $(577 - 106.34x)$ grams, respectively. An equation with similar form has also been used for samples of $Sr_3(Ru_{1-x}Cr_x)_2O_7$ and $(Sr_{1-y}La_y)_3Ru_2O_7$, in conjunction with the $LaCrO_3$ standard.

Measured X-ray intensities should be corrected to take account of processes associated with absorption, fluorescence and the X-ray 'stopping power' of a specimen, which depends on atomic number, Z. Reed [10] describes how these 'ZAF' matrix corrections can be made; an iterative procedure must be followed because these corrections depend on sample composition. The INCA analysis software makes these ZAF corrections; on the other hand, Equation 2.3 refers to *uncorrected* intensities. However, the concentration of dopant cations in the samples referred to in this work have always been in good agreement (within 10%) of the concentrations reported by the INCA software. This observation confirms that the ZAF corrections are relatively small and, hence, justifies the omission of these corrections from the quantitative analysis.

2.3 Cryogenic Apparatus

Measurements of the DC magnetisation, heat capacity, resistivity as a function of temperature and magnetoresistance of cation-doped $Sr_3Ru_2O_7$ crystals are reported in chapters 3-5. The DC magnetisation, resistivity and magnetoresistance of samples have been measured in St Andrews; heat capacity measurements were made at the Centre for Science at Extreme Conditions at the University of Edinburgh. The apparatus with which these measurements have been made are based upon well-known physical processes; Pobell [13], for example, provides a comprehensive description of cryogenic equipment and the relevant physics.

2.3.1 Resistivity Measurements in a Continuous Flow Cryostat

Temperature may be controlled between 300 and 4 K by balancing with a heater the cooling power of the gas evaporating from liquid helium: this is the basis of a *continuous flow cryostat*. A sample probe is contained within a volume (known as the sample space) flushed with helium exchange gas and surrounded by a heat exchanger. Liquid helium from a storage Dewar is supplied to the cryostat via an insulated transfer tube; this liquid flows through the heat exchanger and is then returned to a recovery system via an exhaust. A thermometer and a heater coil are mounted on the heat exchanger; when used in conjunction with an external temperature controller the temperature of the heat exchanger can be controlled.

Measurements of electrical resistivity of samples between 300 and 4K have been made with the samples mounted within a continuous flow cryostat supplied by Oxford Instruments; the external temperature controller was also an Oxford Instruments model (ITC 502). In each measurement run two crystals were mounted on the sample probe and, so that the voltage from both sides of each of these bar-shaped crystals could be measured, four lock-in amplifiers (LIA's) were used. Each crystal was mounted onto a quartz substrate which was attached with double-sided tape onto the sample probe.

Figure 2.9 shows how quasi-2D materials such as $Sr_3Ru_2O_7$ may be mounted such that their in-plane electrical resistivity can be measured. Current connections are made at each end of the crystal (the ideal shape of which is a long, narrow and thin bar); voltage contacts are made on opposite sides of the crystal. *Four* voltage wires are shown in Figure 2.9 because it has been desirable to measure voltage across *both* of the longest sides, to confirm macroscopic homogeneity. The electrical connections were made with gold wires (50 μm diameter) attached onto the crystal with a high-temperature silver paint (Dupont 6838, cured for 5 minutes in air at $T = 450$ °C). The gold wires are then fixed onto a quartz substrate, above which the crystal is mounted.
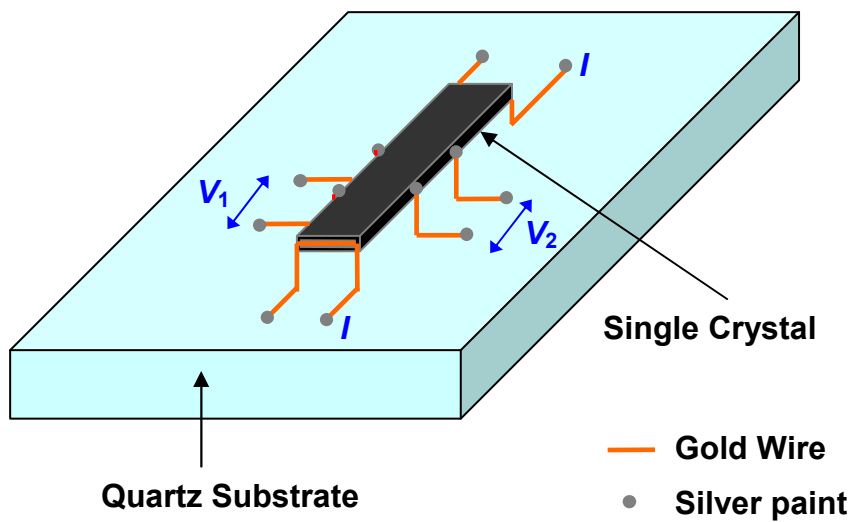
Figure 2.9. An illustration of how crystals have been mounted for resistivity measurements. The exposed *ab*-planes (top and bottom surfaces) of the crystal are parallel to the top surface of the substrate.

The interplane chemical bonding in $Sr_3Ru_2O_7$ is relatively weak – $Sr_3Ru_2O_7$ crystals can be cleaved rather easily parallel to the *ab*-planes with a with a scalpel blade. It has been quite straightforward to cut $Sr_3Ru_2O_7$ into wafer-like pieces ~ 100 μm thickness for resistivity measurements. The resistivity of a bar-shaped sample is

$$\rho_{ab} = R\frac{tw}{l}, \tag{2.4}$$

where R is the resistance of the sample (= V/I for Ohmic conduction), t and w are the thickness and width of the sample, respectively and l is the distance between the two

voltage wires. Equation 2.4 is applicable to quasi-2D metals such as $Sr_3Ru_2O_7$ if it assumed that the individual *ab*-planes of a crystal are in parallel with each other.

Values of *w* and *l* of most crystals were O(1mm) and could be deduced from visual inspection through a high-powered optical microscope. The uncertainty of each these quantities was approximately ±10 %; for the shortest (small *l*) crystals studied, $\Delta l \sim \pm$ 20 %. The thickness of most crystals was O(0.1mm), with $\Delta t \sim \pm$ 20 %. So that the total uncertainty of each ρ_{ab} could be reduced at least five crystals from each as-grown batch of cation-doped $Sr_3Ru_2O_7$ have been measured. Care was taken to ensure that the top and bottom faces of each crystal were parallel to each other: trapezoidal-shaped crystals are undesirable because of the high-resistance *c*-axis current paths in them; equation 2.4 would not be valid for such crystals. All resistivity measurements were made with a Stanford SR380 LIA in the differential mode; a time constant of 1 second and a reference frequency of 90 Hz were consistently used.

2.3.2 Adiabatic Demagnetisation Refrigerator

Temperatures much lower than 4 K can be attained by *magnetic cooling* [14, 15, 16]; the apparatus in which magnetic cooling can be utilised is known as an *adiabatic demagnetisation refrigerator* (ADR). A schematic diagram of the essential parts of an ADR is shown in Figure 2.10. The sample stage is in good thermal contact to a refrigerant pill, a paramagnetic salt with a large moment on each magnetic ion. This pill is located within the bore of a demagnetisation magnet and is also connected to a thermal bath via a heat-switch: if this heat-switch is opened, thermal contact between the pill and the thermal bath is suppressed.

To initiate the cooling process the heat-switch must be closed, allowing good thermal contact between the pill and the thermal bath to be made. The demagnetisation magnet is then ramped up to its maximum field value and the refrigerant pill is subsequently isolated from the bath by opening the heat-switch. The demagnetisation magnet is then ramped down to zero field: this demagnetisation process is adiabatic because the pill/sample system does not, in principle, exchange any heat with the surroundings. As the demagnetisation magnet is ramped down the magnetisation of

the pill decreases. The demagnetisation process is reversible: because there is no change in entropy of the combined pill-sample system, entropy must be *exchanged* between the pill and the sample stage. If the entropy of the pill increases by ΔS the entropy of the sample stage must decrease by ΔS, resulting in a decrease in the temperature of the sample stage.
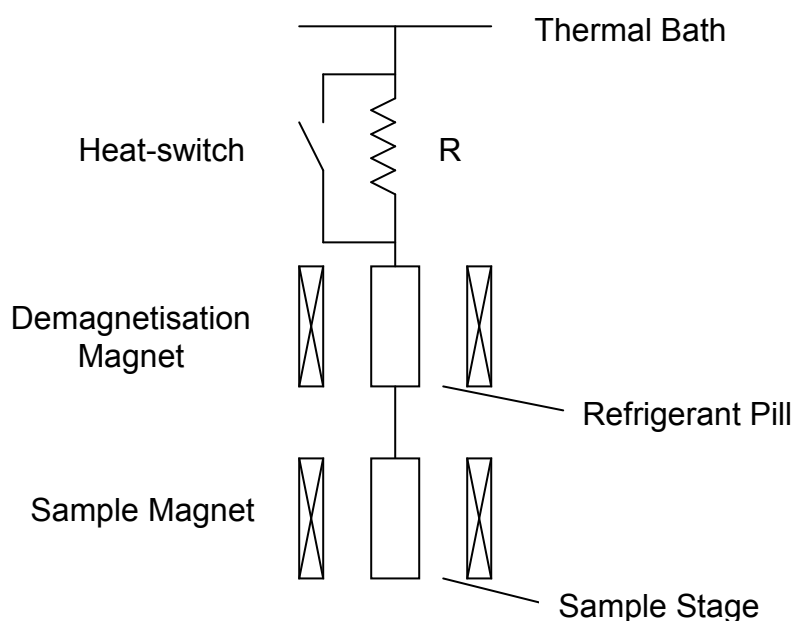
Figure 2.10. A schematic diagram of an ADR. Copied from [16].

An ADR supplied by Cambridge Magnetic Refrigeration has been used to measure resistivity of samples as a function of temperature at temperatures below 5 K and also resistivity as a function of magnetic field (magnetoresistance) at fixed temperatures. This system incorporates an 8 Tesla superconducting magnet around the sample space in addition to a 6.5 Tesla demagnetisation magnet. The heat-switch is mechanical, operated by a rotary mechanism at room temperature. The system can be cooled to 4.2K by placing a small amount of helium exchange gas is into the inner vacuum chamber (IVC); further cooling to approximately 1.45 K is made possible by a 1 K pot, the foundation of which is evaporative cooling of liquid helium. A base temperature of approximately 95 mK after demagnetisation can be achieved with this system.

2.3.3 Dilution Refrigerator

The cooling power of an adiabatic demagnetisation refrigerator is not continuous and the base temperature can only be held for a short time. By contrast, continuous cooling can be achieved with a *dilution refrigerator* [17]. When a mixture of ^{3}He and ^{4}He isotopes is cooled below 0.87 K it separates into two distinctive phases: a lighter "concentrated" ^{3}He-rich phase and a heavier "dilute" phase, rich in ^{4}He. The ^{4}He is superfluid and does not interact with the ^{3}He atoms in this dilute phase. The enthalpy of a ^{3}He atom is larger in the dilute phase than in the concentrated phase: cooling can occur if some of the ^{3}He from the concentrated phase is evaporated into the dilute phase. Such evaporation corresponds to "dilution" of the ^{3}He-rich phase. Even as $T \rightarrow$ 0 a finite amount of ^{3}He remains in the dilute phase and very low temperatures can be attained by the dilution process.

The physical processes involved in dilution refrigeration are described in detail by Pobell [13] and also in literature from Oxford Instruments [17, 18]. The boundary between the two phases of the ^{3}He/^{4}He mixture occurs at the mixing chamber and cooling occurs by evaporation of ^{3}He from the concentrated phase into the dilute phase. ^{3}He must be continually removed from the dilute phase and then returned to the concentrated phase via the still (to which an osmotic pressure gradient is established) and then the condenser.

The dilution refrigerator in St Andrews, supplied by Oxford Instruments, incorporates a 15 Tesla sample magnet. The ^{3}He/^{4}He closed system and the 1K pot are contained inside an IVC, within a Dewar of liquid helium; initial cooling of the system to 4.2 K is achieved with exchange gas in the IVC. The dilution refrigerator was used for some of the magnetoresistance measurements referred to in this thesis; the sample probe used for these measurements could accommodate up to six samples in four-probe configurations. This sample probe was bolted to the mixing chamber, on which a ruthenium oxide thermometer and a heater coil were located. The polar angle of the sample stage was varied by a rotary mechanism operated at room temperature.

2.3.4 MPMS SQUID Magnetometer

The DC magnetisation of samples has been measured with a Magnetic Properties Measurement System (MPMS) supplied by Quantum Design. The cornerstone of the MPMS is a Superconducting Quantum Interference Device (SQUID) magnetometer. A SQUID utilises the properties of electron-pair wave coherence and Josephson junctions to measure magnetic flux [20, 21]. The sample to be investigated was mounted in a plastic straw and fixed onto one end of a metal rod. Quasi-2D materials such as $Sr_3Ru_2O_7$ can be mounted so that either the *ab*-planes or the *c*-axis are parallel to the external magnetic field. For $B \parallel ab$ the sample can be sandwiched within a second plastic straw placed inside the main straw. For $B \parallel c$ a second straw is also used, and the sample is fixed in place with a very small amount of grease. The straws, recommended by Quantum Design, are made from clear (rather than coloured) plastic and have a very small magnetic susceptibility.

The end of the metal rod to which the sample straw is attached is made from quantalloy; the other end of this rod is made from stainless steel and is connected to a stepper motor. The sample may be moved up and down through a set of pickup coils, which are connected to the SQUID with superconducting wires. Voltages are read as a function of the sample's position in the pickup coils; the MPMS computes the magnetic moment of the sample with a measurement algorithm. The external magnetic field may be varied up to a maximum of 5 Tesla and the temperature range of the system is 1.8 - 400 K.

2.3.5 PPMS Heat Capacity Option

The heat capacity of as-grown crystals has been measured with a relaxation method in a Physical Properties Measurement System (PPMS) supplied by Quantum Design [22]. Figure 2.11 shows a schematic diagram of how heat capacity may be measured by a relaxation method. The sample to be investigated is situated on a platform and thermal contact between this platform and the sample is made via a thin layer of grease. The platform is also in contact to a thermal bath, the puck in which the setup is contained. Thermal contact between the platform and the puck is made with wires

of a known conductance, K_w. A thermometer and a heater are also fixed to the sample platform and the entire setup is located within an evacuated chamber.
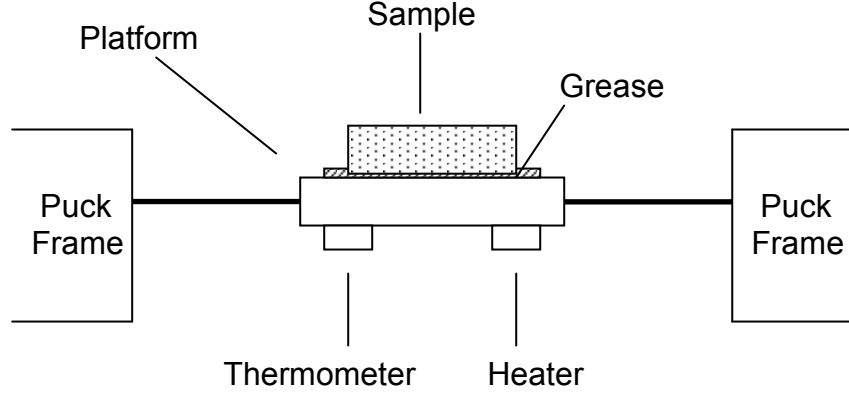
Figure 2.11. A schematic diagram of the setup used for measuring the heat capacity of a sample with a relaxation method. From [22].

A constant power, P_0, is applied from the heater for a known amount of time and this heating period is followed by a cooling period of the same duration. If the sample and the platform are in thermal equilibrium and at the same temperature, T, the total heat capacity, C, of the sample and the platform is

$$C\frac{dT}{dt} = -K_w(T - T_p) + P(t),$$ (2.5)

where T_p is the temperature of the puck, measured by a thermometer buried within its body. $P(t) = P_0$ during heating and is zero during cooling. The temperature of the platform rises or falls to an equilibrium value in a time τ,

$$T(t) = T(0)(1 + \Delta T \exp(-t/\tau)),$$ (2.6)

where $\Delta T = P_0/K_w$. It is clear from Equation 2.5 that during this cooling period $C = K_w\tau = P_0\tau/\Delta T$. C can therefore be deduced by observing the relaxation of the sample temperature [23].

Heat capacity measurements have been made between temperatures of 30 and 0.4 K. Cooling to such low temperatures is achieved by utilising the properties of ^{3}He. The liquid of this isotope evaporates at 3.2 K at atmospheric pressure but, with the use of

evaporative cooling, temperatures as low as 0.3 K can be attained in ^{3}He refrigerators [131]. The sample platform is covered by a radiation shield and the puck is then placed at the end of a long experimental insert. A ^{3}He pot is also located near the same end of this insert, and is in thermal contact with the puck. The insert is lowered into a chamber within a Dewar of liquid helium. At the other end of the insert is situated a turbo pump which promotes evaporative cooling of the ^{3}He from its pot. The heat capacity of the grease-covered platform, $C_{addenda}(T)$, must be measured as a function of temperature before the heat capacity of a sample plus platform, $C_{total}(T)$. The heat capacity of the sample is the difference of these two measurements: $C_{sample}(T) = C_{total}(T) - C_{addenda}(T)$.

2.4 References

[1] F. Lévy, I. Sheikin, B. Grenier and A. D. Huxley, Science **309**, 1343 (2005)

[2] N. Doiron-Leyraud, C. Proust, D. LeBoeuf, J. Levallois, J. Bonnemaison, R. Liang, D. A. Bonn, W. N. Hardy and L. Taillefer, Nature **447**, 565 (2007)

[3] G. Cao, S. McCall and J. E. Crow, Phys. Rev. B **55**, R672 (1997)

[4] G. Cao, L. Balicas, W. H. Song, Y. P. Sun, Y. Xin, V. A. Bondarenko, J. W. Brill, S. Parkin and X. N. Lin, Phys. Rev. B **68**, 174409 (2003)

[5] P. W. Atkins, *Physical Chemistry* (6th Edition), Oxford University Press (1998)

[6] R. S. Perry, PhD Thesis, University of Birmingham (2001)

[7] R. S. Perry and Y. Maeno, J. Cryst. Growth **271**, 134 (2004)

[8] Z.Q. Mao, Y. Maeno and H. Fukazawa, Mat. Res. Bull. **35**, 1813 (2000)

[9] M. Zhou, J. Hooper, D. Fobes, Z.Q. Mao, V. Golub and C.J. O'Connor, Mat. Res. Bull. **40**, 942 (2005)

[10] S. J. B. Reed, *Electron Microprobe Analysis* (2nd Edition), Cambridge University Press (1993)

[11] http://www.mcswiggen.com/TechNotes/WDSvsEDS.htm

[12] http://serc.carleton.edu/17054

[13] F. Pobell, *Matter and Methods at Low Temperatures*, Springer-Verlag (1992)

[14] S. J. Blundell, *Magnetism in Condensed Matter*, Oxford University Press (2001)

[15] F. Mandl, *Statistical Physics* (2nd Edition), Wiley (1988)

[16] mFridge mF-ADR/50 System Manual, Cambridge Magnetic Refrigeration (2001)

[17] H. London, G. R. Clarke and E. Mendoza, Phys. Rev. **128**, 1992 (1962)

[18] Kelvinox Operator's Handbook, Oxford Instruments

[19] N. H. Balshaw, *Practical Cryogenics*, Oxford Instruments (2001)

[20] MPMS XL Manual, Quantum Design

[21] J. F. Annett, *Superconductivity, Superfluids and Condensates*, Oxford University Press (2004)

[22] PPMS Manual, Quantum Design

[23] C. Bergemann, *Experimental Techniques*, Superconductivity Winter School, University of Cambridge (2005)

3. $Sr_3(Ru_{1-x}Ti_x)_2O_7$

3.1 Motivation

As discussed in section 1.4.5, some of the electronic properties of $Sr_3Ru_2O_7$ are sensitive to crystalline disorder. Such disorder can be structural defects, crystalline vacancies or impurity ions; these features can arise during the preparation and growth of $Sr_3Ru_2O_7$ crystals. It is, however, desirable to investigate the influence of disorder on the properties of $Sr_3Ru_2O_7$ in a *controlled* manner. Deliberately substituting foreign cations into the lattice of $Sr_3Ru_2O_7$ is one way of making a controlled study of the influence of disorder on the electronic properties of this metallic ruthenate.

Titanium cations have previously been substituted onto the ruthenium lattice sites in Sr_2RuO_4 [1-3], $SrRuO_3$ [4,5], $Ca_3Ru_2O_7$ [6] and $CaRuO_3$ [7] and titanium was, therefore, judged to be a suitable candidate for doping onto the Ru sites in $Sr_3Ru_2O_7$. It is believed that titanium cations are in the tetravalent state ($3d^0$) when substituted onto Ru^{4+} sites in Ruddlesden-Popper ruthenates. When in a 6-coordinate octahedral environment Ti^{4+} and Ru^{4+} cations have very similar ionic radii, 60.5 and 62 pm, respectively [8]: Ti-doping into Ruddlesden-Popper ruthenates is not expected to induce any major changes to the crystal structure. Furthermore, theoretical studies of the electronic structures of $Sr_2Ru_{1-x}Ti_xO_4$ [9] and $SrRu_{1-x}Ti_xO_3$ [10] indicated that Ti^{4+} orbitals do not hybridise with the conducting Ru-O network: Ti-doping was found to disrupt the Ru-O current paths and cause an increase in electrical resistivity. Although Ti^{4+} is a nonmagnetic cation Ti-doping has been shown to trigger magnetic ordering in $CaRuO_3$ and Sr_2RuO_4, both of which are paramagnetic metals. Minakata and Maeno [1] reported local-moment magnetism when $x \geq 0.025$ in single crystals of $Sr_2Ru_{1-x}Ti_xO_4$; He and Cava [7] discovered ferromagnetic ordering in powdered samples of $CaRu_{1-x}Ti_xO_3$ when $x \geq 0.02$.

Prior to the beginning of this research no work on $Sr_3(Ru_{1-x}Ti_x)_2O_7$ had been reported but, during its execution, a parallel study by an American group was published: Hooper *et al.* [11] reported measurements of the transport, magnetisation and heat

capacity of single crystals of $Sr_3(Ru_{1-x}Ti_x)_2O_7$ ($x \leq 0.08$). Although some of the results reported in this chapter are in qualitative agreement with the work in ref. 11 the primary conclusions of the experimental work reported in this chapter extend far beyond those of Hooper and colleagues. Furthermore, some of the results reported here have been complemented by neutron scattering measurements made by collaborating researchers [12]. The combination of these works has allowed an unambiguous conclusion to be reached: a spin density wave emerges as a function of Ti-doping in the $Sr_3(Ru_{1-x}Ti_x)_2O_7$ series. This fact was not picked up by the study in ref. 11.

Although most of the recent attention paid to $Sr_3Ru_2O_7$ is because of studies of ultrapure single crystals, the crystalline disorder due to titanium substitution reported in this chapter has been an *essential* component of experiments in which an unparalleled study of the electronic physics of $Sr_3Ru_2O_7$ has been made. These experiments, made by collaborating researchers on crystals provided from this work, involved scanning tunnelling microscopy and are referred to in the discussion of this chapter. Similar experiments have previously shed much light on the physics of the high-T_c cuprates [13,14], most of which are heavily disordered. Ongoing STM experiments on crystals of $Sr_3(Ru_{1-x}Ti_x)_2O_7$ from the work reported here are unique because they offer an insight into a *clean* (aside from the relatively small, controlled concentration of titanium cations) narrow-band metal and, therefore, provide a helpful contrast to STM experiments on cuprates, materials in which disorder cannot be easily controlled.

3.2 Crystal Growth and Chemical Characterisation

Batches of $Sr_3(Ru_{1-x}Ti_x)_2O_7$ were prepared by mixing RuO_2, TiO_2 and dried $SrCO_3$ powders in the ratio (1-x)2.52: 2x: 3. The mixed powder was then reacted and formed into a feed-rod using the methods described in section 2.1.2. Attempts were then made to grow crystals in an image furnace. The primary growth parameters for *all* of the cation doped crystals referred to in this thesis were the same as those of undoped $Sr_3Ru_2O_7$, referred to in section 2.1.4. Approximately 25 growth runs were attempted.

3.2.1 X-Ray Diffraction

Some of the as-grown $Sr_3(Ru_{1-x}Ti_x)_2O_7$ crystals were judged to be unsuitable for further study: the texture of these crystals was similar to that of the poor quality $Sr_3Ru_2O_7$ crystals referred to in section 2.1.3; many striations on the *ab*-planes of these crystals were clear to the unaided eye. X-ray diffraction also indicated that the (Ti-doped) trilayer phase was a major constituent of these crystals. However, the *ab*-planes of sections of some of the as-grown crystals did not appear to have such a high concentration of striations and were considered for further measurements. X-ray diffraction patterns from these sections were obtained; Sr_2RuO_4, $SrRuO_3$ and $Sr_4Ru_3O_{10}$ diffraction peaks were seen in *all* of these patterns, although to a much lesser extent than in Figure 2.5. The quantitative extent of the ferromagnetic intergrowth phases in these crystals is determined in terms of their magnetisation in section 3.3.1.

3.2.2 Energy Dispersive X-ray Analysis

The concentration of titanium cations in each batch of $Sr_3(Ru_{1-x}Ti_x)_2O_7$ was deduced by considering the Ti K_α X-ray line centred at $E = 4.51$ keV. The Ti x values were calculated using the analysis described in section 2.2.2. The nominal and measured x values of each batch, x_n and x_a, respectively, are given in Table 3.1. For each batch these two quantities are equal, within errors.

Batch and Nominal x	x_a
Ti23, $x_n = 0.005$	0.0046 ± 0.0013
Ti15, $x_n = 0.01$	0.0098 ± 0.0010
Ti8, $x_n = 0.025$	0.023 ± 0.004
Ti21, $x_n = 0.05$	0.051 ± 0.005
Ti9, $x_n = 0.075$	0.0072 ± 0.008
Ti7, $x_n = 0.1$	0.095 ± 0.007

Table 3.1. The nominal and actual titanium concentration of each batch of $Sr_3(Ru_{1-x}Ti_x)_2O_7$.

3.3 Magnetisation

3.3.1 Intergrowth Contributions

$SrRuO_3$ and $Sr_4Ru_3O_{10}$ intergrowth phases in each batch of $Sr_3(Ru_{1-x}Ti_x)_2O_7$ are expected to make a significant contribution to the DC magnetisation of these materials. Shown in Figure 3.1 is the field-cooled DC susceptibility of $Sr_3(Ru_{1-x}Ti_x)_2O_7$, $x = 0$, 0.01 and 0.025, obtained with an applied field of 0.3 Tesla (the same field used in ref. 11). The peak in $\chi(T)$ of each sample is associated with the majority $Sr_3(Ru_{1-x}Ti_x)_2O_7$ phase. The low temperature susceptibility of $x = 0.01$ and 0.025 is, however, *many* times larger than the low temperature susceptibility of $Sr_3Ru_2O_7$ and is therefore inconsistent with data in ref. 11. Kinks in $\chi(T)$ of the Ti-doped samples are also seen at $T \sim 100$ and 160 K but such kinks are absent from the susceptibility of $Sr_3Ru_2O_7$. The kinks in $\chi(T)$ and the very large low temperature susceptibilities can be attributed to (Ti-doped) $SrRuO_3$ and $Sr_4Ru_3O_{10}$ intergrowth phases. It is therefore desirable to estimate the molar percentages of each of these phases in as-grown crystals of $Sr_3(Ru_{1-x}Ti_x)_2O_7$.
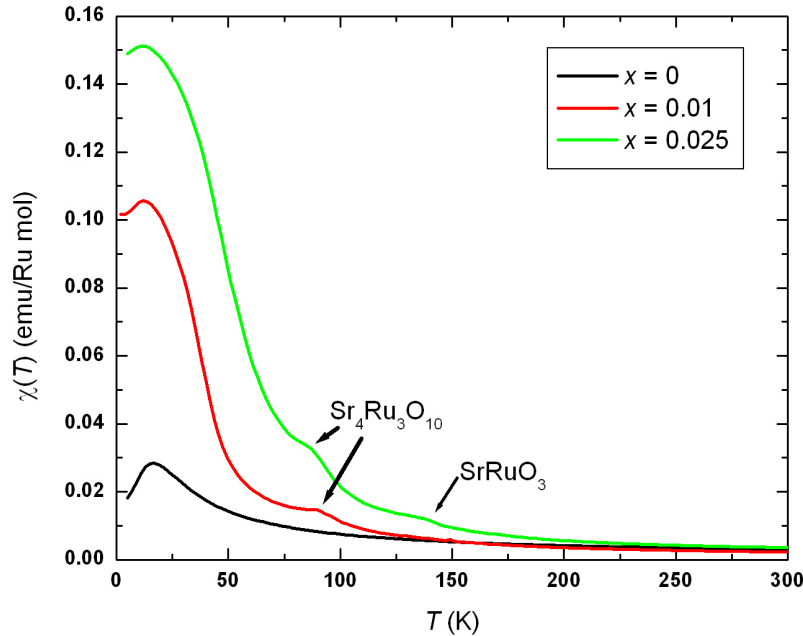

Figure 3.1. The field-cooled DC susceptibility of $x = 0$, 0.01 and 0.025 as a function of temperature, with $B = 0.3$ T.

It is clear that, compared to either of the Ti-doped crystals, the $Sr_3Ru_2O_7$ crystal indicated in Figure 3.1 contains a much smaller percentage of ferromagnetic intergrowths. $SrRuO_3$ and $Sr_4Ru_3O_{10}$ intergrowths can, however, occur in crystals of undoped $Sr_3Ru_2O_7$. Described here is a procedure for estimating the molar percentages of $SrRuO_3$ and $Sr_4Ru_3O_{10}$ in a nominally-$Sr_3Ru_2O_7$ crystal; the same analysis has been used for *all* cation-doped $Sr_3Ru_2O_7$ crystals referred to in this thesis. Shown in Figure 3.2 is the field-cooled magnetisation of a nominally-$Sr_3Ru_2O_7$ crystal, obtained with an external field of 0.01 T applied parallel to the crystalline *c*-axis. The Curie temperature of the $SrRuO_3$ and $Sr_4Ru_3O_{10}$ intergrowths is $T = 165$ and 100 K, respectively; the magnetic contribution from the $Sr_3Ru_2O_7$ phase at low temperatures is also clear. Throughout this thesis it is assumed that any intergrowth phases are laminar, with their *c*-axis parallel to the *c*-axis of the majority bilayer phase of the crystal. The molar fractions of $SrRuO_3$ and $Sr_4Ru_3O_{10}$ have been deduced from the following procedure:

1. At $T = 200$ K apply an external magnetic field of 0.01 T to the sample. Cool down to $T = 5$ K and then measure the magnetisation on warming between 5 and 200 K.
2. Extrapolate to $T = 0$ the field-cooled $M(T)$ curve between 160 and 105 K; M_1 is the extrapolated value of M at $T = 0$ and corresponds to the magnetisation arising from $SrRuO_3$ intergrowths.
3. Extrapolate to $T = 0$ the same $M(T)$ curve between 100 and 50 K; M_2 is the value of this extrapolated curve at $T = 0$. The magnetisation associated with $Sr_4Ru_3O_{10}$ intergrowths is, therefore, $M_3 = M_2 - M_1$.

M_1 and M_3 have been compared to the published magnetisation of $SrRuO_3$ and $Sr_4Ru_3O_{10}$. Cao *et al.* [15] report the field cooled $M(T)$ of single crystals of $Sr_4Ru_3O_{10}$ with an applied field of 0.01 T: the magnetisation at $T = 1.7$ K is 0.115 μ_B/Ru. The field-cooled $M(T)$ of $SrRuO_3$ has been reported [16], also with an applied field of 0.01 T; the magnetisation at $T = 2$ K is 0.175 μ_B/Ru. It is assumed that the molar fraction of $SrRuO_3$ and $Sr_4Ru_3O_{10}$ in each crystal is $M_1/0.175$ and $M_3/0.115$, respectively, with the M values in units of μ_B/Ru. For the $Sr_3Ru_2O_7$ data in Figure 3.2 $M_1 = (2.25 \pm 0.25) \times 10^{-4}$ μ_B/Ru and $M_3 = (0.95 \pm 0.39) \times 10^{-4}$ μ_B/Ru. It can therefore be concluded that the

molar percentage of $SrRuO_3$ and $Sr_4Ru_3O_{10}$ intergrowths in this crystal is 0.13 ± 0.01 % and 0.08 ± 0.03 %, respectively.
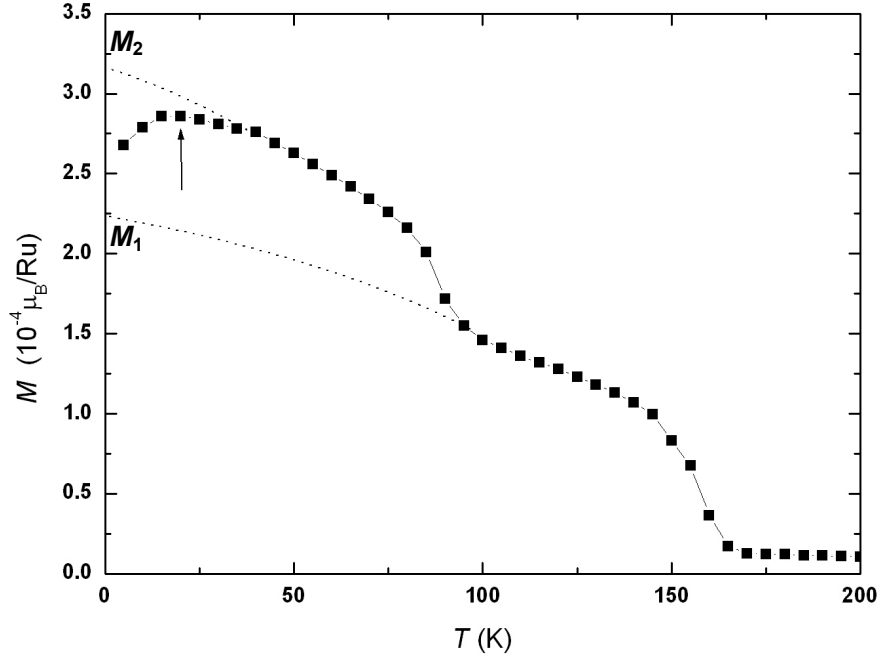
Figure 3.2. The field-cooled magnetisation of a nominally-$Sr_3Ru_2O_7$ crystal. The applied magnetic field is 0.01 T parallel to the crystalline c-axis. The dotted lines are the extrapolations to $T = 0$ referred to in the text. The arrow points to the peak in $M(T)$ associated with the $Sr_3Ru_2O_7$ phase. In this example $M_1 = (2.25 \pm 0.25) \times 10^{-4}$ μ_B/Ru and $M_2 = (3.2 \pm 0.3) \times 10^{-4}$ μ_B/Ru.

There are uncertainties associated with this method of estimating the $SrRuO_3$ and $Sr_4Ru_3O_{10}$ molar fractions. Refs. 15 and 16 refer to the bulk magnetisation of $Sr_4Ru_3O_{10}$ and $SrRuO_3$ but it is not certain that these bulk magnetisation data are applicable to intergrowth regions because interface effects with the majority $Sr_3Ru_2O_7$ phase may be important. It is also unclear if cation doping of the majority $Sr_3Ru_2O_7$ phase extends into these intergrowth phases or if these phases remain undoped. A very limited amount of magnetisation data relating to Cr-, La- and Ti-doped $SrRuO_3$ and $Sr_4Ru_3O_{10}$ has been published [17-20] and, furthermore, the cation doping levels are typically much greater than the largest doping levels considered in this thesis, namely $x \leq 0.1$ for $Sr_3(Ru_{1-x}Ti_x)_2O_7$, $x \leq 0.02$ for $Sr_3(Ru_{1-x}Cr_x)_2O_7$ and $y \leq 0.02$ for $(Sr_{1-y}La_y)_3Ru_2O_7$. It is therefore reasonable to compare the measured 'impurity'

magnetisation of the cation-doped crystals to the magnetisation of *undoped* $SrRuO_3$ and $Sr_4Ru_3O_{10}$.

Listed in Table 3.2 is the molar percentage of $SrRuO_3$ and $Sr_4Ru_3O_{10}$ in each batch of $Sr_3(Ru_{1-x}Ti_x)_2O_7$. The intergrowth percentages in these Ti-doped crystals is, as expected, much greater than in the undoped $Sr_3Ru_2O_7$ crystal indicated in Figure 3.2. Molar percentages of $SrRuO_3$ and $Sr_4Ru_3O_{10}$ of a similar order of magnitude have been measured in crystals of $(Sr_{1-y}La_y)_3Ru_2O_7$ (Chapter 5). By contrast, *much* smaller intergrowth fractions are evident in crystals of $Sr_3(Ru_{1-x}Cr_x)_2O_7$ (Chapter 4).

Crystal Batch	Molar Percentage of $Sr_4Ru_3O_{10}$	Molar Percentage of $SrRuO_3$
Ti23, $x = 0.005$	5.2	0.5
Ti15, $x = 0.01$	3.4	0.8
Ti8, $x = 0.025$	4.1	2.3
Ti21, $x = 0.05$	6.0	3.7
Ti9, $x = 0.075$	6.3	2.9
Ti7, $x = 0.1$	7.1	1.2

Table 3.2. The molar percentage of $Sr_4Ru_3O_{10}$ and $SrRuO_3$ in each batch of $Sr_3(Ru_{1-x}Ti_x)_2O_7$.

It is clear that any magnetisation data from crystals of $Sr_3(Ru_{1-x}Ti_x)_2O_7$ must be treated with caution: although $SrRuO_3$ and $Sr_4Ru_3O_{10}$ are present in these crystals with molar fractions below 10 % the contribution to the magnetisation made by these intergrowth phases is significant. The intrinsic contribution to $M(B)$ or $\chi(T)$ from the majority $Sr_3(Ru_{1-x}Ti_x)_2O_7$ phase can, nonetheless, be estimated. $SrRuO_3$ and $Sr_4Ru_3O_{10}$ have coercive fields of approximately 0.2 T (at $T = 2$ K) so that, in a measurement of $M(B)$, any contribution from the $Sr_3(Ru_{1-x}Ti_x)_2O_7$ phase at fields below this will be masked by the magnetic hysteresis loop of each of these phases. The magnetisation of $SrRuO_3$ or $Sr_4Ru_3O_{10}$ does not saturate at higher fields; dM/dB of these materials at high fields can be estimated from published data. Therefore, measurements of $M(B)$ of most of the $Sr_3(Ru_{1-x}Ti_x)_2O_7$ samples are reported *relative* to an arbitrary field value which is greater than the coercive field of either of the

intergrowth phases. The arbitrary field chosen is 1 Tesla and the change in magnetisation is defined as

$$\Delta M \equiv M(B) - M(B = 1 \text{ T}). \qquad (3.1)$$

The Pauli susceptibility of a paramagnetic metal is dM/dB and can therefore be estimated from a plot of $\Delta M(B)$ at a low temperature ($T = 2$ K is considered in this thesis).

Regarding $\chi(T)$, the magnetisation of the $Sr_3(Ru_{1-x}Ti_x)_2O_7$ phase can be enhanced (relative to the magnetisation of the intergrowth phases) by applying a larger magnetic field. However, it remains desirable to measure $\chi(T)$ of the 'low-field' magnetic regime, away from the metamagnetic features. The applied magnetic field must therefore be much smaller than B_M; the field chosen here for $Sr_3(Ru_{1-x}Ti_x)_2O_7$ is 1.5 T. Because the intrinsic component of $\chi(T)$ of the Ti-doped samples cannot be deduced easily from Figure 3.1, the susceptibility is also defined relative to a fixed value, namely $\chi(T = 2$ K):

$$\Delta\chi \equiv \chi(T) - \chi(T = 2 \text{ K}). \qquad (3.2)$$

$\Delta\chi$ and ΔM are reported for crystals of $Sr_3(Ru_{1-x}Ti_x)_2O_7$ in this chapter and for $(Sr_{1-y}La_y)_3Ru_2O_7$ in Chapter 5. *Uncorrected $M(B)$* and $\chi(T)$ are reported for $Sr_3(Ru_{1-x}Cr_x)_2O_7$ in Chapter 4 because these Cr-doped crystals have a much smaller percentage of ferromagnetic intergrowths.

3.3.2 Low-Doping ($x \leq 0.05$)

3.3.2.1 $B \parallel ab$

The samples of $Sr_3(Ru_{1-x}Ti_x)_2O_7$ have been classified as those with 'low-doping' ($x \leq 0.05$) and 'heavy-doping' ($x \geq 0.075$); the magnetisation of these two classes is reported separately. Shown in Figure 3.3 is $\Delta\chi(T)$ of $x = 0$, 0.01, 0,025 and 0.05, with $B \parallel ab$. A peak in $\Delta\chi(T)$ of $x = 0$, 0.01 and 0.025 is seen at $T = 16$, 13 and 8 K,

respectively. $\Delta\chi(T)$ of $x = 0.05$ is not peaked at any temperature above 2 K. The magnetisation of these samples is shown as a function of magnetic field in the inset to Figure 3.3. ΔM is proportional to B at low fields, with a constant of proportionality of 0.025, 0.033, 0.035 and 0.038 (μ_B/Ru)T^{-1} for $x = 0$, 0.01, 0.025 and 0.05, respectively. A sharp rise in the magnetisation of $Sr_3Ru_2O_7$ is seen in the field range between 4 and 5 Tesla, with a metamagnetic field of 4.4 ± 0.1 T. A super-linear rise in $\Delta M(B)$ of $x = 0.01$ and 0.025 is observed across approximately the same field range as the metamagnetic rise of $Sr_3Ru_2O_7$. These rises in ΔM are much less distinctive than the metamagnetism of $Sr_3Ru_2O_7$. No super-linear rise in ΔM of $x = 0.05$ is seen in the field range up to 5 Tesla.
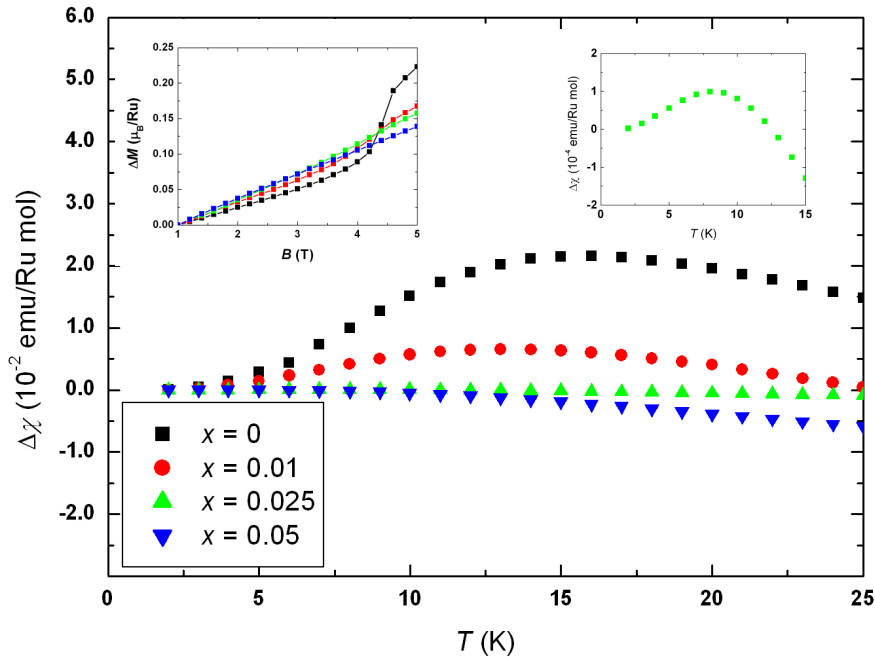
Figure 3.3. $\Delta\chi(T)$ of $x = 0$, 0.01, 0.025 and 0.05. The peak in $\Delta\chi$ of $x = 0.025$ is not clear in the main plot and is, therefore, shown in the top-right inset. The top-left inset displays $\Delta M(B)$ of each sample between 1 and 5 Tesla, measured at $T = 2$ K.

3.3.2.2 $B \parallel c$

Displayed in Figure 3.4 for $B \parallel c$ is $\Delta\chi(T)$ of $Sr_3Ru_2O_7$ and the three Ti-doped materials. $\Delta\chi$ of $Sr_3Ru_2O_7$ peaks at $T = 17$ K; a peak in $\Delta\chi$ of $x = 0.01$ and 0.025 is evident at $T = 10$ and 8 K, respectively. $\Delta\chi(T)$ of $x = 0.05$ is not peaked. It is therefore

clear that, for $B \parallel ab$ and for $B \parallel c$, a trend exists between x and T_{max}, the temperature at which $\Delta\chi$ peaks. For both field orientations T_{max} decreases as a function of x up to $x = 0.025$; $\Delta\chi(T)$ of $x = 0.05$ is not peaked.
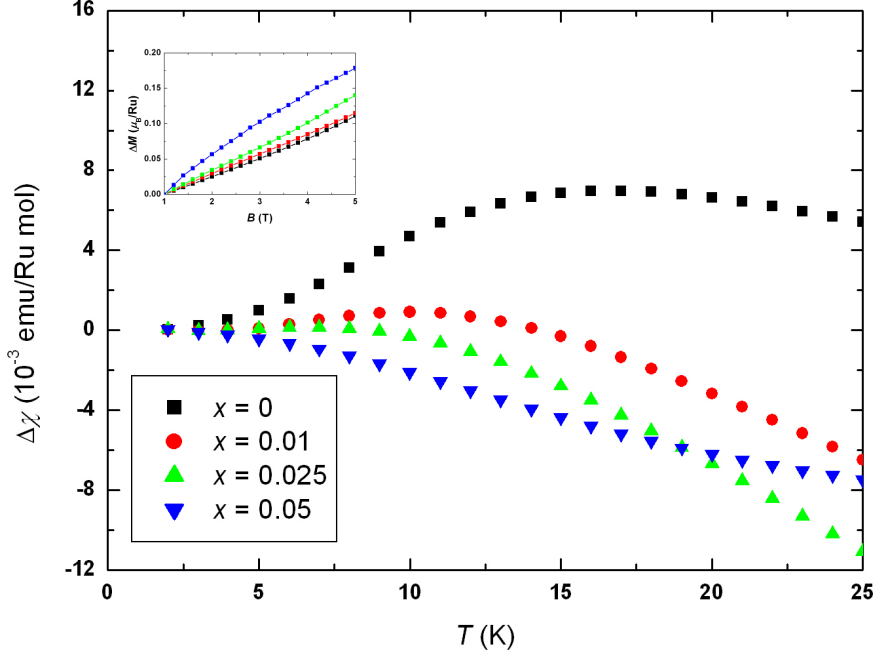
Figure 3.4. $\Delta\chi(T)$ of $x = 0$, 0.01, 0.025, 0.05. Shown in the inset is each $\Delta M(B)$ measured at $T = 2$ K.

The inset to Figure 3.4 displays $\Delta M(B)$ of the four materials. The low-field slope of $\Delta M(B)$ of $x = 0$, 0.01 and 0.025 is 0.025, 0.031 and 0.034 $(\mu_B/Ru)T^{-1}$, respectively. For $Sr_3Ru_2O_7$ this slope is identical to the slope of $\Delta M(B \parallel ab)$. The susceptibilities of $x = 0.01$ and 0.025 extracted from $\Delta M(B)$ are lower than the equivalent ab-plane values by 6 % and 3%, respectively. Overall, the change in field direction considered here does not cause a large change in $d\Delta M/dB$ of each of these materials. These observations imply that the low-T susceptibility of each material is likely to be isotropic and, hence, Pauli-like.

3.3.2.3 The Influence of Intergrowths on $\Delta\chi(T)$

Figures 3.3 and 3.4 show that the characteristic peak in $\chi(T)$ of $Sr_3Ru_2O_7$ is shifted to lower temperatures as a function of Ti-doping. For $B \parallel ab$ these observations are in

qualitative agreement with the measurements of Hooper and co-workers [11]. By contrast, for $B \parallel c$ Hooper *et al.* observe that the characteristic peak in $\chi(T)$ is suppressed by a *very* small Ti content – when $x = 0.03$, they observe no peak in $\chi(T)$. The authors of ref. 11 suggest that the peak in $\chi(T)$ is suppressed because the electronic ground sate of their Ti-doped samples is dominated by ferromagnetic fluctuations. The discrepancy between the data in ref. 11 and that reported in the main part of Figure 3.4 may arise from a number of possible sources. Hooper and colleagues measured $\chi(T)$ of their samples with an applied magnetic field of 0.3 Tesla; a 1.5 Tesla field has been used for the work described in this thesis. However, the peak in $\chi(T)$ is expected to be depressed towards *lower* temperatures if the external magnetic field is increased and, therefore, the susceptibility peaks in Figure 3.4 cannot be attributed to the relatively large magnetic field used in the study described here.

Another possible source of disagreement with the data of Hooper *et al.* is the significant content of ruthenate intergrowths in the crystals referred to in this chapter; the authors of ref. 11 claim that their crystals contain no intergrowths. Two quantities that can be extracted from the plots of $\Delta\chi(T)$ in Figures 3.3 and 3.4 are T_{max} and $\Delta\chi(T_{max})$. The magnetisation of the (Ti-doped) $SrRuO_3$ and $Sr_4Ru_3O_{10}$ phases is known to decrease monotonically as a function of increasing temperature: any peak in $\Delta\chi(T)$ cannot, therefore, be attributed to either of these intergrowth phases. Furthermore, regarding the presence of *monolayer* intergrowths, namely $Sr_2(Ru_{1-x}Ti_x)O_4$, Minakata and Maeno [1] show that the transition temperature of the density wave magnetic ordering in this series *increases* as a function of increasing x: this observation cannot be reconciled with the *decrease* in T_{max} as a function of x in Figures 3.3 and 3.4. Therefore, by a process of elimination, it is certain that peaks in $\Delta\chi(T)$ at $T = T_{max}$ in Figures 3.3 and 3.4 are intrinsic, rather than intergrowth-related. Overall, it is unlikely that the discrepancy between the susceptibility measurements in ref. 11 and those described here can be attributed to ruthenate intergrowth phases.

The electrical resistivity of the $Sr_3(Ru_{1-x}Ti_x)_2O_7$ crystals grown during the execution of this work is reported in section 3.5; $\rho_{ab}(T)$ (in zero field) of each of the Ti-doped materials is reported for temperatures between 0.1 and 300 K and, in addition, the

residual in-plane resistivity, ρ_{ab0}, of each material in units of $\mu\Omega$cm is made clear. Hooper and colleagues also report $\rho_{ab}(T)$ of their crystals at temperatures below 10 K but report the residual resistivity of only *one* of their seven Ti-doped materials: ρ_{ab0} of their $x = 0.03$ material is reported to be approximately 60 $\mu\Omega$cm. The material with the most similar titanium concentration in this chapter is $x = 0.025$, which has a residual resistivity of 25 ± 2 $\mu\Omega$cm. Therefore, the $x = 0.03$ material in ref. 11 seems to be *much* more disordered than the $x = 0.025$ material reported here, with a residual resistivity approximately double the expected value (on the basis of the work in section 3.5). There is a possibility that the disappearance of peaks in $\chi(T)$ in ref. 11 may be due to significant crystalline disorder. However, because Hooper *et al.* report only one value of ρ_{ab0}, a clear link between the disorder of their samples and the suppression of the susceptibility peak cannot be proved.

Figure 3.5 $\Delta\chi(T_{max})$ as a function of the total molar percentage of SrRuO₃ and Sr₄Ru₃O₁₀ intergrowths.

It also seems likely that the absolute value of T_{max} in Figures 3.3 and 3.4 is not influenced by the presence of intergrowths, simply because a (measured) peaked $\chi(T)$ can be the sum of a (intrinsic) peaked $\chi(T)$ and a second (intergrowth) $\chi(T)$ which

decreases smoothly with temperature. Regarding absolute values of $\Delta\chi(T)$, it may be expected that the ferromagnetic intergrowths would 'drag down' in value the intrinsic magnetisation as a function of increasing temperature (if it is assumed that the intrinsic and intergrowth magnetisations can be added together in series). Therefore, a relatively large fraction of ferromagnetic intergrowths may be expected to yield a relatively small value of $\Delta\chi(T_{max})$. Shown in Figure 3.5 is, for $x = 0$, 0.01 and 0.02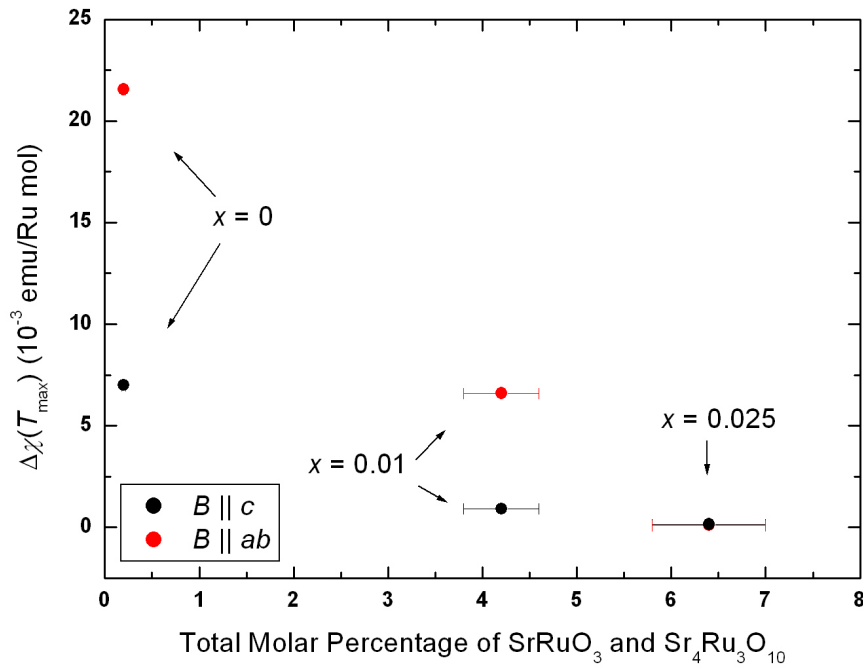5, $\Delta\chi(T_{max})$ as a function of the total molar percentage of $SrRuO_3$ and $Sr_4Ru_3O_{10}$ intergrowths. For $B \parallel ab$ and $B \parallel c$, $\Delta\chi(T_{max})$ decreases as a function of increasing intergrowth percentage. This trend *could* indicate that the ferromagnetic intergrowths do indeed 'drag down' in value the intrinsic magnetic susceptibility. On the other hand, it is also clear from Table 3.2 that $x = 0$ contains a smaller intergrowth percentage than $x = 0.01$ which, furthermore, contains a smaller intergrowth percentage than $x = 0.025$. In other words, it is impossible to de-convolute the intrinsic- and intergrowth-related effects on the absolute value of $\Delta\chi(T_{max})$.

3.3.2.4 Connection to a Spin Fluctuation Theory of Metamagnetism

Hooper *et al.* discuss some of their observations in terms of spin fluctuations. In particular they refer to the observation by Capogna *et al.* [21] that ferromagnetic fluctuations found in $Sr_3Ru_2O_7$ at high temperatures cross-over to incommensurate fluctuations at a temperature similar to T_{max}. The depression to lower temperatures of T_{max} as a function of x in ref. 11 is given as an indicator that antiferromagnetic fluctuations are suppressed by Ti-doping. Yamada [22] shows that a 1st order metamagnetic phase transition may occur in an itinerant system if $ac/b^2 < 9/20$. It can be shown that this ratio is related to the macroscopic susceptibility by the following expression:

$$\frac{ac}{b^2} = \frac{5}{28}\left[1 - \frac{\chi_P}{\chi(T_{max})}\right]^{-1},$$ (3.3)

where a, b and c are the first three coefficients of the Landau expansion referred to in section 1.2.3.2. The Pauli susceptibility, χ_P, of these samples can be deduced from the $\Delta M(B)$ data in the insets to Figures 3.3 and 3.4. It is assumed here that each $\Delta M(B)$

also includes $M(B)$ contributions from the $SrRuO_3$ and $Sr_4Ru_3O_{10}$ intergrowths. Although these are ferromagnetic materials their magnetisation does not saturate at fields up to 5 T. The slope of $M(B)$ of $SrRuO_3$ and $Sr_4Ru_3O_{10}$ at fields above 1 T, at T = 2 K, is estimated to be 0.075 and 0.013 $(\mu_B/Ru)T^{-1}$, respectively [15,16]. Therefore, the *intrinsic* Pauli susceptibility of the Ti-doped samples described here is assumed to be:

$$\chi_P = \frac{d(\Delta M)}{dB} - 0.013F_{43\_10} - 0.075F_{113}, \tag{3.4}$$

where F_{43_10} and F_{113} are the molar fractions of $Sr_4Ru_3O_{10}$ and $SrRuO_3$ in each crystal; susceptibilities are in units of $(\mu_B/Ru)T^{-1}$. $\chi(T_{max})$ can be extracted from Figures 3.3 and 3.4: if it is assumed that $\Delta\chi(T)$ at low temperatures is dominated by the intrinsic contribution then $\chi(T_{max}) = \chi_P + \Delta\chi(T_{max})$. Table 3.3 lists, for $x = 0$, 0.01 and 0.025, ac/b^2 for both field orientations. The Pauli susceptibility of each material has been deduced from Equation 3.4, with $d(\Delta M)/dB$ taken from the insets to Figures 3.3 and 3.4; F_{43_10} and F_{113} (expressed as percentages) are listed in Table 3.2. It has been assumed that $\chi(T_{max})$ is the sum of χ_P (the *estimated* Pauli susceptibility) and the uncorrected $\Delta\chi(T_{max})$, displayed in the main part of Figures 3.3 and 3.4.

x	Field	Uncorrected $d(\Delta M)/dB$ $(10^{-2}\,\mu_B/Ru)T^{-1}$	Estimated χ_P $(10^{-2}$ emu/Ru mol)	Uncorrected $\Delta\chi(T_{max})$ $(10^{-3}$ emu/Ru mol)	Estimated ac/b^2
0	$B \parallel ab$	2.5	1.5	21.6	0.3
0	$B \parallel c$	2.5	1.5	7.0	0.6
0.01	$B \parallel ab$	3.3	1.91	6.6	0.7
0.01	$B \parallel c$	3.1	1.72	0.9	3.6
0.025	$B \parallel ab$	3.5	2.03	0.1	36.6
0.025	$B \parallel c$	3.4	1.90	0.1	34.1

Table 3.3. The uncorrected d(ΔM)/dB, the estimated Pauli susceptibility, the uncorrected $\Delta\chi(T_{max})$ and the estimated value of ac/b^2 for $x = 0$, 0.01 and 0.025.

For $Sr_3Ru_2O_7$ the condition of $ac/b^2 < 9/20$ is not satisfied when $B \parallel c$. Table 3.3 also indicates that ac/b^2 increases as a function of Ti-doping. With $B = 0.3$ T $\parallel ab$, Hooper et al. deduced ac/b^2 values of 0.42, 0.80 and 6.13 for samples with $x = 0$, 0.005 and 0.03, respectively. The ac/b^2 values listed in Table 3.3 are in qualitative agreement with those in ref. 11: Ti-doping causes an increase in ac/b^2 and, in the context of the theory of Yamada, shifts the system away from a 1st order metamagnetic phase transition.

3.3.3 High-Doping ($x \geq 0.075$)

Shown in Figure 3.6 is $\Delta\chi(T)$ of $x = 0.075$ and 0.1, for $B \parallel c$. A peak in susceptibility is clear at $T_{max} = 18$ and 29 K for $x = 0.075$ and 0.1, respectively. When $T < T_{max}$ the zero-field-cooled (ZFC) susceptibility of each material falls below the field-cooled (FC) susceptibility. The differences in these ZFC and FC measurements imply that the ground state of these materials may be magnetically ordered, with a transition temperature of approximately 18 and 29 K for $x = 0.075$ and 0.l, respectively.
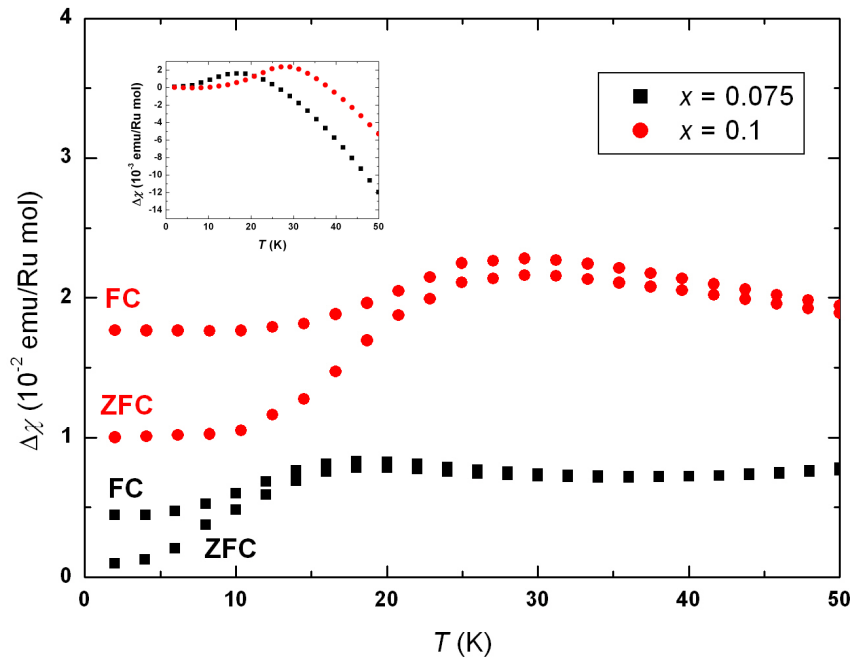

Figure 3.6. $\Delta\chi(T)$ of $x = 0.075$ and 0.1, with $B \parallel c$. The two data have, for purposes of clarity, been offset from each other. The inset displays $\Delta\chi(T)$ of each sample measured with $B \parallel ab$.

The inset to Figure 3.6 shows $\Delta\chi$ of $x = 0.075$ and 0.1 with $B \parallel ab$. $\Delta\chi$ of both samples is clearly peaked, with the same T_{max} seen as for $B \parallel c$. *No* difference was observed in the field-cooled and the zero-field-cooled susceptibilities when $B \parallel ab$: it is therefore clear that the ordered magnetic moment in these samples is aligned along (or very close to) the crystalline c-axis because, if the magnetic moment was aligned along an *intermediate* direction (i.e. some direction between ab and c), a difference in the ZFC and FC measurements in the c-axis *and* the ab-plane would be expected. Also, no time-dependence of the remanent moment of the low-temperature state ($B \parallel c$) has been detected, implying that the differences in $\Delta\chi_{FC}$ and $\Delta\chi_{ZFC}$ in Figure 3.6 are associated with static magnetism, rather than glassy irreversibility.

The magnetic ordering in these samples could, in principle, be related to intergrowth phases. However, if Figure 3.6 is considered alongside heat capacity and resistivity data in Figures 3.8 and 3.9, respectively, it is clear that the magnetic ordering is associated with the majority $Sr_3(Ru_{1-x}Ti_x)_2O_7$ phase. Moreover, neutron scattering measurements (referred to in section 3.7) have indicated that the wave-vector of the magnetic ordering in these samples has a well-defined dependence on the reciprocal lattice of the *bilayer* ruthenate phase. This is further evidence that this magnetic ordering is intrinsic, rather than intergrowth-related.

3.4 Heat Capacity

Hooper *et al.* observed an upturn in C/T of samples of $Sr_3(Ru_{1-x}Ti_x)_2O_7$ ($x \neq 0$) at low temperatures. A low-temperature upturn in C/T has also been observed in small-x samples of the $Sr_2Ru_{1-x}Ti_xO_4$ series [2]. Shown in Figure 3.7 is C/T of $Sr_3Ru_2O_7$ and each of the Ti-doped samples as a function of temperature squared; these heat capacity measurements extend down to $T = 400$ mK, much lower than the 2 K base temperature in ref. 11. At temperatures above approximately 15 K C/T of each material is proportional to T^2. The inset to Figure 3.7 displays the constant of proportionality, β, in this regime; no obvious correlation between β and x is evident.

The electronic component of the heat capacity, C_{el}, is assumed to be the difference in the total heat capacity and the phonon contribution, such that $C_{el}/T = C/T - \beta T^2$. This quantity is displayed in Figure 3.8 for all of the samples. C_{el}/T of $Sr_3Ru_2O_7$ rises from 110 mJ/Ru mol K^2 at 400 mK to a peak of $\sim$ 120 mJ/Ru mol K^2 at $T = 7.5$ K. C_{el}/T of $x = 0.005$ also peaks at $T = 7.5$ K but, in contrast to C_{el}/T of $Sr_3Ru_2O_7$, does not settle to a temperature-independent value at the lowest temperatures: C_{el}/T of this sample displays a broad minimum of 110 mJ/Ru mol K^2 at $T = 2$ K and *increases* to 115 mJ/Ru mol K^2 at $T = 400$ mK. An upturn in C_{el}/T of $x = 0.01$ is also clear: a minimum of 110 mJ/Ru mol K^2 at $T = 3$ K is accompanied by a rise to 120 mJ/Ru mol K^2 at $T = 400$ mK. C_{el}/T of $x = 0.025$ and 0.05 decrease as a function of T across the entire range of temperatures shown in Figure 3.8.
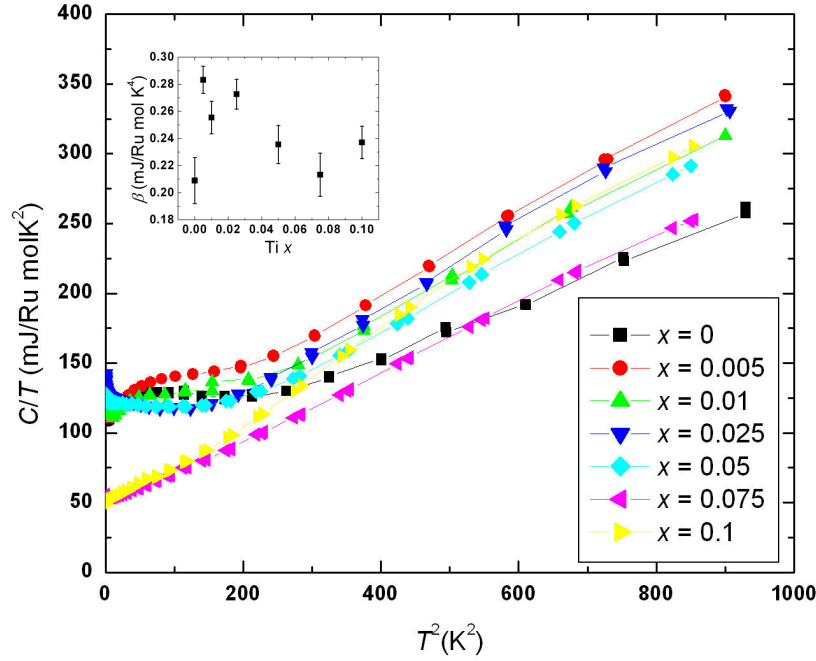
Figure 3.7. *C/T of $Sr_3(Ru_{1-x}Ti_x)_2O_7$ as a function of temperature squared. The β coefficient of each sample in shown in the inset.**

In their study of $Sr_2(Ru_{1-x}Ti_x)O_4$ Kikugawa and Maeno reported a logarithmic divergence with temperature of C_{el}/T of $x = 0.025$. This logarithmic dependence was attributed to critical magnetic fluctuations. Shown in the inset to Figure 3.8 is C_{el}/T of the $x = 0.025$ and 0.05 samples as a function of $\ln(T)$. At temperatures between 0.4 and 4.5 K C_{el}/T of both materials is proportional to $\ln(T)$ with a constant of

proportionality of 8.27 and 4.72 mJ/Ru mol K^3 for $x = 0.025$ and 0.05, respectively. These observations clearly indicate the presence of critical magnetic fluctuations in the $x = 0.025$ and 0.05 materials.

The electronic component of C/T of $x = 0.075$ and 0.1 is *significantly* smaller than C_{el}/T of the other samples; the temperature dependence of C_{el}/T of these two samples is also relatively weak. Measurements in section 3.3.3 suggested that the ground state of these materials may be magnetically ordered; the relatively small C_{el}/T of these materials is likely to be concomitant with any magnetic ordering. A smaller C_{el}/T implies that parts of the original $Sr_3Ru_2O_7$ Fermi surface have been gapped and, therefore, the data in Figure 3.8 hint at the presence of a spin density wave (SDW) in the $x = 0.075$ and 0.1 materials.
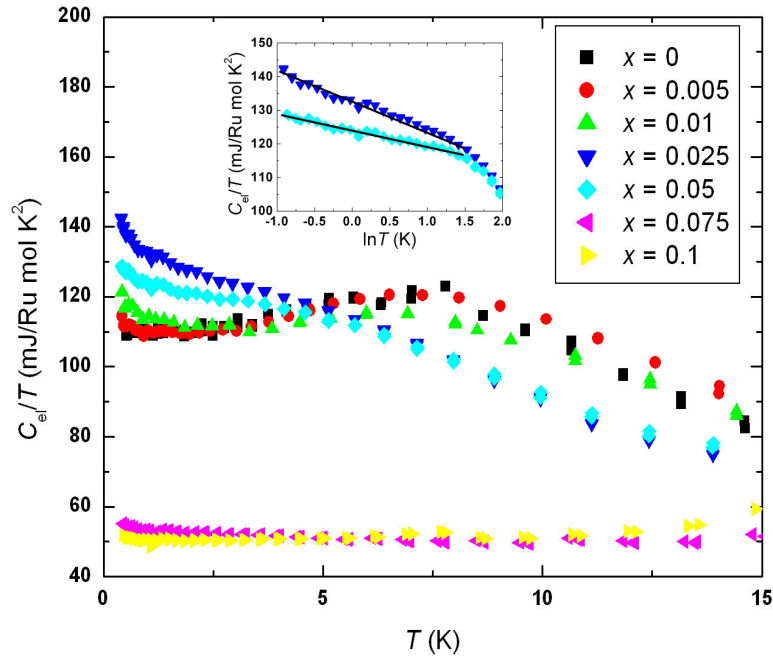
Figure 3.8. C_{el}/T of $Sr_3(Ru_{1-x}Ti_x)_2O_7$ as a function of temperature. The inset shows C_{el}/T of $x = 0.025$ and 0.05 at low temperatures on a $\ln(T)$ scale.

$SrRuO_3$ and $Sr_4Ru_3O_{10}$ both have a Sommerfeld coefficient of approximately 30 mJ/Ru mol K^2 [23, 24]: a suppression of C_{el}/T of the $x = 0.075$ and 0.1 samples may, in principle, arise from ferromagnetic intergrowth phases within these materials. For instance, 6.3 and 2.9 molar percent of $Sr_4Ru_3O_{10}$ and $SrRuO_3$ intergrowths,

respectively, have been estimated in samples of $x = 0.1$ (Table 3.2). If it is assumed that the heat capacity of these intergrowths can be added in series to the heat capacity of the majority phase, an approximation to C_{el}/T of $x = 0.1$ is ((91.8% × 110 mJ/Ru mol K^2) + (9.2% × 30 mJ/Ru mol K^2)) = 102 mJ/Ru mol K^2. This value is only slightly smaller than C_{el}/T of *undoped* Sr$_3$Ru$_2$O$_7$ at low temperatures. If this assumption of adding the heat capacities in series is maintained it is obvious that, with $O(10\%)$ total molar content of intergrowths, the relatively small values of C_{el}/T of the $x = 0.075$ and 0.1 samples cannot be accounted for by the intergrowth phases, even if C_{el}/T of these was zero. It is therefore certain that a relatively small electronic heat capacity is an intrinsic feature of these samples.

The logarithmic divergence of C_{el}/T of $x = 0.025$ and 0.05 is qualitatively similar to the divergence of C_{el}/T of Sr$_2$Ru$_{1-x}$Ti$_x$O$_4$ ($x = 0.025$) measured by Kikugawa and Maeno. C_{el}/T of Sr$_2$RuO$_4$ at $T = 400$ mK is enhanced by 8 mJ/Ru mol K^2 by $x = 0.025$ Ti-doping [2]. For the same x value an enhancement of more than 30 mJ/Ru mol K^2 can be seen in Figure 3.8. It is therefore clear that the logarithmic divergence of C_{el}/T of some of the samples of Sr$_3$(Ru$_{1-x}$Ti$_x$)$_2$O$_7$ cannot be attributed to Sr$_2$Ru$_{1-x}$Ti$_x$O$_4$ intergrowths and is, therefore, intrinsic to these materials.

An SDW in Sr$_2$Ru$_{1-x}$Ti$_x$O$_4$ ($x = 0.09$) has been detected in neutron scattering experiments [3] at temperatures below approximately 25 K. C_{el}/T of this material extrapolated to $T = 0$ K is 35 mJ/Ru mol K^2; this value is slightly smaller than the Sommerfeld coefficient of Sr$_2$RuO$_4$, 40 mJ/Ru mol K^2. Therefore, the suppression of C_{el}/T of $x = 0.075$ and 0.1 (relative to C_{el}/T of $x = 0$) displayed in Figure 3.8 is *much* larger than the suppression of C_{el}/T due to heavy Ti-doping into Sr$_2$RuO$_4$.

3.5 Resistivity as a Function of Temperature

Shown in Figure 3.9 is the in-plane electrical resistivity of Sr$_3$(Ru$_{1-x}$Ti$_x$)$_2$O$_7$ as a function of temperature. Measurements between 4 K and 300 K were made in a continuous flow cryostat; temperatures below 4 K were achieved with an ADR. ρ_{ab} of each sample varies linearly with T at high temperatures; the constant of proportionality is 0.77, 0.78, 0.74, 0.77, 0.76, 0.77 and 0.76 μΩcmK^{-1} for $x = 0$, 0.01,

0.025, 0.05, 0.075 and 0.1, respectively. A minimum in $\rho_{ab}(T)$ of $x = 0.075$ and 0.1 is evident at $T = 19$ K and 35 K, respectively. These temperatures are quite similar to the T_{max} values of 18 and 29 K pertinent to the DC magnetisation of these samples (section 3.3.3). An inset to Figure 3.9 displays the resistivity of $x = 0.05$ at low temperatures; a minimum in $\rho_{ab}(T)$ is seen at $T = 1.5$ K. For those samples with $x < 0.05$, $d\rho_{ab}/dT$ is positive across the entire range of temperatures. The second inset to Figure 3.8 shows $(\rho_{ab} - \rho_{ab0})/T^2$ ($\equiv A$) of $x = 0$, 0.01 and 0.025. Although the noise associated with each measurement dominates at the lowest temperatures it seems likely that $(\rho_{ab} - \rho_{ab0})/T^2$ of each sample remains constant as $T \to 0$. A increases from 0.08 $\mu\Omega$cmK^{-2} for Sr$_3$Ru$_2$O$_7$ to 0.091 and 0.099 $\mu\Omega$cmK^{-2} for $x = 0.01$ and 0.025, respectively. T_{FL}, the maximum temperature to which the T^2 resistivity extends, is depressed from 8.3 K for Sr$_3$Ru$_2$O$_7$ to 6.5 and 6.0 K for $x = 0.01$ and 0.025, respectively.
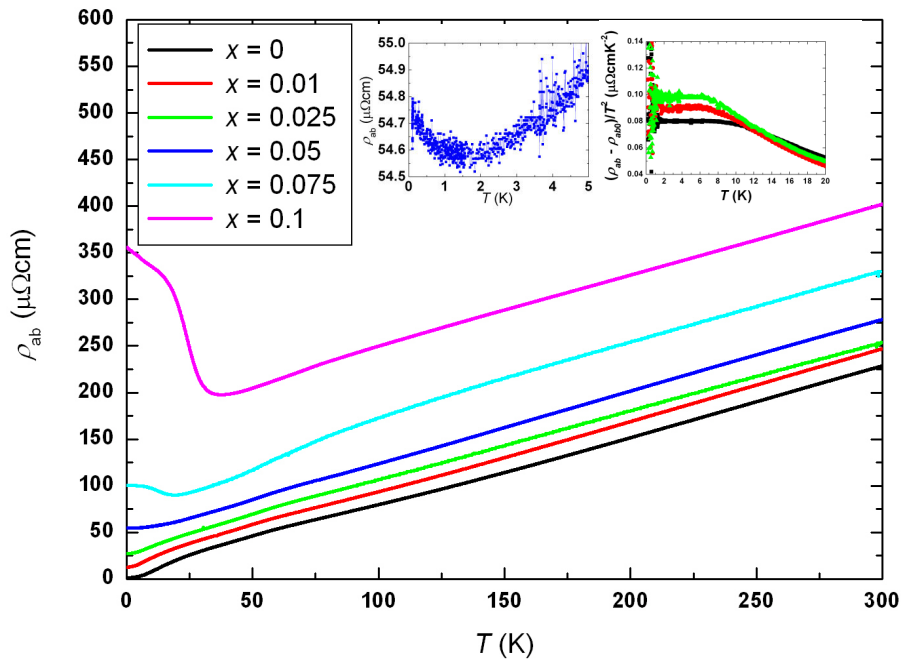
Figure 3.9. $\rho_{ab}(T)$ of Sr$_3$(Ru$_{1-x}$Ti$_x$)$_2$O$_7$. The left-hand inset shows $\rho_{ab}(T)$ of $x = 0.05$ at low temperatures; the right-hand inset displays $(\rho_{ab} - \rho_{ab0})/T^2$ of $x = 0$, 0.01 and 0.025 at temperatures below 20 K.

It is highly probable that the upturn in $\rho_{ab}(T)$ of $x = 0.075$ and 0.1 is associated with the magnetic ordering postulated in section 3.3.3. A large resistivity at low

temperature is consistent with the suggestion that some parts of the Fermi surface, and hence some of the free carriers, of $Sr_3Ru_2O_7$ have vanished. An upturn in $\rho_{ab}(T)$ of $Sr_2Ru_{0.91}Ti_{0.09}O_4$ [1] has also been observed, with the resistivity minimum of this material at $T = 25$ K, a temperature almost identical to the temperature below which signatures of a SDW were seen in neutron scattering experiments. Overall, the minimum in $\rho_{ab}(T)$ of both $x = 0.075$ and 0.1 in Figure 3.8 is likely to be associated with the onset of a SDW in these materials

The minimum in $\rho_{ab}(T)$ of $x = 0.05$ occurs at $T = 1.5$ K, a temperature lower than can be attained with the cryogenic setup of the MPMS magnetometer. If 1.5 K is assumed to be approximately coincident with a magnetic ordering temperature, it is unsurprising that no signatures of magnetic ordering were observed in the magnetisation of $x = 0.05$ (section 3.3.2). However, the electronic component of the heat capacity of $x = 0.05$ is *qualitatively* different to C_{el}/T of $x = 0.075$ and 0.1. The upturn in $\rho_{ab}(T)$ is not, therefore, an unambiguous indicator of magnetic ordering of the ground state of $x = 0.05$.

3.6 Magnetoresistance

3.6.1 $x = 0, 0.01$ and 0.025

The inset to Figure 3.3 indicates that, across approximately the same region of field at which $M(B)$ of $Sr_3Ru_2O_7$ rises, $\Delta M(B)$ of $x = 0.01$ and 0.025 also rise super-linearly. It is desirable to look for signatures of this metamagnetism in the magnetoresistance of these Ti-doped samples. Shown in Figure 3.10 is the magnetoresistance (normalised with respect to the zero-field resistivity) of $x = 0, 0.01$ and 0.025 at $T = 300$ mK. The magnetic field was applied parallel to the ab-planes of each crystal and was also parallel to the electrical current. These measurements were made in an ADR with the external magnetic field swept at 0.1 T/min.

The lower-field peaks in $\rho_{ab}(B)$ of $Sr_3Ru_2O_7$ are associated with the primary and secondary metamagnetic fields at 5.0 and 5.8 T, respectively; the feature centred

about 6.2 T is sensitive to residual in-plane resistivity and has associated with it an in-plane magnetoresistive anisotropy (discussed in the appendix). *No* sharp peaks are seen in the magnetoresistance of $x = 0.01$ or 0.025 at $T = 300$ mK. The data in the main part of Figure 3.10 are in qualitative agreement with the magnetoresistance measurements of Hooper and colleagues [11], who report that a small amount of Ti-doping 'smears-out' the sharp features in $\rho_{ab}(B)$ of $Sr_3Ru_2O_7$. Furthermore, the absence of any sharp features in $\rho_{ab}(B)$ of $x = 0.01$ and 0.025 probably indicates that the 1st order metamagnetic features of $Sr_3Ru_2O_7$ have been suppressed.

The insets to Figure 3.10 show $\rho_{ab}(B)$ of $x = 0.01$ and 0.025 at $T = 300$, 600 and 1200 mK. Features in $\rho_{ab}(B)$ of $x = 0.01$ are clear at fields of 5.0 and 5.8 T but, by contrast, only *one* feature, a broad maximum, is seen in $\rho_{ab}(B)$ of $x = 0.025$. Increasing temperature from 300 to 1200 mK does not cause any major qualitative changes to $\rho_{ab}(B)$ of either of these materials.
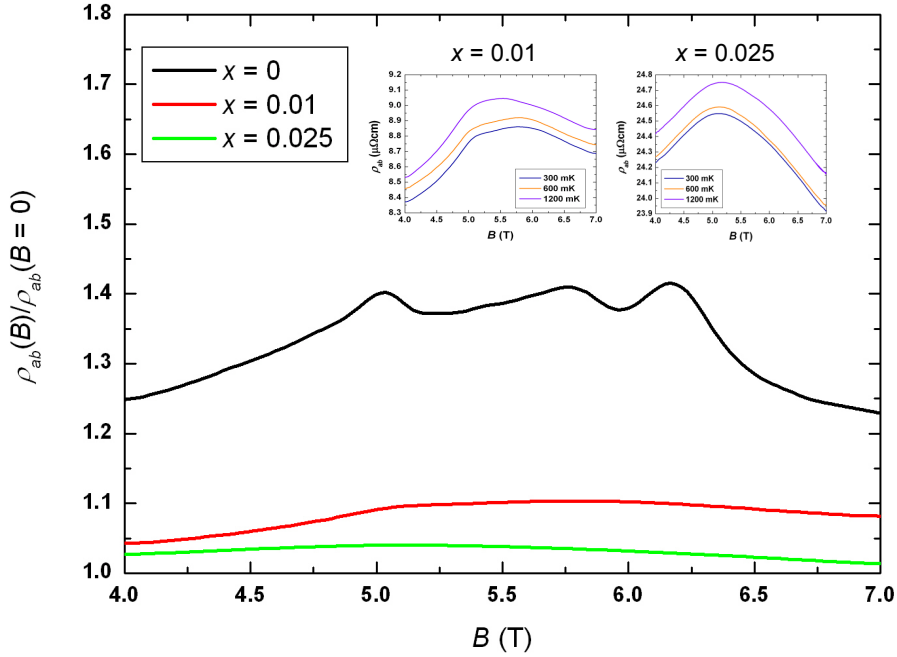

Figure 3.10. The magnetoresistance ($B \parallel I \parallel ab$) of $x = 0$, 0.01 and 0.025 at $T = 300$ mK. $\rho_{ab}(B)$ of $x = 0.01$ and 0.025 at $T = 300$, 600 and 1200 mK is displayed in the insets.

3.6.2 Thermal- and Disorder-Related Effects on $\rho_{ab}(B)$

If it is assumed that Ti^{4+} orbitals do not hybridise with the conducting Ru-O planes of $Sr_3Ru_2O_7$, the major consequence of Ti-doping may be the reduction of the electronic mean free path within these planes, due to elastic scattering. A reduction of the electronic mean free path can also be achieved by 'thermally broadening' the Fermi surface by increasing temperature.
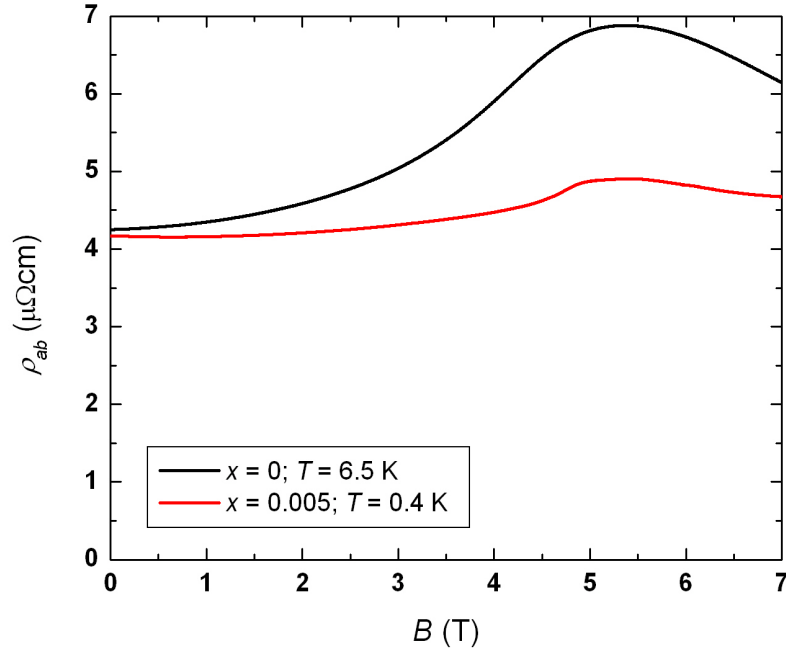
Figure 3.11. $\rho_{ab}(B)$ of $Sr_3Ru_2O_7$ at $T = 6.5$ K and $\rho_{ab}(B)$ of $x = 0.005$ at $T = 400$ mK.

It is desirable to compare the influence on $\rho_{ab}(B)$ of $Sr_3Ru_2O_7$ of thermal- and disorder-related effects. Shown in Figure 3.11 is the magnetoresistance at $T = 6.5$ K of a $Sr_3Ru_2O_7$ crystal alongside $\rho_{ab}(B)$ of $x = 0.005$ measured at $T = 400$ mK; $B \parallel I \parallel ab$ in each case. The residual resistivity of the $Sr_3Ru_2O_7$ crystal is 1.25 $\mu\Omega$cm and the A coefficient is 0.075 $\mu\Omega$cmK^{-2}: at $T = 6.5$ K the zero-field resistivity of this crystal is 4.4 ± 0.2 $\mu\Omega$cm. This resistivity is, within errors, identical to the 4.5 ± 0.2 $\mu\Omega$cm residual resistivity of the $x = 0.005$ crystal. In spite of the two crystals having very similar resistivities at zero field, the two $\rho_{ab}(B)$ are remarkably different. A peak is seen in both data at approximately 5.5 Tesla but, across the field range between zero and seven Tesla, the magnetoresistance of the $x = 0.005$ sample is always smaller than

$\rho_{ab}(B)$ of $Sr_3Ru_2O_7$. It is therefore apparent that the effects of temperature and gentle Ti-doping on the in-plane magnetoresistance of $Sr_3Ru_2O_7$ are not equivalent.

3.7 Discussion

The main observations reported in this chapter are:

- A small amount of titanium doping into $Sr_3Ru_2O_7$ enhances the electronic component of the heat capacity at low temperatures. For certain doping levels —$x = 0.025$ and 0.05— this enhancement has a $\ln(T)$ form at temperatures below approximately 4 K.

- Heavier titanium doping —$x = 0.075$ and 0.1— causes a significant decrease in the electronic heat capacity at low temperatures (Figure 3.8).

- In those samples for which $x \leq 0.05$ the characteristic peak in $\chi(T)$ is shifted to lower temperatures as a function of x (Figures 3.3 and 3.4).

- Magnetic irreversibility is observed in the $x = 0.075$ and 0.1 materials (Figure 3.6). The temperature below which this irreversibility occurs is very similar to the temperature at which an upturn in the electrical resistivity has been measured (Figure 3.9).

Much of the low-energy electronic physics of these members of the $Sr_3(Ru_{1-x}Ti_x)_2O_7$ series is captured remarkably well by Figure 3.8, in which the electronic component of the molar heat capacity is displayed. These measurements extend to lower temperatures and incorporate many more samples than the heat capacity measurements reported in ref. 11. At low temperatures C_{el}/T of $Sr_3Ru_2O_7$ is independent of temperature and the Sommerfeld coefficient is 110 mJ/Ru mol K^2. A small amount of Ti-doping induces an upturn in C_{el}/T at low temperatures. For $x = 0.025$ and 0.05 this upturn extends over a decade of temperature down to 0.4 K and diverges logarithmically with temperature. A substantial reduction in C_{el}/T of the samples with heavier Ti-doping has also been observed; the temperature dependence of these two heat capacities is also quite weak. Overall, these observations are consistent with emergence of a spin density wave as a function of Ti-doping. A small C_{el}/T indicates that sections of the original Fermi surface have been gapped; a $\ln(T)$ contribution to the heat capacity points towards critical magnetic fluctuations. It may

be possible that, at a critical value of x, these magnetic fluctuations are 'frozen' and that static magnetic ordering then emerges at higher doping levels. An upturn in $\rho_{ab}(T)$ is observed in these samples at temperatures approximately equal to T_{max}. It is notable that Hooper *et al.* also measured a low-T upturn in C/T of some of their materials but did not report any particular temperature dependence. Ref. 11 also reports an upturn in $\rho_{ab}(T)$ of an $x = 0.08$ sample, but the magnetic susceptibility or heat capacity of this sample was not reported.

Spin dynamics and magnetic ordering wave-vectors can often be explored by neutron scattering experiments. Such experiments have been performed by Professor Markus Braden and Paul Steffens of the University of Cologne, to whom crystals of $x = 0.075$ and 0.1 from this thesis were provided. These measurements are unpublished, so only minor reference is made to them here. Five of the conclusions that have emerged from these experiments are: (1) static magnetic ordering with an ordering wave-vector $\mathbf{Q} \sim$ (¼ ¼ 0) (in the (h k l) notation) is observed in these samples; (2) this magnetic ordering has a well-defined dependence of reciprocal $Sr_3Ru_2O_7$ lattice out of the RuO_2 planes; (3) the ordering is *much* weaker out-of-plane than it is in-plane; (4) the temperature below which this ordering is seen is 18 and 30 K for $x = 0.075$ and 0.01, respectively and; (5) the ordered magnetic moment is aligned along the crystalline c-axis. The second of these conclusions validates the earlier assertion that signatures of ordering in the DC susceptibility (Figure 3.6) are intrinsic, rather than intergrowth-related. The latter two conclusions are also in excellent agreement with the measurements of $\chi(T)$. The two-dimensional nature of this magnetic ordering can probably be traced back to the quasi-2D structure of $Sr_3Ru_2O_7$. Regarding the wave-vector of the magnetic ordering, a similar $\mathbf{Q}$ was observed in magnetically-ordered samples of $Sr_3(Ru_{1-x}Mn_x)_2O_7$ studied by Mathieu and colleagues. Displayed in Figure 3.12 for $x = 0.075$ and 0.1 is the elastic intensity at certain $\mathbf{Q}$ as a function of temperature. The onset of the magnetic intensity is clear in each case. Overall, the measurements reported in this chapter and these neutron scattering measurements provide unambiguous evidence for the formation of a spin density wave in $x = 0.075$ and 0.1.

A spin density wave in the $Sr_2Ru_{1-x}Ti_xO_4$ series has been accounted for in terms of spin fluctuations in *undoped* Sr_2RuO_4 [21] Magnetic fluctuations (arising from Fermi

surface nesting) with $\mathbf{Q} \sim (0.67, 0.67, 0)$ have been measured in Sr_2RuO_4. Ti-doping seems to 'freeze' these fluctuations: static magnetic ordering with $\mathbf{Q} \sim (0.67, 0.67, 0)$ has been observed in samples of $Sr_2Ru_{1-x}Ti_xO_4$ ($x = 0.09$). However, fluctuations with $\mathbf{Q} \sim (\frac{1}{4}, \frac{1}{4}, 0)$ relevant to the Mn- and Ti-doped bilayer ruthenate have *not* been observed in undoped $Sr_3Ru_2O_7$ [25]. Furthermore, glassy magnetic behaviour (i.e. a time-dependent remanent magnetisation) has been observed in small-x samples of the $Sr_2Ru_{1-x}Ti_xO_4$ series [1] but no similar behaviour has been measured for any of the of the $Sr_3(Ru_{1-x}Ti_x)_2O_7$ materials reported in this work. It is therefore unlikely that the static magnetic ordering in samples of $Sr_3(Ru_{1-x}Ti_x)_2O_7$ emerges in the same way as the ordering does in $Sr_2Ru_{1-x}Ti_xO_4$.
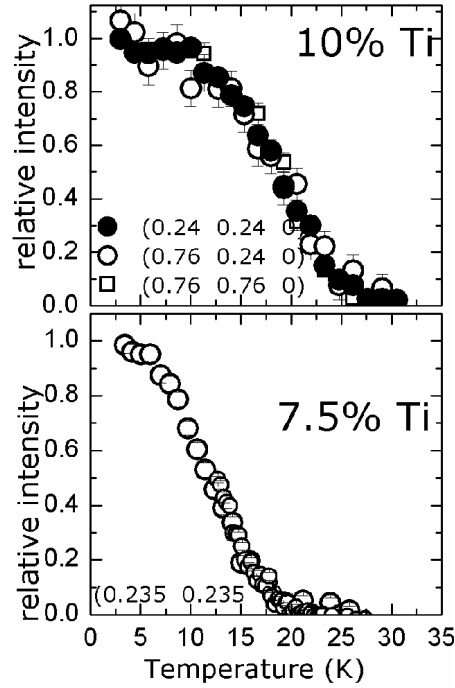
Figure 3.12. The temperature dependence of the elastic intensity measured in neutron scattering experiments on crystals of $x = 0.075$ and 0.1 grown in St Andrews. The wave-vectors at which this intensity has been measured are displayed in each panel. Images courtesy of Paul Steffens and Markus Braden.

The depression to lower temperatures of the peak in $\chi(T)$ is in qualitative agreement with the earlier work of Hooper and colleagues. In the theory of Yamada [22], a smaller T_{max} is consistent with an enhanced Pauli susceptibility. χ_P, estimated from $\Delta M(B)$, *is* enhanced as a function of x, for $x \leq 0.05$. The sharp metamagnetic features

of $Sr_3Ru_2O_7$ are also smeared out in field by a small amount of Ti-doping and ac/b^2 is enhanced. These observations imply that the first-order metamagnetic physics is suppressed by Ti-doping.

Figure 3.10 indicates that thermal effects on the in-plane magnetoresistance of $Sr_3Ru_2O_7$ are inequivalent to the effect on $\rho_{ab}(B)$ of a small amount of Ti-doping. Spin fluctuations may, in principle, be the source of the difference between the two $\rho(B)$. At relatively high temperatures, it is likely that electrical transport would be influenced by thermal population of the modes of such fluctuations. On the other hand, it is not clear how such fluctuations would be influenced at low temperatures by quenched crystalline disorder. In light of the strong magneto-elastic coupling known in Ruddlesden-Popper ruthenates, a mode of the *lattice* cannot be ruled out as a source of the difference in the two $\rho_{ab}(B)$.

(a)   (b)
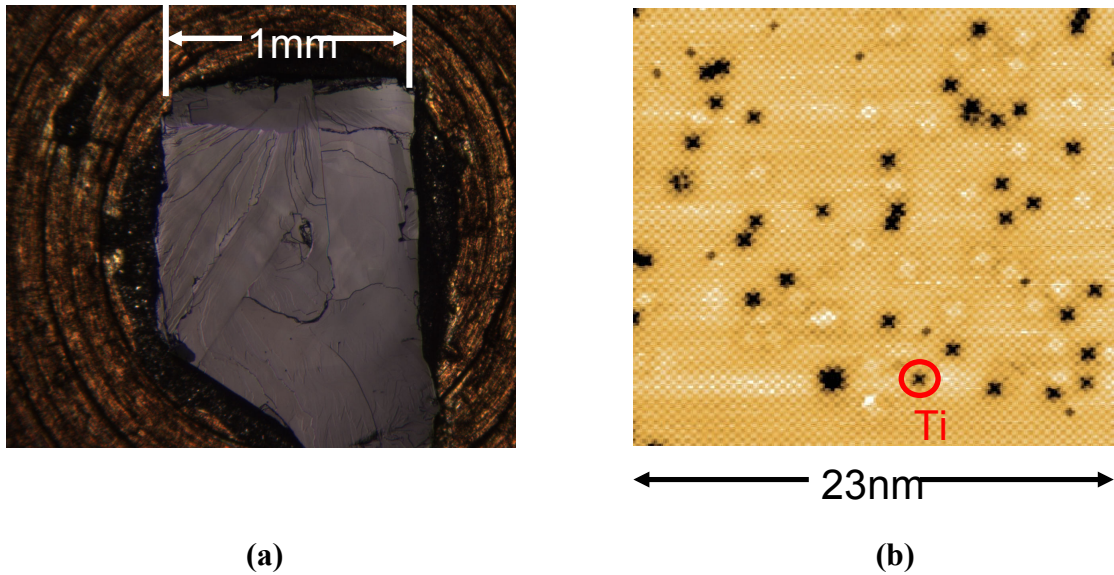
Figure 3.13. (a) A crystal of $Sr_3(Ru_{0.99}Ti_{0.01})_2O_7$, cleaved and ready for use in an STM experiment. (b) A topographic image of this crystal, with atomic resolution. Images courtesy of Dr Jinho Lee, Alfred Wang and Milan Allan.

Although the orbitals of Ti^{4+} cations probably do not hybridise with the conducting Ru-O planes, Ti-doping can, nonetheless, modify the spectrum of Landau quasiparticles of $Sr_3Ru_2O_7$. Elastic scattering from impurity atoms will mix eigenstates of the same energy but with different $\mathbf{k}$. If eigenstates with $\mathbf{k}_1$ and $\mathbf{k}_2$ are mixed an interference pattern with wave-vector $\mathbf{q} = \mathbf{k}_2 - \mathbf{k}_1$ will appear in the

quasiparticle wavefunction and, hence, modulations of the local density of states (LDOS) with wavelength $\lambda=2\pi/|\mathbf{q}|$ will occur. These quasiparticle interference (QPI) effects can, in principle, be observed by scanning tunnelling microscopy [26, 27]. Samples of $Sr_3(Ru_{1-x}Ti_x)_2O_7$ referred to in this chapter have been provided to the research group of Professor Séamus Davis at Cornell University. In work which has not yet been published Dr Jinho Lee, Alfred Wang and Milan Allan have observed QPI effects in some of the small-x samples of this series. In contrast to the very clean $Sr_3Ru_2O_7$ crystals in which disorder-sensitive features have been observed some degree of quenched crystalline disorder is *desirable* for QPI experiments, hence the suitability of the Ti-doped samples referred to in this thesis.

(a)   (b)
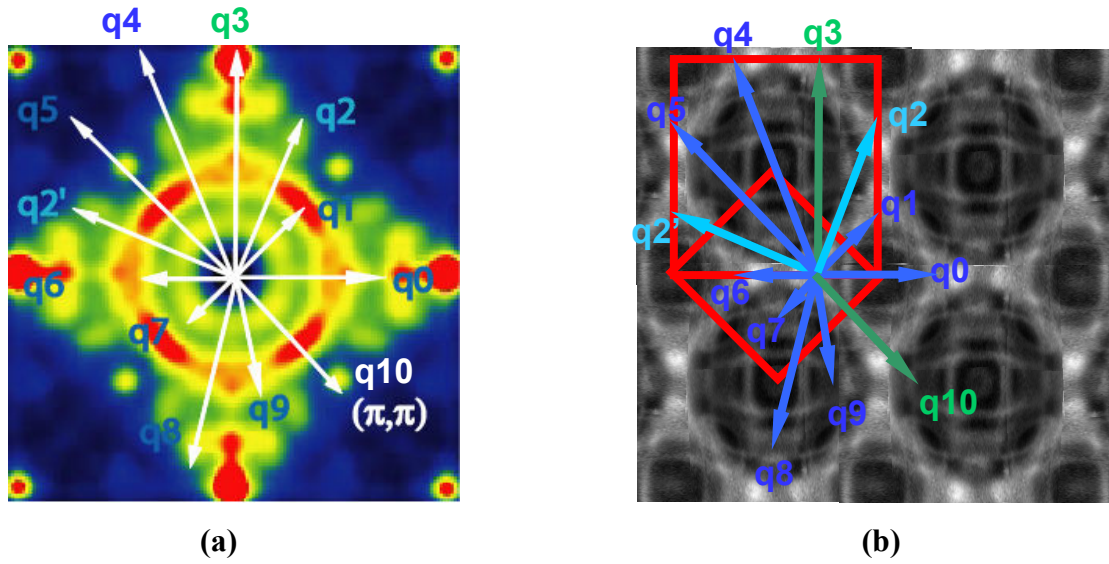
Figure 3.14. (a) The QPI pattern of a crystal of $Sr_3(Ru_{1.99}Ti_{0.01})_2O_7$ grown during the execution of the work described in this chapter. This pattern, displayed in *q*-space, was obtained by Fourier-transforming the pattern of the real-space variation in the local electronic density of states. (b) The electronic band-structure of *undoped* $Sr_3Ru_2O_7$, displayed in *k*-space. This image was obtained in an ARPES experiment by Dr Felix Baumberger; the crystal on which this measurement was made was also grown in St Andrews, by Dr Robin Perry. Images courtesy of Dr Jinho Lee, Alfred Wang and Milan Allan.

Displayed in Figure 3.13(a) is an image of a cleaved crystal of $Sr_3(Ru_{0.99}Ti_{0.01})_2O_7$; a topographic image of this crystal obtained in an STM experiment is shown in Figure 3.13(b). The titanium ions are clear in this image and, furthermore, the concentration of these ions is in good agreement with EDX measurements (section 3.2.2). A real-

space map of the variations in the LDOS of this material has been made; QPI effects have been revealed by obtaining the Fourier transform of this map. The QPI pattern from a crystal of $x = 0.01$ is compared to the Fermi surface of *undoped* $Sr_3Ru_2O_7$ in Figure 3.14. These are the first observations of QPI effects in ruthenates; no QPI signatures were observed in previous experiments on undoped $Sr_3Ru_2O_7$ or in cation-doped Sr_2RuO_4. These STM experiments may shed light on the heavily-renormalised ground state of undoped $Sr_3Ru_2O_7$ and may also reveal the origins of the spin density wave in the heavily-doped samples. Previous STM experiments on samples of $Sr_2Ru_{1-x}Ti_xO_4$ were hindered by a surface reconstruction of the electronic structure [28]; no such surface reconstruction has been observed in samples of bilayer strontium ruthenate. Overall, STM measurements on cation-doped samples grown during the execution of this work, when combined with the magnetisation, heat capacity and transport measurements already made, are likely to reveal much information about the electronic physics of $Sr_3Ru_2O_7$.

3.8 References

[1] M. Minakata and Y. Maeno, Phys. Rev. B **63**, 180504 (2001)

[2] N. Kikugawa and Y. Maeno, Phys. Rev. Lett. **89**, 117001 (2002)

[3] M. Braden, O. Friedt, Y. Sidis, P. Bourges, M. Minakata and Y. Maeno, Phys. Rev. Lett. **88**, 197002 (2002)

[4] K. W. Kim, J. S. Lee, T. W. Noh, S. R. Lee and K. Char, Phys. Rev. B **71**, 125104 (2005)

[5] J. Kim, J.-Y. Kim, B.-G. Park and S.-J. Oh, Phys. Rev. B **73**, 235109 (2006)

[6] N. Kikugawa and A. P. Mackenzie, unpublished

[7] T. He and R. J. Cava, Phys. Rev. B **63**, 172403 (2001)

[8] http://abulafia.mt.ic.ac.uk/shannon/ptable.php

[9] S. V. Halilov, D. J. Singh, J. Minár, A. Y. Perlov and H. Ebert, Phys. Rev. B **71**, 100503 (2005)

[10] K. Maiti, R. S. Singh and V. R. Medicherla, Phys. Rev. B **76**, 165128 (2007)

[11] J. Hooper, M. H. Fang, M. Zhou, D. Fobes, N. Dang, Z. Q. Mao, C. M. Feng, Z. A. Xu, M. H. Yu, C. J. O'Connor, G. J. Xu, N. Andersen and M. Salamon, Phys. Rev. B **75**, 060403 (2007)

[12] P. Steffens and M. Braden, unpublished

[13] T. Hanaguri, Y. Kohsaka, J. C. Davis, C. Lupien, I. Yamada, M. Azuma, M. Takano, K. Ohishi, M. Ono and H. Takagi, Nature Phys. **3**, 865 (2007)

[14] J. Hoffman, K. McElroy, D-H Lee, K.M. Lang, H. Eisaki, S. Uchida and J.C. Davis, Science **297**, 1148 (2005)

[15] G. Cao, L. Balicas, W. H. Song, Y. P. Sun, Y. Xin, V. A. Bondarenko, J. W. Brill, S. Parkin and X. N. Lin, Phys. Rev. B **68**, 174409 (2003)

[16] V. Durairaj, S. Chikara, X. N. Lin, A. Douglass, G. Cao, P. Schlottmann, E. S. Choi and R. P. Guertin, Phys. Rev. B **73**, 214414 (2006)

[17] S. Chikara, V. Durairaj, W. H. Song, Y. P. Sun, X. N. Lin, A. Douglass, G. Cao, P. Schlottmann and S. Parkin, Phys. Rev. B **73**, 224420 (2006)

[18] H Nakatsugawa, E Iguchi and Y Oohara, J. Phys.: Condens. Matter **14**, 415 (2002)

[19] A. J. Williams, A. Gillies, J. P. Attfield, G. Heymann, H. Huppertz, M. J. Martínez-Lope and J. A. Alonso, Phys. Rev. B **73**, 104409 (2006)

[20] B. Dabrowski, S. Kolesnik, O. Chmaissem, T. Maxwell, M. Avdeev, P. W. Barnes and J. D. Jorgensen, Phys. Rev. B **72**, 054428 (2005)

[21] L. Capogna, E. M. Forgan, S. M. Hayden, A. Wildes, J. A. Duffy, A. P. Mackenzie, R. S. Perry, S. Ikeda, Y. Maeno and S. P. Brown, Phys. Rev. B **67**, 012504 (2003)

[22] H. Yamada, Phys. Rev. B. **47**, 11211 (1993)

[23] G. Cao, S. McCall, M. Shepard, J. E. Crow and R. P. Guertin, Phys. Rev. B **56**, 321 (1997)

[24] G. Cao, S. Chikara, J. W. Brill, P. Schlottmann, Phys. Rev. B **75**, 024429 (2007)

[25] Y. Sidis, M. Braden, P. Bourges, B. Hennion, S. NishiZaki, Y. Maeno and Y. Mori, Phys. Rev. Lett **83**, 3320 (1999)

[26] http://people.ccmr.cornell.edu/~jcdavis/mK_stm/

[27] S. H. Pan, E. W. Hudson and J. C. Davis, Rev. Sci. Inst. **70**, 1459 (1999)

[28] B.I. Barker, S.K. Dutta, C. Lupien, P.L. McEuen, N. Kikugawa, Y. Maeno and J.C. Davis, Physica B **329**, 1334 (2003)

4. $Sr_3(Ru_{1-x}Cr_x)_2O_7$

4.1 Motivation

Titanium cations are probably in the nonmagnetic Ti^{4+} state when they are substituted onto the ruthenium lattice sites of $Sr_3Ru_2O_7$. It is also desirable to investigate the influence of *magnetic* cations on the electronic properties of $Sr_3Ru_2O_7$. Mathieu *et al.* [1] studied single crystals of $Sr_3(Ru_{1-x}Mn_x)_2O_7$ − manganese cations are usually stable as Mn^{3+} or Mn^{4+}, both of which have a nonzero magnetic moment. Chromium cations are, likewise, usually found with a 3+ or 4+ nominal valence in perovskite TMOs. A decision was made to replace some of the Ru^{4+} ions in $Sr_3Ru_2O_7$ with Cr ions. Chromium-doping has been reported for other perovskite ruthenates, namely $SrRu_{1-x}Cr_xO_3$ [2,3,4] and $CaRu_{1-x}Cr_xO_3$ [3]. In this latter case only a small amount of doping ($x \sim 0.05$) was enough to promote magnetic ordering out of the paramagnetic ground state of $CaRuO_3$.

The valence state of a TM cation is inextricably linked to the occupation of its *d* orbitals and, hence, to its spin configuration. The importance of the orbital degree of freedom in TMOs was briefly referred to in section 1.1. This degree of freedom in many oxides has been explored in recent years by resonant X-ray scattering [5]. RXS experiments on crystals of Mn-doped $Sr_3Ru_2O_7$ referred to in the previous paragraph have been made by Professor Andrea Damascelli, who suggested the substitution of chromium atoms into $Sr_3Ru_2O_7$. Crystals referred to in this chapter have, along with Ti- and La-doped $Sr_3Ru_2O_7$ crystals, been provided to the group of Professor Damascelli.

4.2 Crystal Growth and Chemical Characterisation

$SrCO_3$, Cr_2O_3 and RuO_2 powders were mixed in the ratio 3: x : 2.52(1-x) and a feed-rod was made with the procedure described in section 2.1.2. Three crystal growth runs

were attempted; the nominal Cr content of batches Cr3, Cr4 and Cr5 was $x = 0.01$, 0.05 and 0.1, respectively.

4.2.1 X-ray Diffraction

The X-ray diffraction patterns of batches Cr3 and Cr4 are dominated by the diffraction peaks of the bilayer phase. Batch Cr5 was not considered for further study because the bilayer phase was a minority constituent. Batches Cr3 and Cr4 are the highest quality (in terms of having the smallest fractions of $SrRuO_3$ and $Sr_4Ru_3O_{10}$ impurity phases) of all the cation-doped $Sr_3Ru_2O_7$ referred to in this thesis. To the unaided eye, the *ab*-planes of these crystals appear very smooth, with only minor distortions evident. The molar percentage of ferromagnetic intergrowths in these crystals is estimated in section 4.3.1.

4.2.2 Energy Dispersive X-ray Analysis

The concentration of chromium cations in batches Cr3 and Cr4 was deduced from EDX measurements; the Cr K_α peak at $E = 5.41$ keV was considered. It was determined that $x = 0.0064 \pm 0.0009$ and 0.021 ± 0.002 for Cr3 and Cr4, respectively. These x values are *significantly* smaller than the nominal x values. A large discrepancy between the actual and the nominal chromium content of these crystals may arise from a number of sources. It is unclear how the Sr-Ru-Cr-O phase diagram behaves in the environment within an image furnace; Cr_2O_3, like RuO_2, may be susceptible to evaporation out of the molten zone. A discrepancy between the nominal and measured Cr content has also been recorded in crystals of $Sr_2Ru_{1-x}Cr_xO_4$ grown in the St Andrews image furnace.

4.3 Magnetisation

4.3.1 Intergrowth Contributions

Using the analysis described in section 3.3.1 the molar percentages of $SrRuO_3$ and $Sr_4Ru_3O_{10}$ in each batch of $Sr_3(Ru_{1-x}Cr_x)_2O_7$ has been deduced. These values, listed in

Table 4.1, are *much* smaller than the intergrowth percentages in any of the $Sr_3(Ru_{1-x}Ti_x)_2O_7$ crystals, thus confirming the relatively high crystalline quality of these batches.

Batch	Molar Percentage of $Sr_4Ru_3O_{10}$	Molar Percentage of $SrRuO_3$
Cr3, $x = 0.006$	0.08	0.18
Cr4, $x = 0.02$	0.31	0.05

Table 4.1. The estimated molar percentages of $SrRuO_3$ and $Sr_4Ru_3O_{10}$ intergrowths in batches Cr3 and Cr4.

4.3.2 *B || ab*

$\chi(T)$ of $x = 0$, 0.006 and 0.02 is displayed in Figure 4.1. No difference in $\chi_{ZFC}(T)$ and $\chi_{FC}(T)$ was observed with this field orientation for any of these materials. The distinctive peak in $\chi(T)$ is shifted in temperature from 16 K for $Sr_3Ru_2O_7$ to 15 K for $x = 0.006$. At temperatures below approximately 25 K the susceptibility of $x = 0.02$ is greater than $\chi(T)$ of $x = 0$ or 0.006. $\chi(T)$ of $x = 0.02$ peaks at $T = 6$ K and decreases in value by a relatively small amount at lower temperatures.

The inset to Figure 4.1 displays the magnetisation of $Sr_3Ru_2O_7$ and the Cr-doped samples as a function of magnetic field. A super-linear rise in $M(B)$ of both $x = 0$ and 0.006 is clear. The magnetisation of $x = 0.006$ rises to the same value (0.26 μ_B/Ru at 5 Tesla) as $M(B)$ of $Sr_3Ru_2O_7$ but the super-linear rise in $M(B)$ of this Cr-doped material is broader in field range than the equivalent feature in $M(B)$ of $Sr_3Ru_2O_7$. The variation with field of the magnetisation of $x = 0.02$ is *qualitatively* different to $M(B)$ of $x = 0$ and 0.006: M varies linearly with B at low fields but no super-linear rise in magnetisation is seen in the field range up to 5 Tesla. The low field slope of $M(B)$ increases from 0.025 $(\mu_B/Ru)T^{-1}$ for $Sr_3Ru_2O_7$ to 0.028 and 0.048 $(\mu_B/Ru)T^{-1}$ for $x = 0.006$ and 0.02, respectively.
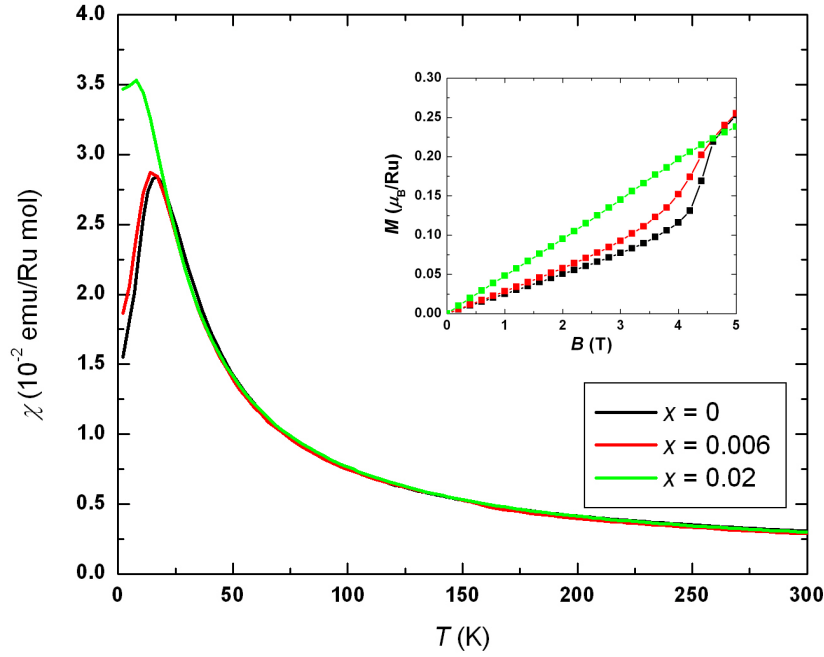
Figure 4.1. $\chi(T)$ of $x = 0$, 0.006 and 0.02, measured with $B = 0.3$ T. The inset shows the magnetisation of each sample as a function of field at $T = 2$ K.

4.3.3 $B \parallel c$

Figure 4.2 shows $\chi(T)$ of $x = 0$, 0.006 and 0.02 when the external magnetic field is parallel to the c-axis of each material. $\chi(T)$ of $x = 0.006$ peaks at $T = 14$ K, a temperature which is slightly less than 16 K, the temperature at which $\chi(T)$ of $Sr_3Ru_2O_7$ peaks. In addition to the susceptibility peak a *minimum* in $\chi(T)$ of $x = 0.006$ is observed at $T \sim 8$ K and, at temperatures below this, $\chi(T)$ rises as a function of decreasing temperature. There is no difference in $\chi_{ZFC}(T)$ and $\chi_{FC}(T)$ of either $x = 0$ or 0.006. A difference in the FC and ZFC magnetisation of $x = 0.02$ at low temperatures *is* clear: $\chi_{ZFC}(T)$ is sharply peaked at $T = 6$ K but a much weaker temperature dependence of $\chi_{FC}(T)$ is observed. The inset to Figure 4.2 clearly shows the difference in $\chi_{ZFC}(T)$ and $\chi_{FC}(T)$ of $x = 0.02$, measured with a lower magnetic field. The peak in $\chi_{ZFC}(T)$ is coincident in temperature with a change in slope (or 'kink') of $\chi_{FC}(T)$.

Magnetic irreversibility is indicated by the difference in the FC and ZFC susceptibilities of $x = 0.02$. It was desirable to search for signatures of this irreversibility in $M(B)$. The magnetisation of the three materials as a function of field is displayed in Figure 4.3. As the magnetic field was swept up and then down no hysteresis was seen in the magnetisation of $x = 0$ or 0.006. By contrast, hysteresis in $M(B)$ of $x = 0.02$ *is* evident; a remanence of 0.008 μ_B/Ru and coercive field of 0.125 Tesla are associated with the hysteresis loop.
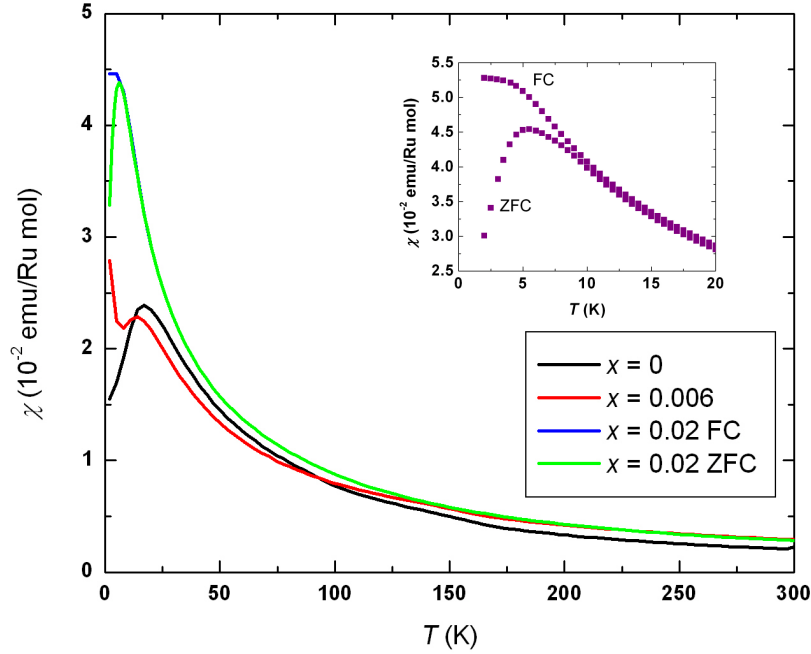
Figure 4.2. $\chi(T)$ **of** x **= 0, 0.006 and 0.02, measured with** B **= 0.3 T. The inset shows** $\chi(T)$ **of** x **= 0.02 at low temperatures, measured with** B **= 0.1 T.**

A peak in $\chi_{ZFC}(T)$ at some temperature T^* alongside a change in slope or 'kink' in $\chi_{FC}(T)$ at a temperature similar to T^* may be a signature of a glassy magnetic state. Minakata and Maeno [6] observed these features in the susceptibility of $Sr_2Ru_{1-x}Ti_xO_4$ ($x = 0.025$). The remanent magnetisation of this material was found to decay logarithmically with time, t, as $t \rightarrow \infty$. It was therefore desirable to investigate any time-dependence of the remanent magnetisation of $x = 0.02$. The inset to Figure 4.3 displays the remanent magnetisation of $x = 0.02$ at $T = 2$, 4 and 6 K as a function of time. The sample was cooled from 300 K in zero field to each temperature; an external field of 5 Tesla was then applied to the sample; this field was subsequently

reduced to back to zero and the magnetisation of the sample was then measured as a function of time. It is clear that as $t \rightarrow \infty$, $M_{rem}(t) = M_{rem}(t_0) - H(\ln(t))$, where t_0 is some arbitrary time. $H = 0.064$, 0.023 and 0.004 (μ_B/Cr) at $T = 2$, 4 and 6 K, respectively.
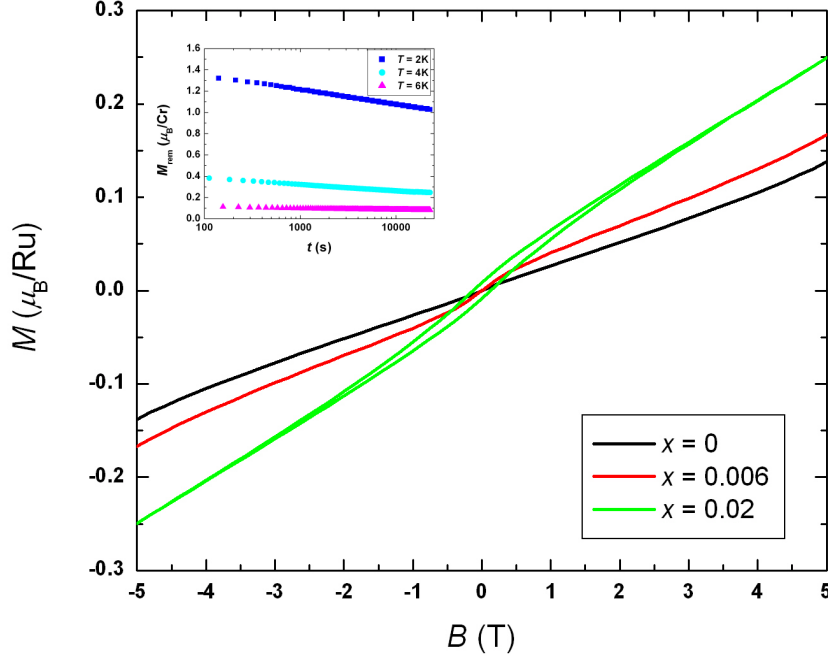
Figure 4.3. $M(B)$ **of** $x = 0$, 0.006 **and** 0.02 **at** $T = 2$ **K. The inset shows the remanent magnetisation of** $x = 0.02$ **as a function of time at** $T = 2$, 4 **and** 6 **K.**

4.3.4 $x = 0.006$

It is possible that the upturn in $\chi(T)$ of $x = 0.006$ in Figure 4.2 is a precursor to the magnetic irreversibility of $x = 0.02$. Associated with this upturn is a $1/T$ temperature dependence; the results displayed in Figures 4.1 and 4.2 also imply that this feature is suppressed when the magnetic field is rotated towards the crystalline ab-planes. This striking upturn in $\chi(T)$ of $x = 0.006$ is explored here in more detail.

4.3.4.1 Angular Variation of $\chi(T)$

The upturn in $\chi(T)$ of $x = 0.006$ is observed when $B \parallel c$ but not when $B \parallel ab$. It was therefore desirable to investigate the variation with field angle, θ, of the susceptibility

of this material at low temperatures. For measurements in the MPMS magnetometer samples can be mounted within drinking straws so that the *c*-axis ($\theta = 0°$) or the *ab*-plane ($\theta = 90°$) is parallel to the external magnetic field. Intermediate angles cannot be attained by using only drinking straws. To overcome this problem a small holder was made from a piece of clear, rigid plastic. One surface of this holder was cut to the required angle and the sample was then fixed onto this flat surface with a small amount of grease. The holder was subsequently placed inside the plastic straw; the susceptibility of the holder was comparable to the (small) magnetic susceptibility of the straw.
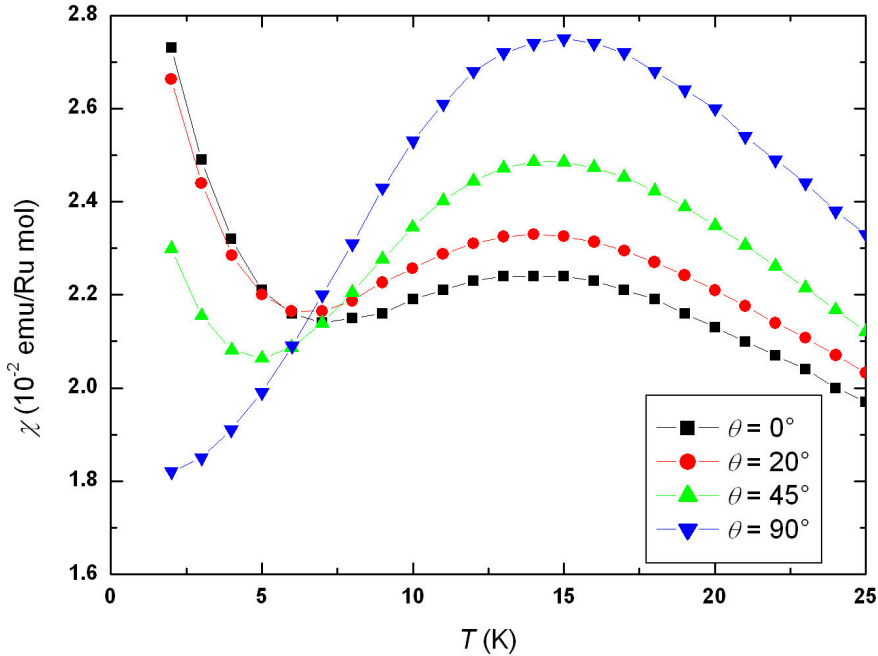
Figure 4.4. $\chi(T)$ of $x = 0.006$ measured with the crystalline *c*-axis tilted at various angles, θ, to an external magnetic field of 0.3 T.

Figure 4.4 shows $\chi(T)$ of $x = 0.006$ with $\theta = 0, 20, 45$ and $90°$. A minimum and maximum in $\chi(T)$ at $T_{min} = 7$ K and $T_{max} = 14$ K, respectively, are evident when $\theta = 0°$. As a function of angle the maximum in $\chi(T)$ is shifted in temperature by approximately 1 K overall, from 14 K when $\theta = 0°$ to 15 K when $\theta = 90°$. The minimum in $\chi(T)$ is shifted to $T_{min} = 6$ and 5 K when $\theta = 20$ and $45°$, respectively. When $\theta = 90°$ no minimum in $\chi(T)$ is seen down to $T = 2$ K. It is therefore clear that

increasing the component of magnetic field parallel to the *ab*-planes of the crystal causes a shift to lower temperatures of the minimum in $\chi(T)$.

4.3.4.2 Variation of $\chi(T)$ with B

Figure 4.5 shows, for various values of magnetic field parallel to the *c*-axis, $\chi(T)$ of x = 0.006. A peak in $\chi(T)$ is seen at T_{max} = 14 K for all field values. A minimum in $\chi(T)$ at T_{min} = 7.5 K is depressed to T_{min} = 7, 6.5 and 5 K when B increases from 0.1 T to 0.3, 0.6 and 1 T, respectively. When B = 2 T no minimum in $\chi(T)$ is seen. Also, no minimum in $\chi(T)$ occurs when larger magnetic fields up to 5 Tesla are applied (not shown in Figure 4.5). Overall, increasing the magnitude of the out-of-plane magnetic field has a qualitatively similar effect as increasing the *in-plane* component of magnetic field does, namely the depression to lower temperatures of the susceptibility minimum.
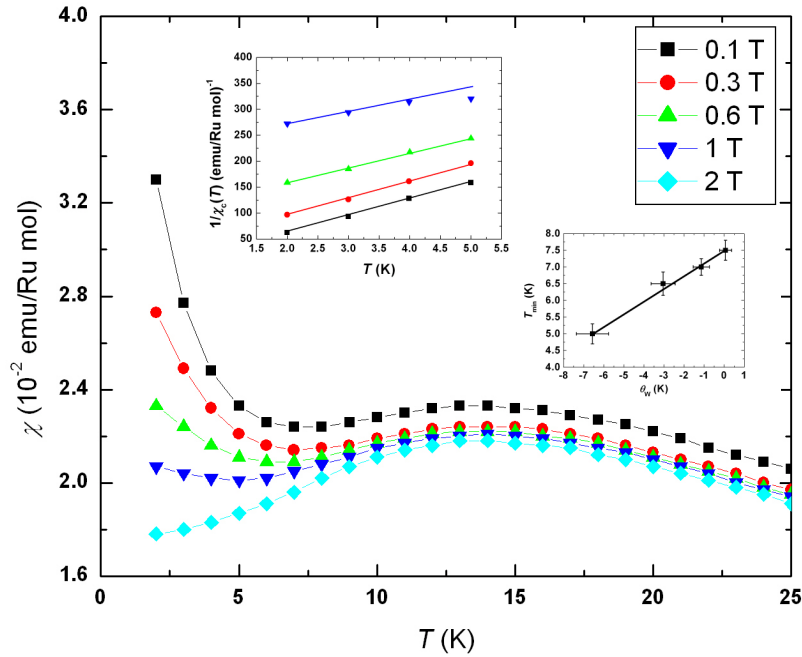

Figure 4.5. $\chi(T)$ of x = 0.006 measured with different magnetic fields. The upper inset shows $\chi_C^{-1}(T)$ at temperatures less than T_{min}, measured with B = 0.1, 0.3, 0.6 and 1 T; the slope of each trendline is 32.4 (emu/Ru mol)$^{-1}$K^{-1}. Shown in the lower inset is T_{min} plotted against θ_W.

$\chi(T)$ is proportional to $1/T$ at temperatures less than T_{min}. It is assumed that this $1/T$ contribution, denoted as $\chi_C(T)$, acts in addition to the Pauli susceptibility, such that

$$\chi(T) = \chi_P + \chi_C(T). \qquad (4.1)$$

It is difficult to extract χ_P from those data in which a minimum in $\chi(T)$ is seen. However, when $B = 2$ T no minimum is seen and $\chi(T)$ extrapolated to $T = 0$ is 1.75×10^{-2} emu/Ru mol, the value assumed to be χ_P of $x = 0.006$. It is also assumed that this susceptibility is independent of temperature and magnetic field. The inverse of χ_C is plotted against temperature in Figure 4.5. When $B = 0.1$, 0.3 and 0.6 T $\chi_C^{-1}(T)$ is proportional to T across the entire range of temperatures shown; the constant of proportionality is 32.4, 33.2 and 28.8 (emu/Ru mol)$^{-1}$K^{-1}, respectively.

When $B = 2$ T $\chi_C^{-1}(T)$ is not proportional to T across the entire range because the minimum in $\chi(T)$ is at $T = 5$ K. T_{min} is largest when the field is low and the $1/T$ behaviour is likely to be captured best by the 0.1 T data: a slope of 32.4 (emu/Ru mol)$^{-1}$K^{-1} has, therefore, been fitted to each data. This slope fits *very* well to the 0.3 and 0.6 T data and also fits the two lowest temperature points of the 1 T data.

The Weiss temperature, θ_W, (the temperature at which $\chi_C^{-1}(T)$ extrapolates to zero) is 0.1, -1.1, -3.0 and -6.6 K when $B = 0.1$, 0.3, 0.6 and 1 T, respectively. The trend of θ_W decreasing as a function of field is *not* changed when the best-fit lines to the 0.3, 0.6 and 1T data are considered. θ_W for each data, deduced from the fit of 32.4(emu/Ru mol)$^{-1}$K^{-1} *and* from the best-fit to each data is listed in Table 4.2. It is also clear that T_{min} and θ_W both decrease as a function of field. The lower inset to Figure 4.5 displays these quantities plotted against each other; a linear trendline of $T_{min} = 0.4\theta_W + 7.5$ relates these two quantities.

$\chi_C(T) = G/T$, where G, the inverse of the aforementioned proportionality constant, is equal to 0.031 ± 0.001 (emu/Ru mol)K. This contribution to the susceptibility can be expressed in terms of the concentration of chromium ions by multiplying this number by the Ru/Cr ratio in the crystal, namely 0.994/0.006: $G = 5.14 \pm 0.16$ (emu/Cr mol)K. Blundell [7] shows that an effective magnetic moment associated with a $1/T$

dependence of $\chi(T)$ can be expressed as a number of Bohr magnetons per formula unit,

$$\mu_{\text{eff}} = 2.827\sqrt{\chi_{\text{M}}^{\text{cgs}}T} \, , \qquad (4.2)$$

where $\chi_{\text{M}}^{\text{cgs}}T$ is equivalent to G. It can therefore be concluded that the effective moment per Cr ion is $6.4 \pm 0.9 \, \mu_{\text{B}}$. The uncertainty of this effective moment arises from the uncertainty of the Cr x value. The effective moment expected from an isolated Cr^{4+} or Cr^{3+} ion (assuming that the orbital moment is quenched, so that $\mu_{\text{eff}} \approx 2\mu_B\sqrt{S(S+1)}$) is 2.8 and 3.8 μ_{B}, respectively. The effective moment per Cr ion in this material is, therefore, significantly larger than the effective moment of an isolated chromium cation.

B (T)	θ_W (K) obtained from Best-Fit	θ_W (K) obtained from fit to slope of 32.4 (emu/Ru mol)$^{-1}$K^{-1}
0.1	0.07	0.07
0.3	-0.87	-1.14
0.6	-3.49	-3.04
1	-10.89	-6.56

Table 4.2. The Weiss temperature extracted from fitting $\chi_c^{-1}(T)$ to (a) a slope of 32.4 (emu/Ru mol)$^{-1}$K^{-1} and, (b) to a best-fit slope, unique to each data. When B = 1 T $\chi_C(T)$ is not proportional to $1/T$ over the entire range of temperatures between 2 and 5 K, so the best-fit was to the 2, 3 and 4 K points only.

The nominal valence of the Cr cations is uncertain. For charge disorder to be minimised tetravalent Ru ions should be replaced by Cr^{4+} but, on the other hand, a $Ru^{4+} + Cr^{4+} \rightarrow Ru^{5+} + Cr^{3+}$ charge transfer may occur. Also, the size of the chromium ions relative to the ruthenium ions must be taken into account. The ionic radius of Cr^{3+} and Cr^{4+} is 61.5 and 55 pm, respectively; Ru^{4+} has a radius of 62 pm (these numbers are for a 6-coordinate octahedral environment). Therefore, compared to Cr^{4+} ions, Cr^{3+} ions will cause a smaller change to the perovskite tolerance factor. Overall, if it is assumed that the orbital moment of the Cr cations is quenched, the polarisation

attributable to the electron fluid is 3.6 ± 0.9 or 2.6 ± 0.9 μ_B/Cr if the chromium valence is 4+ or 3+, respectively.

4.4 Heat Capacity

Figure 4.6 shows C/T of $x = 0$, 0.006 and 0.02 as a function of temperature squared. C/T of each sample is proportional to T^2 at high temperatures; $\beta = 0.209 \pm 0.008$, 0.232 ± 0.006 and 0.237 ± 0.008 mJ/Ru mol K^4 for $x = 0$, 0.006 and 0.02 respectively.
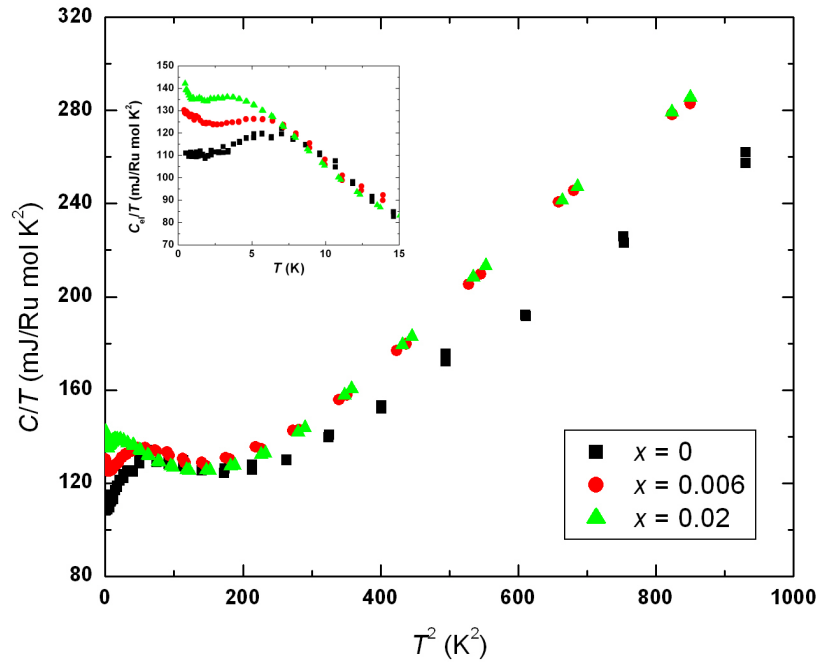
Figure 4.6. C/T of $x = 0$, 0.006 and 0.02 as a function of temperature squared. The inset displays C_{el}/T of each sample at temperatures below 15 K.

C_{el}/T of each sample as a function of temperature is shown in the inset to Figure 4.6. C_{el}/T of $x = 0$ rises from a low temperature value of 110 mJ/Ru mol K^2 to a maximum of 119 mJ/Ru mol K^2 at $T = 7.5$ K. A broad peak is also seen in C_{el}/T of $x = 0.006$: this peak of 126 mJ/Ru mol K^2 at $T \sim 6$ K is not, however, the maximum of C_{el}/T; a broad minimum is seen at $T = 2.5$ K and C_{el}/T rises as a function of decreasing temperature to 130 mJ/Ru mol K^2 at 400 mK. Qualitatively similar behaviour is also seen in C_{el}/T of $x = 0.02$: a broad peak of 137 mJ/Ru mol K^2 at $T = 3$ K alongside a minimum at $T \sim$ 1.5 K, followed by a rise in C_{el}/T to 141 mJ/Ru mol K^2 at $T = 400$ mK. The upturn in

C_{el}/T of the Ti-doped $x = 0.025$ and 0.05 samples was shown to diverge logarithmically with temperature (section 3.4). However, the upturn in C_{el}/T of these Cr-doped samples does *not* extend over a full decade of temperature and a $\ln(T)$ temperature dependence cannot be claimed.

4.5 Resistivity as a Function of Temperature

$\rho_{ab}(T)$ of $Sr_3(Ru_{1-x}Cr_x)_2O_7$ at temperatures between 0.1 and 300 K is displayed in Figure 4.7. The residual in-plane resistivity of $x = 0$, 0.006 and 0.02 is 1.2, 8 and 21 $\mu\Omega$cm, respectively. The inset to Figure 4.7 shows $(\rho_{ab}\text{-}\rho_{ab0})/T^2$ of these samples. T_{FL} is depressed from 8.2 K for $Sr_3Ru_2O_7$ to 5.7 K for $x = 0.006$. It is not certain that a T_{FL} can be extracted from the $x = 0.02$ data because the measurement is dominated by noise at low temperatures. If, however, it is assumed that there *is* a change of slope of $(\rho_{ab}\text{-}\rho_{ab0})/T^2$ of $x = 0.02$, an upper limit of T_{FL} is 1.4 K. The A coefficient increases from 0.08 $\mu\Omega$cmK^{-2} for $Sr_3Ru_2O_7$ to 0.093 and 0.126 $\mu\Omega$cmK^{-2} for $x = 0.006$ and 0.02, respectively, assuming that $\rho_{ab}(T)$ of $x = 0.02$ is proportional to T^2 at temperatures below the putative T_{FL}.
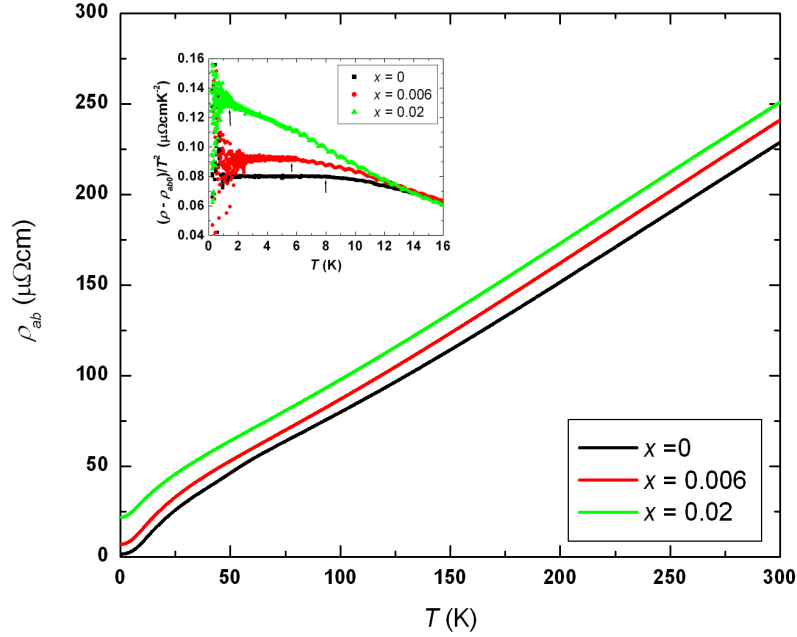

Figure 4.7. $\rho_{ab}(T)$ of $x = 0$, 0.006 and 0.02. The inset shows $(\rho_{ab}\text{-}\rho_{ab0})/T^2$ of each material; the arrows point to T_{FL}.

4.6 Magnetoresistance

Shown in Figure 4.8 is magnetoresistance ($B \parallel I \parallel ab$) of $x = 0$, 0.006 and 0.02 with T = 400 mK. The features in $\rho_{ab}(B)$ of $x = 0.006$ and 0.02 are less distinctive than the sharp features in $\rho_{ab}(B)$ of $Sr_3Ru_2O_7$. A broad peak in $\rho_{ab}(B)$ of $x = 0.006$ is clear at a field of 4.8 T; features in $\rho_{ab}(B)$ of this material are also clear at fields of 5.05 and 5.8 T, similar to B_M and B_{M2} of $Sr_3Ru_2O_7$. The magnetoresistance of $x = 0.02$ passes through a very broad peak at 3.5 T and decreases with field above this value. The inset to Figure 4.8 shows $\rho_{ab}(B)$ of $x = 0.006$ at different temperatures: no qualitative changes are seen in $\rho_{ab}(B)$ as temperature is raised from 400 mK to 1200 mK.
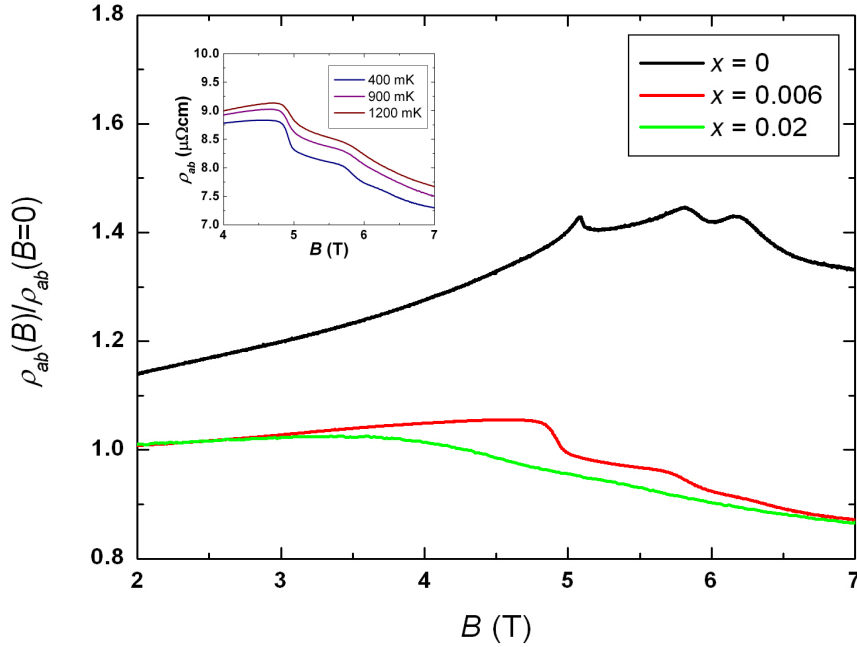
Figure 4.8. The magnetoresistance, $\rho_{ab}(B)/\rho_{ab}(B = 0)$, of $x = 0$, 0.006 and 0.02 at T = 400 mK. The inset shows $\rho_{ab}(B)$ of $x = 0.006$ at $T = 400$, 900 and 1200 mK. ρ_{ab0} of $x = 0$, 0.006 and 0.02 is 1, 8 and 21 $\mu\Omega$cm, respectively.

4.7 Discussion

The main observations reported in this chapter are:

- A relatively small amount of chromium substitution —$x = 0.006$— into $Sr_3Ru_2O_7$ leads to a $1/T$ contribution to the magnetisation ($B \parallel c$) at low

temperatures (Figure 4.2). This upturn in the magnetisation has associated with it an effective magnetic moment of more than 6 μ_B per chromium ion.

- Magnetic irreversibility at low temperatures is observed in the material with a greater chromium concentration, namely $x = 0.02$. This irreversibility is time-dependent; the remanent magnetisation decays logarithmically with time (Figure 4.3).

- The Fermi liquid A coefficient is enhanced by chromium-doping; T_{FL}, the maximum temperature to which the T^2-resistivity regime extends, decreases as a function of doping (Figure 4.7). In addition, chromium substitution induces an upturn in the electronic heat capacity at low temperatures (Figure 4.6).

The crystals of $x = 0.006$ and 0.02 reported in this chapter have a relatively small percentage of $SrRuO_3$ and $Sr_4Ru_3O_{10}$ intergrowths and, consequently, the reliable magnetisation data obtained from these crystals are the basis of much of the discussion provided here. Mathieu and colleagues [1] refer to the use of SQUID magnetometry in revealing "minor impurities of Sr_2RuO_4 and traces of the ferromagnetic $Sr_4Ru_3O_{10}$" in their $Sr_3(Ru_{1-x}Mn_x)_2O_7$ crystals but do *not* report any magnetisation measurements to support their major claim, namely that $Sr_3Ru_2O_7$ is driven into an antiferromagnetic insulating state by doping with a small concentration of manganese ions. The main conclusions of this chapter *are* supported by magnetisation measurements.

The magnetisation of $Sr_3Ru_2O_7$ is changed significantly by doping with a small concentration of chromium cations. The metamagnetic feature in $M(B)$ ($B \parallel ab$) of $x = 0.006$ is broadened in field range with respect to the equivalent feature in the magnetisation of $Sr_3Ru_2O_7$. *No* evidence of metamagnetism is seen in samples of $x = 0.02$ with this field orientation. For fields parallel to the crystalline c-axis the effects of Cr-doping are remarkable. An upturn in $\chi(T)$ of $x = 0.006$ is seen at low temperatures; this upturn is proportional to $1/T$ and has an effective magnetic moment of more than 6 μ_B/Cr associated with it. The upturn is superimposed onto the main susceptibility peak and, hence, a minimum in $\chi(T)$ is seen in the intermediate temperature range. This minimum is shifted to lower temperatures when the (out-of-plane) magnetic field is enhanced. A depression to lower temperatures of this

minimum is, likewise, observed when the *in-plane* component of field is increased, by tilting the crystal with respect to the external field. Magnetic irreversibility is observed in samples of $x = 0.02$ at temperatures below approximately 6 K; the remanent magnetisation of the low temperature magnetic state decays logarithmically with time. The following paragraphs give an opinion of how the susceptibility upturn of $x = 0.006$ and the glassy magnetism of $x = 0.02$ may arise, and how these features may relate to each other.

It is possible that the $1/T$ contribution to $\chi(T)$ of $x = 0.006$ at low temperatures can be attributed to magnetic entities which interact weakly with each other, similar in some respects to a Curie-type $1/T$ susceptibility arising from non-interacting local moments. An effective moment of more than 6 μ_B/Cr implies that these entities are not isolated Cr cations. One possibility is that each Cr cation has an 'island' of magnetic polarisation around it. The Pauli contribution to the susceptibility of $x = 0.006$ is *not* less than χ_P of $Sr_3Ru_2O_7$ and, hence, the number of Landau quasiparticles is not reduced by Cr-doping. Furthermore, there is no upturn in the resistivity of $x = 0.006$ at low temperatures; localisation of carriers around each Cr cation can therefore be ruled out. One possibility is that the 'island' of magnetism around each Cr cation is associated with a smoothly-varying polarisation of the $Sr_3Ru_2O_7$ electron fluid.

Blundell [7], Gehring [8] and Guimarães [9] discuss the effects of placing magnetic impurities into paramagnetic metals. A magnetic impurity can induce an oscillatory magnetisation around itself which, consequently, polarises the surrounding fluid of electrons. This polarisation can interact with other magnetic impurities and there is, therefore, a long-range interaction between the magnetic ions which is oscillatory in real-space − this is the *Ruderman–Kittel–Kasuya–Yoshida* (RKKY) interaction. This interaction oscillates between ferromagnetic and antiferromagnetic coupling and decays as a function of distance from the magnetic impurity ion.

The oscillation between antiferromagnetic and ferromagnetic coupling may lead to magnetic frustration and the system may be unable to relax into a magnetic ground state: 'freezing' of the spins may occur at some particular temperature T_f, below which spins are fixed in a particular configuration. Non-reversible behaviour and, hence, magnetic hysteresis is a consequence of a frozen spin configuration [10]. For

instance, non-reversible behaviour can be seen when a very small amount (few ppm) manganese ions are dissolved into copper: the RKKY interaction between the Mn ions is mediated by the Cu conduction electrons. However, this type of scenario is *not* applicable to $Sr_3(Ru_{1-x}Cr_x)_2O_7$ because no hysteresis in the magnetisation of $x = 0.006$ has been observed.

A magnetisation which varies smoothly in real-space can, in principle, arise from a susceptibility which is sharply-peaked in **q**-space. $Sr_3Ru_2O_7$ has a zero-field Wilson ratio of approximately 10 and, consequently, the susceptibility is thought to be exchange-enhanced in the vicinity of $\mathbf{q} = 0$. This exchange-enhanced susceptibility is a possible origin of a smoothly-varying island of magnetic polarisation around each Cr ion. A comparison can be made between $Sr_3(Ru_{1-x}Cr_x)_2O_7$ and PdFe [11,12]; palladium, like $Sr_3Ru_2O_7$, is on the verge of a ferromagnetic instability. When iron impurities are alloyed into Pd 10 μ_B 'giant moments' can emerge around each iron ion. If it is assumed that an island of magnetic polarisation originates is centred about each Cr ion in the $x = 0.006$ material, one possible explanation of the magnetic irreversibility of $x = 0.02$ is that, above a certain doping level, these islands interact with each other by the RKKY mechanism.

Minakata and Maeno [6] observed time-dependent magnetic behaviour in $Sr_2Ru_{1-x}Ti_xO_4$, $x = 0.025$; an effective moment of ~ 0.5 μ_B/Ti was deduced. Braden *et al.* [13] suggest magnetic frustration in this material may arise from competition between disorder (from the Ti scattering centres) and the onset of a spin density wave (which is observed in heavily Ti-doped samples). Because the Ti cations in this material are in the nonmagnetic 4+ valence state, *all* of the 0.5 μ_B/Ti can be attributed to itinerant carriers. By contrast, the Cr cations $Sr_3(Ru_{1-x}Cr_x)_2O_7$ *do* have an intrinsic magnetic moment. If the orbital moment of the Cr cations is assumed to be quenched the magnetic polarisation attributable to the electron fluid is 3.6 or 2.6 μ_B/Cr if the chromium valence is 4+ or 3+, respectively. Either of these values is *much* larger than the moment given to the itinerant carriers per dopant ion in $Sr_2Ru_{1-x}Ti_xO_4$. Another major difference between the glassy magnetism of Cr $x = 0.02$ and that of $Sr_2Ru_{1-x}Ti_xO_4$ is clear in the decay profile of the remanent magnetisation. In the notation of $M_{rem}(t) = M_{rem}(t_0) - H\ln(t)$, Minakata and Maeno find that H is maximised when $T = T_f$. By contrast, the inset to Figure 4.3 clearly shows that H of $x = 0.02$ maximised at

low temperatures. Overall, it seems likely that the glassy magnetism of $Sr_3(Ru_{1-x}Cr_x)_2O_7$ has a different origin to that of $Sr_2Ru_{1-x}Ti_xO_4$.

An upturn in C_{el}/T of the Cr-doped samples is evident at low temperatures. The upturn in C_{el}/T of some of the $Sr_3(Ru_{1-x}Ti_x)_2O_7$ was attributed to critical magnetic fluctuations – it is possible that the upturn in C_{el}/T of these Cr-doped samples can also be attributed to critical fluctuations. The suppression of T_{FL} as a function of x is also striking. The residual in-plane resistivity of Cr $x = 0.02$ is ~ 25 $\mu\Omega$cm, comparable to ρ_{ab0} of Ti $x = 0.025$. T_{FL} of this latter material is approximately 6 K; the putative T_{FL} of Cr $x = 0.02$ is ≤ 1.4 K. In qualitative terms, Fermi liquid theory remains valid if there is a restricted region of phase space into which quasiparticles can be scattered; any breakdown of Fermi liquid theory may be attributed to the emergence of additional phase space, possibly due to critical fluctuations.

4.8 References

[1] R. Mathieu, A. Asamitsu, Y. Kaneko, J. P. He, X. Z. Yu, R. Kumai, Y. Onose, N. Takeshita, T. Arima, H. Takagi and Y. Tokura, Phys. Rev. B **72**, 092404 (2005)

[2] A. J. Williams, A. Gillies, J. P. Attfield, G. Heymann, H. Huppertz, M. J. Martínez-Lope and J. A. Alonso, Phys. Rev. B **73**, 104409 (2006)

[3] V. Durairaj, S. Chikara, X. N. Lin, A. Douglass, G. Cao, P. Schlottmann, E. S. Choi and R. P. Guertin, Phys. Rev. B **73**, 214414 (2006)

[4] B. Dabrowski, S. Kolesnik, O. Chmaissem, T. Maxwell, M. Avdeev, P. W. Barnes and J. D. Jorgensen, Phys. Rev. B **72**, 054428 (2005)

[5] Y. Murakami, H. Nakao, T. Matsumura and H. Ohsumi, J. Mag. Mag. Mat. **310**, 723 (2007)

[6] M. Minakata and Y. Maeno, Phys. Rev. B **63**, 180504 (2001)

[7] S. J. Blundell, *Magnetism in Condensed Matter*, Oxford University Press (2001)

[8] G. A. Gehring in *Spin Electronics*, edited by M. Ziese and M. J. Thornton, Springer (2001)

[9] A. P. Guimarães, *Magnetism and Magnetic Resonance in Solids*, Wiley (1998)

[10] K. H. Fischer and J. A. Hertz, *Spin Glasses*, Cambridge University Press (1991)

[11] R. Segnan, Phys. Rev. **160**, 404 (1967)

[12] A. M. Clogston, B. T. Matthias, M. Peter, H. J. Williams, E. Corenzwit and R. C. Sherwood, Phys. Rev. **125**, 541 (1962)

[13] M. Braden, O. Friedt, Y. Sidis, P. Bourges, M. Minakata and Y. Maeno, Phys. Rev. Lett. **88**, 197002 (2002)

5. $(Sr_{1-y}La_y)_3Ru_2O_7$

5.1 Motivation

Titanium and chromium cations substitute onto the ruthenium sites in the crystal lattice of $Sr_3Ru_2O_7$. Foreign cations can also be introduced *out* of the conducting RuO_2 planes. The replacement of Sr^{2+} ions in $Sr_3Ru_2O_7$ with isovalent calcium ions has been reported previously [1]. *Non*-isovalent substitution onto the Sr sites has been performed in the context of Sr_2RuO_4: Kikugawa and colleagues [2-5] studied some of the electronic properties of $Sr_{2-y}La_yRuO_4$ – lanthanum cations are known to be stable as nonmagnetic La^{3+}. It was shown that one additional electron is added to the electronic structure for each lanthanum ion doped into the lattice – this 'electron doping' caused a rigid shift of the Fermi level to a higher energy, towards a van Hove singularity in the electronic density of states.

La-doping is particularly interesting in the context of $Sr_3Ru_2O_7$ because peak(s) in the density of states in the vicinity of E_F may contribute to the metamagnetism: if the rigid band-shift scenario remains applicable to $Sr_3Ru_2O_7$, adding electrons to the valence band may 'tune' the Fermi level towards or away from these peaks and, hence, cause a measurable change in the value of metamagnetic field. In addition, because lanthanum cations substitute out of the RuO_2 planes, the rate of change of residual *in-plane* resistivity with La-doping is likely to be much less severe than the enhancement of ρ_{ab0} due to Ti- or Cr-doping. Results from in the previous two chapters indicated that doping cations onto the ruthenium lattice sites caused a broadening of sharp features in some of the electronic properties of $Sr_3Ru_2O_7$. It was anticipated that lanthanum substitution into $Sr_3Ru_2O_7$ would allow the evolution with electron-doping of some of these properties to be explored in a relatively low-disorder environment. This low-disorder context has been an *essential* basis for a key focus of this chapter – showing that Yamada theory does not adequately describe the metamagnetism of $Sr_3Ru_2O_7$.

5.2 Crystal Growth and Characterisation

$SrCO_3$, RuO_2 and La_2O_3 powders were mixed in the ratio $3(1-y)$: 2.52: $3y/2$. La_2O_3 absorbs water and carbon dioxide from the atmosphere so, prior to being mixed with the other powders, was dried in air at 1000°C; the dried La_2O_3 powder was then weighed a few minutes after being removed to room temperature. A feed rod was made according to the procedure described in section 2.1.2 and the conditions in the image furnace were unchanged from those described in section 2.1.4. Some of the crystal growths were unsuccessful; three batches (L2, L3 and L4) from a total of six were used for further study.

5.2.1 X-ray Diffraction

Signatures of Sr_2RuO_4, $Sr_4Ru_3O_{10}$ and $SrRuO_3$ were observed in the X-ray diffraction patterns of crushed crystals of L2, L3 and L4 to a similar extent as in samples of $Sr_3(Ru_{1-x}Ti_x)_2O_7$. The content of ferromagnetic intergrowths in the La-doped samples is estimated in section 5.3.1. Also, the quasi-2D crystal structure of $Sr_3Ru_2O_7$ is *not* disturbed by the lanthanum substitution described here: the *c*-axis lattice parameter of crystals of L2, L3 and L4 is unchanged from that of $Sr_3Ru_2O_7$, namely 20.7 Å.

5.2.2 Energy Dispersive X-ray Analysis

Batch	y_a
L3, $y_n = 0.005$	0.0048 ± 0.0009
L2, $y_n = 0.01$	0.011 ± 0.002
L4, $y_n = 0.02$	0.019 ± 0.002

Table 5.1. The nominal and actual lanthanum concentration of each batch of $(Sr_{1-y}La_y)_3Ru_2O_7$.

The lanthanum content of each batch was deduced from EDX measurements with a $LaCrO_3$ standard; the lanthanum L_α peak at $E = 4.65$ keV was considered. Table 5.1 lists the La y values of each batch. The measured and nominal y values are very

similar.

5.3 Magnetisation

5.3.1 Intergrowth Contributions

An estimation of the molar percentages of $SrRuO_3$ and $Sr_4Ru_3O_{10}$ intergrowths of each crystal batch was made according to the procedures described in section 3.3.1. These values, listed in Table 5.2, are of the same order of magnitude as the intergrowth percentages in each batch of $Sr_3(Ru_{1-x}Ti_x)_2O_7$. Furthermore, $\chi(T)$ of each of the $(Sr_{1-y}La_y)_3Ru_2O_7$ samples measured with a field of 0.3 T was qualitatively similar to $\chi(T)$ of the Ti-doped samples measured with an identical magnetic field (shown in Figure 3.1): kinks in $\chi(T)$ of the La-doped samples were clear at temperatures of approximately 100 and 160 K and the susceptibility at low temperatures was many times greater than $\chi(T)$ of undoped $Sr_3Ru_2O_7$. $\Delta\chi(T)$ and $\Delta M(B)$ of these La-doped samples is reported here (rather than $\chi(T)$ and $M(B)$).

Batch	$Sr_4Ru_3O_{10}$ molar percentage	$SrRuO_3$ molar percentage
L3, $y = 0.005$	5.0	1.7
L2, $y = 0.01$	4.9	2.4
L4, $y = 0.02$	2.2	2.9

Table 5.2. The molar percentages of $Sr_4Ru_3O_{10}$ and $SrRuO_3$ of each of the $(Sr_{1-y}La_y)_3Ru_2O_7$ batches.

5.3.2 *B || ab*

$\Delta\chi(T)$ of $y = 0$, 0.005, 0.01 and 0.02 is shown in Figure 5.1. The maximum value of $\Delta\chi$ of $Sr_3Ru_2O_7$ is 2.1×10^{-2} emu/Ru mol at $T_{max} = 16$ K. The maximum of $\Delta\chi$ of each of the La-doped samples is much smaller: 0.51, 0.49 and 0.48×10^{-2} emu/Ru mol at $T_{max} = 14$, 15 and 17 K for $y = 0.005$, 0.01 and 0.02, respectively; the uncertainty of

these T_{max} values is $\pm$ 0.5 K. Therefore, in contrast to the behaviour of the small-x samples of $Sr_3(Ru_{1-x}Ti_x)_2O_7$, T_{max} of these La-doped materials does *not* vary monotonically with doping: T_{max} of y = 0.005 is smaller than T_{max} of the other materials.
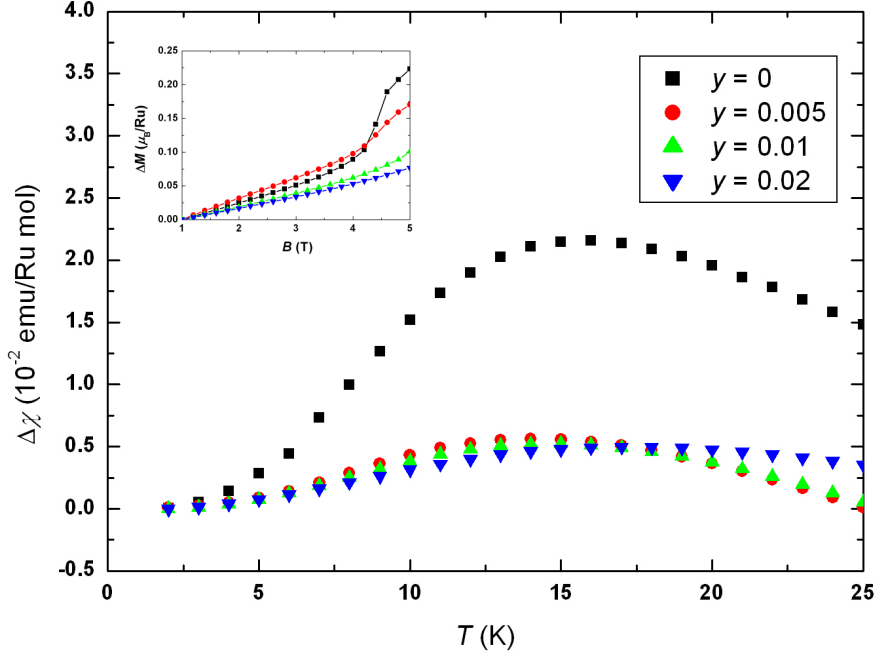

Figure 5.1. $\Delta\chi(T)$ **of** y **= 0, 0.005, 0.01 and 0.02. The inset shows** ΔM**(B) of these materials at** T **= 2 K.**

The inset to Figure 5.1 shows $\Delta M(B)$ of $Sr_3Ru_2O_7$ and each of the La-doped samples. The low-field slope of $\Delta M(B)$ also varies non-monotonically with y: this slope is 0.025, 0.032, 0.019 and 0.017 μ_B/RuT^{-1} for y = 0, 0.005, 0.01 and 0.02, respectively. In addition to the metamagnetism of $Sr_3Ru_2O_7$ a super-linear rise in $\Delta M(B)$ of y = 0.005 is seen in the field range between 4 and 5 T, with B_M = 4.6 $\pm$ 0.1 T. This field is slightly larger than B_M = 4.4 $\pm$ 0.1 T of $Sr_3Ru_2O_7$. At fields above approximately 4 T $\Delta M(B)$ of y = 0.01 also rises above the trend of the low-field, linear $\Delta M(B)$. However, B_M of y = 0.01 cannot be deduced because the entire rise in magnetisation is not seen within the 5 Tesla field range. No super-linear rise is seen in $\Delta M(B)$ of y = 0.02 in the field range up to 5 Tesla. Overall, it seems that the metamagnetic field is enhanced (monotonically) as a function of y; this trend has been confirmed by magnetoresistance measurements made with higher magnetic fields (section 5.6.1).

5.3.3 *B* || *c*

Figure 5.2 shows $\Delta\chi(T)$ of each material with B parallel to the crystalline c-axis. T_{max} = 16.5, 15, 18 and 19.5 K for y = 0, 0.005, 0.01 and 0.02, respectively. The maximum value of $\Delta\chi$ of y = 0, 0.005, 0.01 and 0.02 is 7.0, 2.0, 3.8 and 4.2 × 10^{-3} emu/Ru mol, respectively.
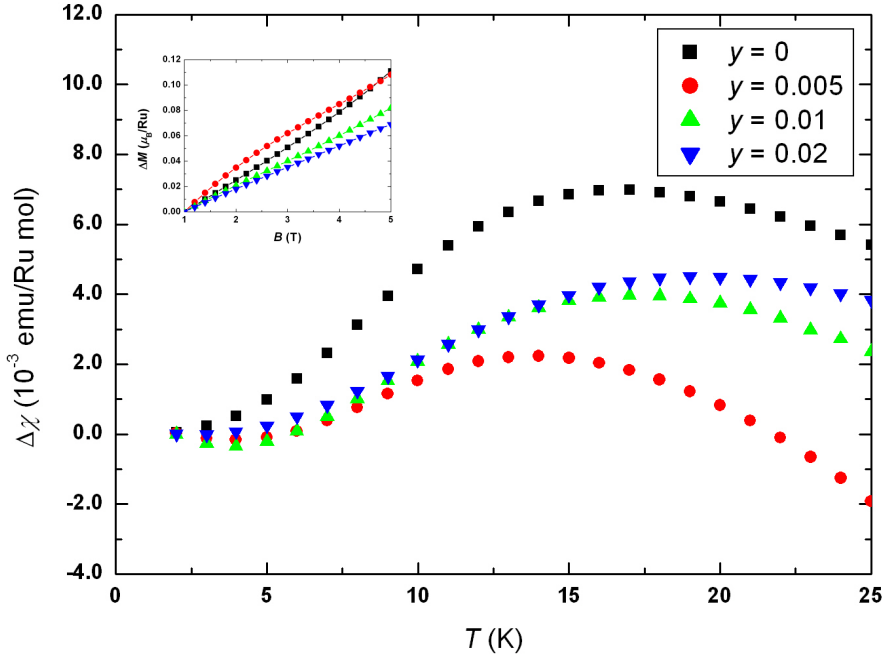

Figure 5.2. $\Delta\chi(T)$ of y = 0, 0.005, 0.01 and 0.02. The inset shows $\Delta M(B)$ of y = 0, 0.005, 0.01 and 0.02 at T = 2 K.

Displayed in the inset to Figure 5.2 is $\Delta M(B)$ of $Sr_3Ru_2O_7$ and each of the La-doped samples with T = 2 K. The low-field slope of $\Delta M(B)$ of y = 0, 0.005, 0.01 and 0.02 is 0.025, 0.034, 0.021 and 0.018 μ_B/RuT^{-1}, respectively. These values are quite similar to the low-field slope of $\Delta M(B \parallel ab)$ of each sample, referred to in the previous section. The similarity of the ab-plane and c-axis susceptibilities implies that the susceptibility of these materials is Pauli-like. Overall, both T_{max} and the low-field slope of $\Delta M(B)$ vary non-monotonically with La-doping: y = 0.005 has the smallest T_{max} and the largest value of d(ΔM)/dB. These observations are in qualitatively similar to the y-dependence of both T_{max} and d(ΔM)/dB measured with $B \parallel ab$ in section 5.3.2.

5.3.4 The Influence of Intergrowths on $\Delta\chi(T)$

The purpose of this section is to deduce to what extent the measured $\Delta\chi(T)$ are representative of the intrinsic $\chi(T)$ of the La-doped materials. Shown in Figure 5.3 is $\Delta\chi(T_{max})$ of $y = 0.005$, 0.01 and 0.02 as a function of the total molar percentage of $SrRuO_3$ and $Sr_4Ru_3O_{10}$ in each material. There is no clear correlation between $\Delta\chi(T_{max})$ and the total ferromagnetic intergrowth percentage in these La-doped materials. The intergrowth percentage does not vary monotonically with doping – the largest percentage of ferromagnetic intergrowths occurs in the $y = 0.01$ material. For $B \parallel c$ the relationship between $\Delta\chi(T_{max})$ and y is non-monotonic (Figure 5.2): the data in Figure 5.3 seem to lend some support to this relationship because there is no apparent correlation between $\Delta\chi(T_{max})$ and the total percentage of ferromagnetic intergrowths. However, absolute values of $\Delta\chi(T_{max})$ must be treated with caution, simply because it is difficult to de-convolute the intrinsic and intergrowth contributions to the magnetisation.
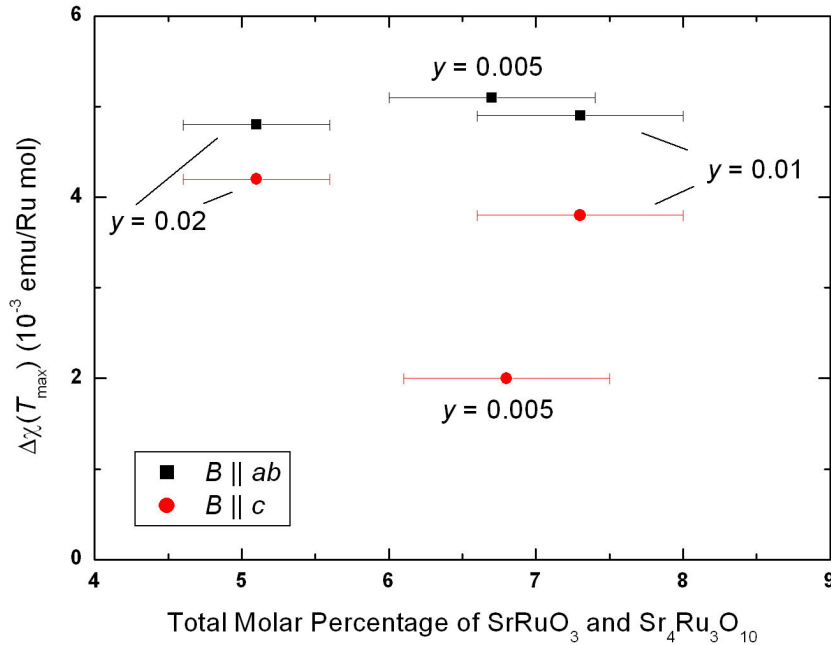

Figure 5.3. $\Delta\chi(T_{max})$ as a function of the total molar percentage of $SrRuO_3$ and $Sr_4Ru_3O_{10}$ intergrowths.

5.4 Heat Capacity

C/T of each material as function of temperature squared is shown in Figure 5.4. For temperatures greater than approximately 15 K C/T of each sample is proportional to T^2, with β = 0.202, 0.237, 0.264 and 0.224 mJ/Ru mol K^4 for y = 0, 0.005, 0.01 and 0.02, respectively. The inset to Figure 5.4 shows C_{el}/T of each sample at low temperatures. No upturn is seen in C_{el}/T of any of these samples at low temperatures and the data can be extrapolated to T = 0 K, so that the Sommerfeld coefficient of each material can be deduced. γ = 111, 92, 81 and 76 mJ/Ru mol K^2 for y = 0, 0.005, 0.01 and 0.02, respectively.
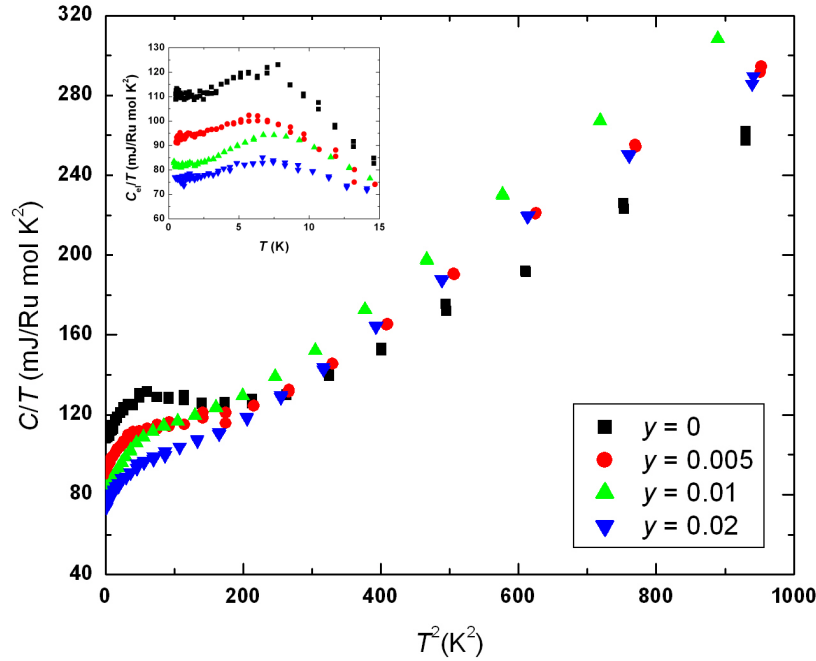
Figure 5.4. C/T of y = 0, 0.005, 0.01 and 0.02 as a function of temperature squared. The inset displays C_{el}/T of each material as a function of temperature.

The Sommerfeld coefficient of both SrRuO$_3$ and Sr$_4$Ru$_3$O$_{10}$ is approximately 30mJ/Ru mol K^2 [6,7] much lower than γ of Sr$_3$Ru$_2$O$_7$: the intrinsic Sommerfeld coefficient of the La-doped Sr$_3$Ru$_2$O$_7$ samples referred to here may, in principle, be reduced in value by SrRuO3 and Sr$_4$Ru$_3$O$_{10}$ intergrowth phases. If the heat capacity of these intergrowth phases —the molar percentages of which are estimated in section 5.3.1— is assumed to add in series to the intrinsic heat capacity and if a Sommerfeld

coefficient of 30mJ/Ru mol K^2 is assumed for both of these intergrowth phases, the corrected γ coefficients of y = 0.005, 0.01 and 0.02 are 97, 85 and 78 mJ/Ru mol K^2, respectively. Overall, the clear trend between y and γ is *not* disturbed by accounting for the $SrRuO_3$ and $Sr_4Ru_3O_{10}$ intergrowth phases: γ decreases steadily with increasing y.

5.5 Resistivity as a Function of Temperature

$\rho_{ab}(T)$ of y = 0, 0.005, 0.01 and 0.02 between 300 and 0.1 K is shown in Figure 5.5. Each $\rho_{ab}(T)$ is proportional to T at high temperatures and it is also clear that the residual resistivity of each material is relatively low.
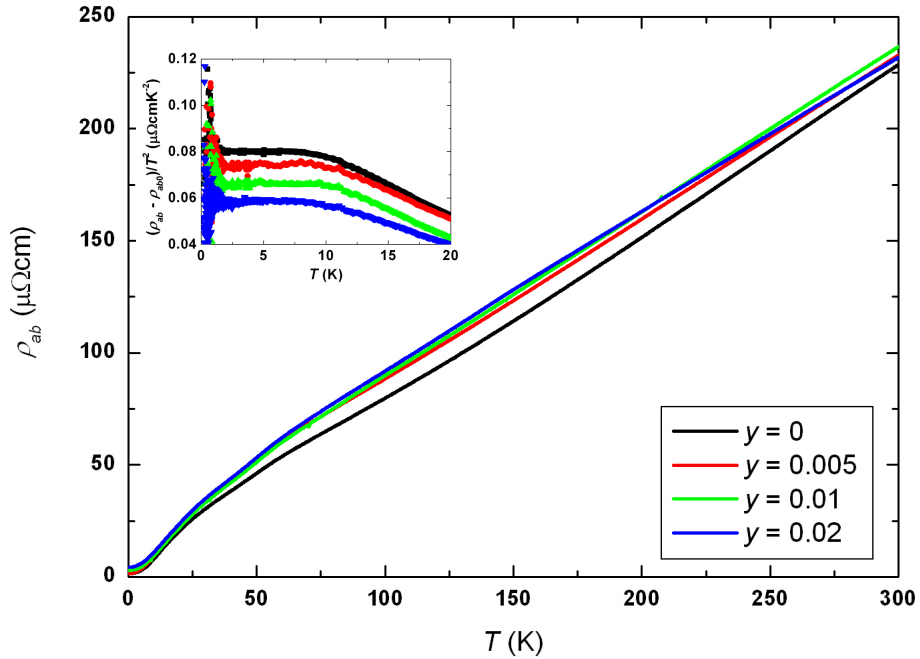
Figure 5.5. $\rho_{ab}(T)$ of y = 0, 0.005, 0.01, 0.02. (ρ_{ab} - ρ_{ab0})/T^2 of each material as a function of temperature is displayed in the inset.

The inset to Figure 5.5 shows (ρ_{ab} - ρ_{ab0})/T^2 of each material at low temperatures. The Fermi liquid A coefficient —the value of (ρ_{ab} - ρ_{ab0})/T^2 at T = 0— decreases from 0.08 $\mu\Omega$cmK^{-2} in $Sr_3Ru_2O_7$ to 0.074, 0.066 and 0.059 $\mu\Omega$cmK^{-2} for y = 0.005, 0.01 and 0.02, respectively. This decrease in A as a function of cation doping is in contrast to the *increase* in A as a function of doping seen in samples of both Ti- and

Cr-doped $Sr_3Ru_2O_7$. ρ_{ab0} = 1.1 ± 0.1, 1.8 ± 0.2, 2.9 ± 0.3 and 4.4 ± 0.4 μΩcm for y = 0, 0.005, 0.01 and 0.02, respectively: $d\rho_{ab0}/dy$ therefore approximately 170 μΩcm/y. This rate of change of residual in-plane resistivity with La-doping is, as expected for an out-of-plane dopant, much less than the enhancement of ρ_{ab0} per dopant ion in the $Sr_3(Ru_{1-x}Ti_x)_2O_7$ and $Sr_3(Ru_{1-x}Cr_x)_2O_7$ series.

5.6 Magnetoresistance

Magnetisation measurements as a function of magnetic field in section 5.3.2 hinted that the metamagnetic field of $Sr_3Ru_2O_7$ is shifted to higher fields as a function of La-doping. Fields up to 15 Tesla have been available in a dilution refrigerator and, therefore, the metamagnetism of $(Sr_{1-y}La_y)_3Ru_2O_7$ has been explored by magnetoresistance measurements made at T = 100 mK.

5.6.1 Angular Study at T = 100 mK

5.6.1.1 The Variation of $B_M(\theta)$ with y

$\rho_{ab}(B)$ at T = 100 mK of y = 0, 0.005, 0.01 and 0.02 is shown in Figures 5.6 – 5.9. These measurements were made with the magnetic field swept at a rate of 0.1 T/min. θ = 0° corresponds to $B \parallel c$-axis and the current and the field are configured so that $B \parallel I$ when θ = 90°. The uncertainty associated with the B_M values of each of these La-doped materials is relatively small: the metamagnetic features in each $\rho_{ab}(B)$ are distinctive and B_M is assumed to be the field value at which $d\rho/dB$ is a maximum. This situation is in contrast to the magnetoresistance of samples of Ti- and Cr-doped $Sr_3Ru_2O_7$ shown in sections 3.6 and 4.6; the metamagnetic field value relevant to these materials cannot be deduced unequivocally because $\rho_{ab}(B)$ is 'smeared out' in field. A knowledge of an exact, unambiguous value of each B_M is *essential* for some of the analysis referred to later in this chapter, the conclusions of which imply that Yamada theory does not account for all aspects of the metamagnetism of $(Sr_{1-y}La_y)_3Ru_2O_7$. It is emphasised here that the relatively low disorder of these La-doped materials is crucial to the results of the magnetoresistance studies described in this section and in section 5.6.2.
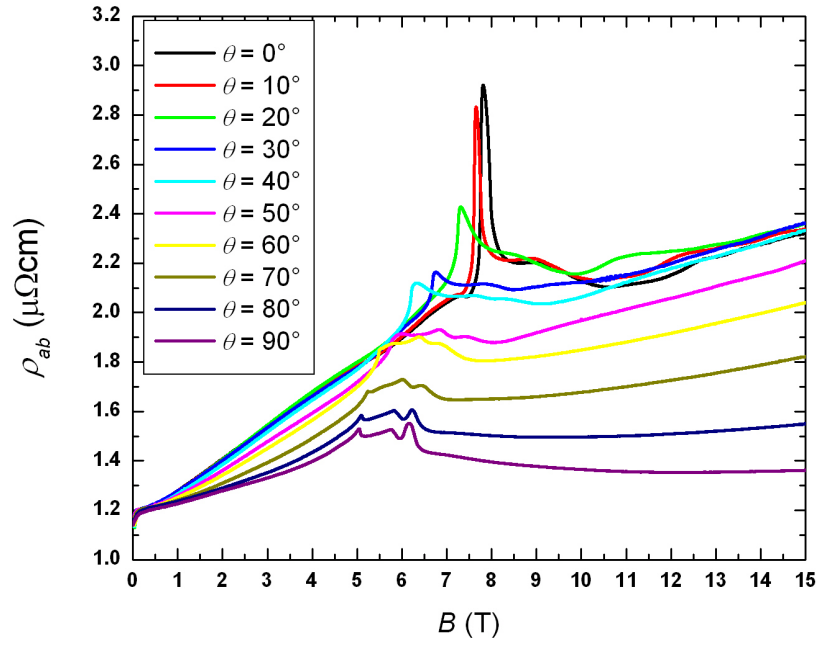
Figure 5.6. $\rho_{ab}(B)$ of $y = 0$ at $T = 100$ mK.
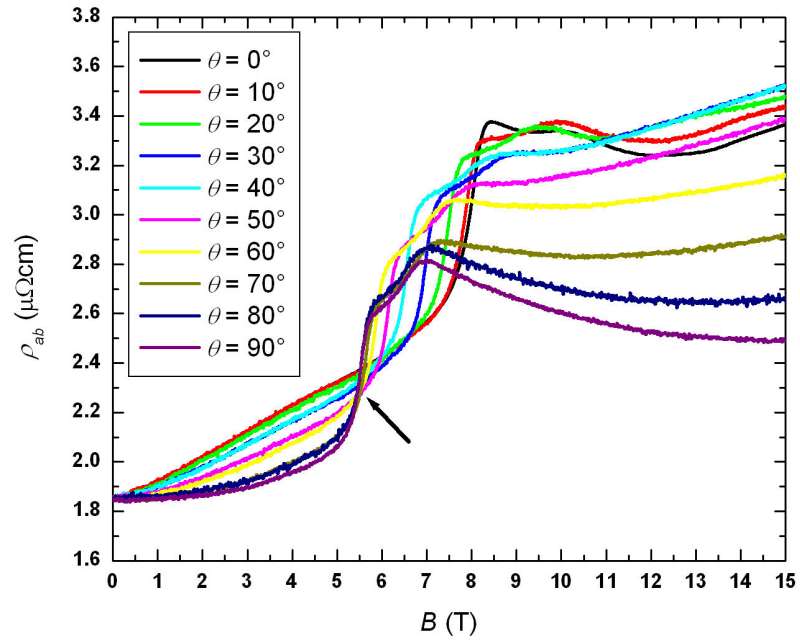
Figure 5.7. $\rho_{ab}(B)$ of $y = 0.005$ at $T = 100$ mK.
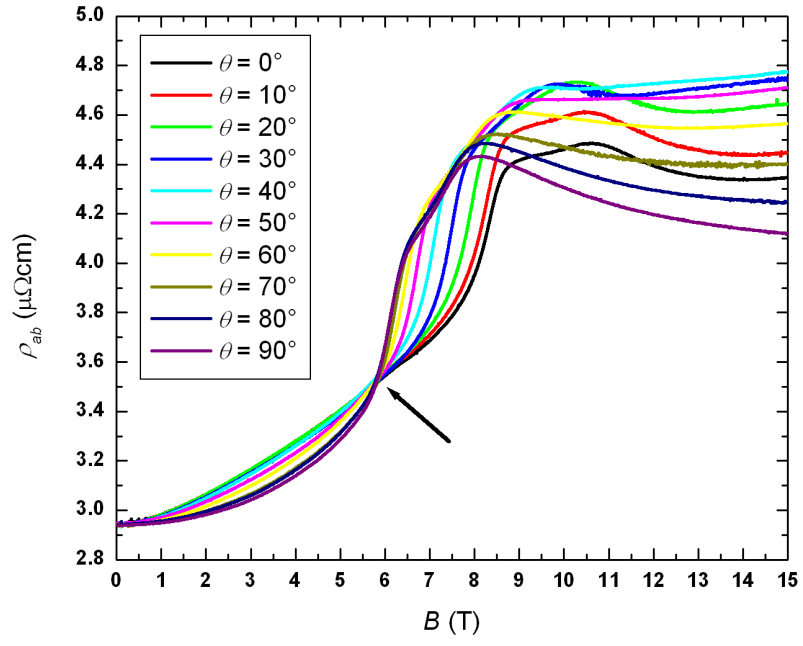
Figure 5.8. $\rho_{ab}(B)$ of $y = 0.01$ at $T = 100$ mK.

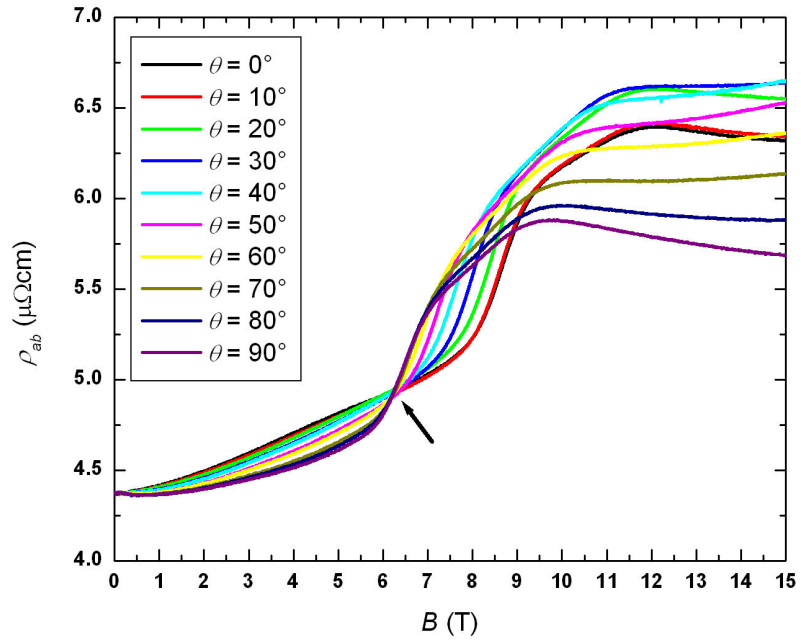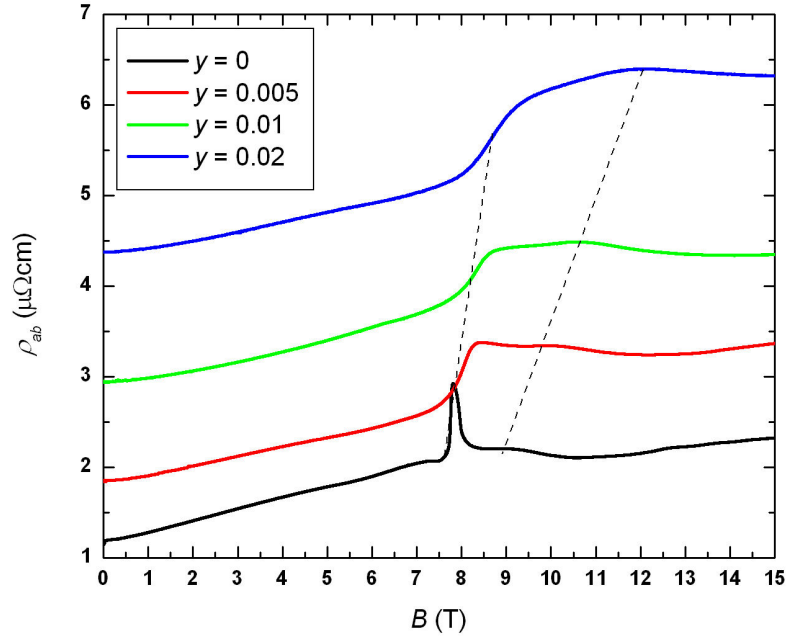**Figure 5.9.** $\rho_{ab}(B)$ of $y = 0.02$ at $T = 100$ mK.

Figure 5.10. $\rho_{ab}(B)$ of $y = 0$, 0.005, 0.01 and 0.02 at $T = 100$ mK with $\theta = 0°$. The dashed lines are a guide to the eye.
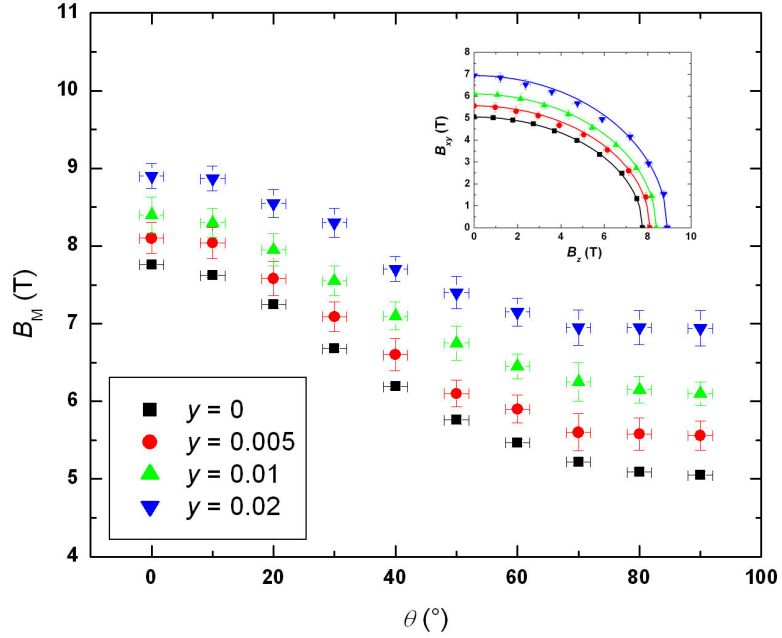

Figure 5.11. The variation with θ of B_M of $y = 0$, 0.005, 0.01 and 0.02. B_{xy} is plotted against B_z in the inset; the elliptical fit to each data arises from Equation 5.1.

It is clear in Figures 5.6 and 5.7 that, for each θ, the metamagnetic features of $y =$ 0.005 are shifted to higher fields than in Sr$_3$Ru$_2$O$_7$. For example, when $\theta = 90°$ the main metamagnetic feature in $\rho_{ab}(B)$ of $y = 0.005$ is centred at approximately 5.5 T and there is a further peak in $\rho_{ab}(B)$ at 6.9 T. For Sr$_3$Ru$_2$O$_7$ the corresponding values are 5.1 T for the primary metamagnetic field and 5.8 T for the secondary peak in $\rho_{ab}(B)$. The features associated with the metamagnetic features are shifted to even higher field values in the $y = 0.01$ and 0.02 samples, shown in Figures 5.8 and 5.9, respectively. Also, indicated with an arrow in Figures 5.7, 5.8 and 5.9 is a possible 'crossing point' (B^*, ρ^*) at which $\rho_{ab}(B = B^*)$ seems to be independent of θ. These crossing points are explored in more detail in section 5.6.1.2.

Figure 5.10 shows $\rho_{ab}(B)$ of $y = 0$, 0.005, 0.01 and 0.02 when $\theta = 0°$. The primary metamagnetic feature is shifted from 7.8 T for Sr$_3$Ru$_2$O$_7$ to 8.1, 8.4 and 8.8 Tesla for y = 0.005, 0.01 and 0.02, respectively. A weaker feature in $\rho_{ab}(B)$ of Sr$_3$Ru$_2$O$_7$ at $B =$ 9.2 T is shifted to fields of 10.4, 11.0 and 11.9 T in the $y = 0.005$, 0.01 and 0.02 samples, respectively. A feature similar to the sharp peak in $\rho_{ab}(B)$ of Sr$_3$Ru$_2$O$_7$ is not observed in the magnetoresistance of any of the La-doped materials. It is important to note that a peak in $\rho_{ab}(B)$ of Sr$_3$Ru$_2$O$_7$ (albeit a less sharp one than in Figure 5.10) *has* previously been observed in undoped samples with a residual in-plane resistivity comparable to ρ_{ab0} of $y = 0.005$. In other words, the suppression of the sharp peak in $\rho_{ab}(B)$ of Sr$_3$Ru$_2$O$_7$ as a function of La-doping in Figure 5.10 is not *only* due to increasing disorder, but can also be attributed to the intrinsic effects of electron doping. The strong influence of electron doping has also been confirmed by separate measurements of the AC susceptibility of a $y = 0.002$ sample ($\rho_{ab0} = 1.1$ μΩcm) by Dr Robin Perry [8].

The variation with θ of B_M of all of the samples has been deduced from Figures 5.6 – 5.9 and is shown in Figure 5.11. Overall, the angular dependence of the metamagnetic field of each material follows a single mathematical function. The angular dependence of B_M can be expressed in terms of the in-plane and out-of-plane components of the metamagnetic field vector, B_{xy} ($\equiv B_\mathrm{M}\sin\theta$) and B_z ($\equiv B_\mathrm{M}\cos\theta$), respectively. These quantities are plotted against each other in the inset to Figure 5.11. For each y, the data fit very well to an ellipse with semi-major and semi-minor axes equal to B_z and B_{xy}, respectively. The equation of such an ellipse is

$$\frac{B_z^2}{B_c^2} + \frac{B_{xy}^2}{B_{ab}^2} = 1 .$$ (5.1)

This can also be expressed as

$$\frac{B_M^2 \cos^2 \theta}{B_c^2} + \frac{B_M^2 \sin^2 \theta}{B_{ab}^2} = 1 .$$ (5.2)

The angular variation of B_M of each material is therefore

$$B_M(\theta) = \left(\frac{B_c^2 B_{ab}^2}{B_c^2 \cos^2 \theta + B_{ab}^2 \sin^2 \theta} \right)^{1/2} .$$ (5.3)

The anisotropy of the metamagnetism may be expressed in terms of the eccentricity, e, of each ellipse in Figure 5.11:

$$e = \left(1 - \frac{B_c^2}{B_{ab}^2} \right)^{1/2} .$$ (5.4)

e decreases from 0.76 ± 0.02 for $Sr_3Ru_2O_7$ to 0.72 ± 0.03, 0.69 ± 0.03 and 0.63 ± 0.04 for $y = 0.005$, 0.01 and 0.02, respectively. This decrease in e implies that the metamagnetism becomes less anisotropic as a function of y. It should be recalled that, for the small lanthanum concentrations considered in this work, the *crystal* structure of $Sr_3Ru_2O_7$ does not become less anisotropic as a function of La-doping (section 5.2.1).

5.6.1.2 'Crossing Points' in the (B, ρ_{ab}) Plane

Marked with an arrow in Figures 5.7, 5.8 and 5.9 is a region of the (B, ρ) plane at which a 'crossing point' seems to occur: a point (B^*, ρ^*) in the plot at which many of the data seem to coincide. In Figure 5.7 only those data for which $\theta \geq 50°$ coincide at the proposed crossing point. By contrast, the proposed crossing points in Figures 5.8 and 5.9 are very distinctive – most, if not all, of the data seem to coincide at (B^*, ρ^*).

$(B^*, \rho^*) = (5.42 \text{ T}, 2.21 \text{ μΩcm})$, $(5.82 \text{ T}, 3.51 \text{ μΩcm})$ and $(6.25 \text{ T}, 4.85 \text{ μΩcm})$ for $y = 0.005$, 0.01 and 0.02, respectively. ρ^* is plotted against B^* in the top inset to Figure 5.12. These two quantities are related linearly: $\rho^* = 3.18B^* - 15.02$, with the field and resistivity expressed in units of Tesla and μΩcm, respectively. This linear relationship, however, is likely to be coincidental because resistivity is a sample

121

dependent quantity. It is more appropriate to look for a relationship between B^* and the angle-dependent metamagnetic field. Shown in the main part of Figure 5.12 for y = 0.005, 0.01 and 0.02 is a plot of B^* against B_{ab}, the value of B_M when $\theta = 90°$. There is also a linear relationship between these two quantities:

$$B^* = 0.593B_{ab} + 2.149. \tag{5.5}$$

It is clear that, for $y = 0.005$, 0.01 and 0.02, B^* is smaller than B_{ab}.
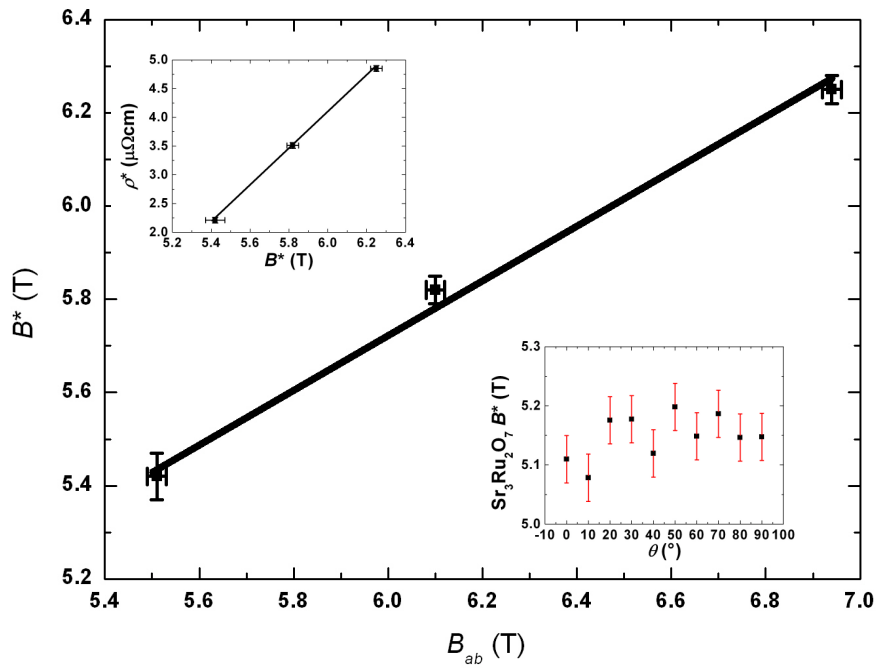
Figure 5.12. B^* **of** y **= 0.005, 0.01 and 0.02 plotted against** B_{ab}**. The top inset displays** ρ^* **against** B^* **for the same samples. The lower inset displays** $B^*(\theta)$ **of** $Sr_3Ru_2O_7$**, extrapolated from the** y **= 0.005, 0.01 and 0.02 data.**

There is no crossing point in the $Sr_3Ru_2O_7$ (B, ρ) plot (Figure 5.6). A putative B^* for $Sr_3Ru_2O_7$ can, however, be deduced from Equation 5.5 – when $\theta = 90°$, $B^* = 5.14$ T. Moreover, for the crossing points of $y = 0.005$, 0.01 and 0.02 a good fit for *each* θ between 0 and 90° is

$$B^*(y) = X(\theta)B_M(\theta, y) + Z(\theta), \tag{5.6}$$

where X and Z are the slope and intercept found when, for a given θ, $B^*(y)$ is plotted against $B_M(y)$. The lower inset to Figure 5.12 shows $B^*(\theta)$ found when $B_M(\theta, y = 0)$ is substituted into Equation 5.6. To a good approximation $B^*(y = 0)$ is independent of θ across the entire angular range. It is also clear that this B^* is slightly *larger* than B_{ab} which, for $Sr_3Ru_2O_7$ at $T = 100$ mK, is 5.05 T. This is in contrast to B^* of the La-doped materials, each of which is smaller than B_{ab}. Overall, the existence of the crossing points in the (B, ρ) plots is apparently correlated with a relationship between B^* and B_{ab}. For $y = 0.005$, 0.01 and 0.02, B^* is slightly *smaller* than B_{ab}. On the other hand, no crossing point in the (B, ρ) plot of $Sr_3Ru_2O_7$ is observed but the predicted B^* of $Sr_3Ru_2O_7$ is *greater* than B_{ab}.

5.6.2 The Influence of Higher Temperatures

It was also desirable to investigate how $\rho_{ab}(B)$ varies with temperature and, therefore, to investigate the dependence of B_M on temperature. B_{ab} of each of the La-doped materials was within the 7.5 Tesla field range available in the ADR and, hence, measurements of $\rho_{ab}(B)$ with $B \parallel I \parallel ab$ have been made. Figure 5.13 displays $\rho_{ab}(B)$ of $y = 0.01$ at $T = 300$, 600 and 1200 mK. The rise in resistivity associated with the metamagnetism is not broadened in field range significantly as temperature is raised from 300 mK to 1200 mK.

The inset to Figure 5.13 shows the derivative of $\rho_{ab}(B)$ with respect to field in the vicinity of the metamagnetic feature. The peak in $d\rho/dB$ (at $B = B_M$) is shifted from 5.87 ± 0.01 T at $T = 300$ mK to 5.85 ± 0.01 and 5.79 ± 0.01 T at 600 mK and 1200 mK, respectively: dB_M/dT is clearly negative over this temperature range. Qualitatively similar temperature-dependence of $\rho_{ab}(B)$ (little broadening) and the peak in $d\rho/dB$ (negative dB_M/dT) has also been observed for $y = 0.005$ and 0.02. A similar analysis of the temperature dependence of B_M of the Ti- and Cr-doped samples was not made in chapters 3 and 4 because the magnetoresistance of these materials was 'smeared out' in field and the exact value of B_M was unclear.
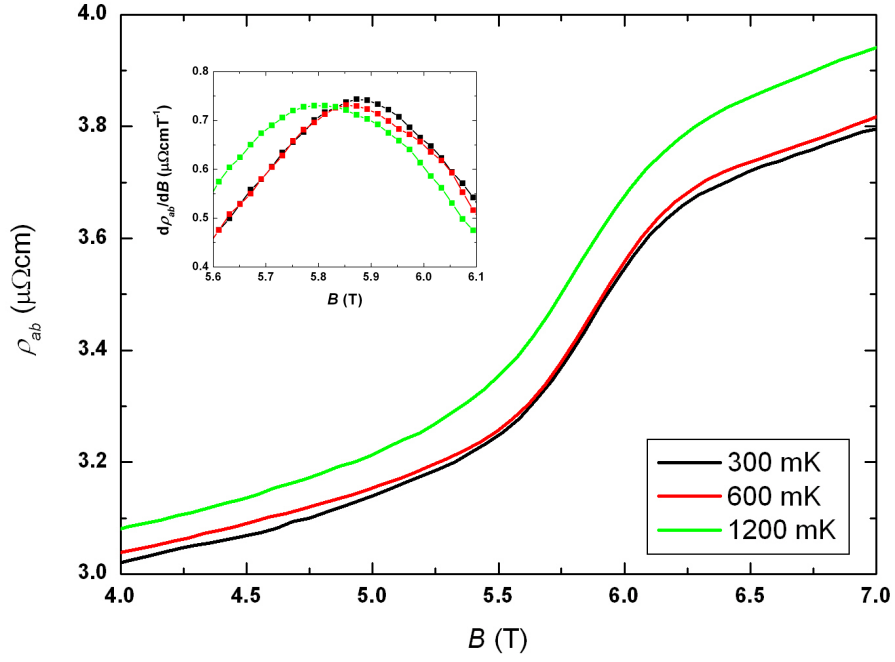
Figure 5.13. $\rho_{ab}(B)$ **of** $y = 0.01$**, measured with** $B \parallel I \parallel ab$**.** $d\rho/dB$ **in the vicinity of** B_M **is displayed in the inset.**

5.7 Discussion

The main observations reported in this chapter are:

- The Fermi liquid A coefficient (Figure 5.5) and the Sommerfeld coefficient of the electronic heat capacity (Figure 5.4) decrease steadily as a function of lanthanum substitution into $Sr_3Ru_2O_7$.

- The metamagnetic field *increases* steadily as a function of La-doping (Figure 5.10).

- The metamagnetic field of the La-doped materials decreases as temperature is raised (Figure 5.13).

- Both the Pauli susceptibility and T_{max}, the temperature at which the magnetic susceptibility peaks, vary non-monotonically with lanthanum concentration.

The decreases in both γ and A imply that the mass of some, or possibly all, of the

Landau quasiparticles decreases as a function of La-doping. Equations 1.2 and 1.5 imply that γ and A are expected to be proportional to $m*$ and $(m*)^2$, respectively, so that A/γ^2 of a Fermi liquid should be a constant, known as the *Kadowaki-Woods ratio* (KWR). However, these two equations are only valid for a single-band, isotropic Fermi surface. Hussey [9] provides a detailed discussion of the Kadowaki-Woods ratio in the context of real, correlated metallic oxides; it is shown that the KWR depends on unit cell volume, dimensionality, carrier density and also the number of bands in the Brillouin zone.
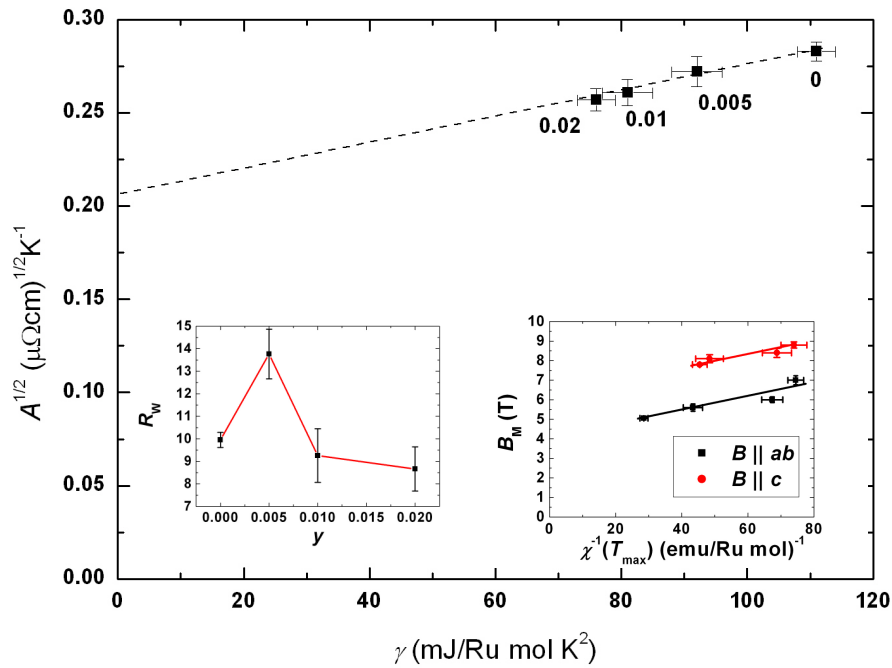
Figure 5.14. γ of y = 0, 0.005, 0.01 and 0.02 as a function of $A^{1/2}$. The left inset displays R_W as a function of y; the line is a guide to the eye. The right inset shows B_M plotted against the inverse of the estimated value of $\chi(T_{max})$ for $B \parallel ab$ and $B \parallel c$.

Figure 5.14 shows the square root of A of each material plotted against γ. These two quantities are related by a linear fit, but the linear trendline does not pass through the origin. However, the KWR is known to be sensitive to carrier density, n, and A/γ^2 is expected to be proportional to k_F^{-3} in two-dimensional Fermi liquids. If lanthanum substitution is assumed to 'electron-dope' the ground state of $Sr_3Ru_2O_7$, k_F should increase as a function of y. It is therefore unsurprising that the trendline in Figure 5.14

does not pass through the origin because the simplest form of the KWR does not account for changes in k_F. Hussey shows a qualitatively similar plot to Figure 5.14 for the $La_{1-x}Sr_xTiO_3$ series, for which k_F also varies with carrier doping, x. Overall, the data in the main part of Figure 5.14 do not imply that the theory associated with the KWR is invalid for the $(Sr_{1-y}La_y)_3Ru_2O_7$ series, but *do* clearly indicate a reduction in the thermodynamic mass, $m*$, of some, if not all, of the Landau quasiparticles as a function of y.

y	χ_P (10^{-2} emu/Ru mol)	γ (mJ/Ru mol K^2)	R_W	F_0^a
0	1.50 ± 0.03	111 ± 3	9.9 ± 0.3	-0.898 ± 0.003
0.005	1.77 ± 0.13	92 ± 3	13.8 ± 1.1	-0.927 ± 0.006
0.01	1.05 ± 0.13	81 ± 3	9.3 ± 1.2	-0.892 ± 0.014
0.02	0.91 ± 0.10	76 ± 3	8.7 ± 1.0	-0.885 ± 0.013

Table 5.3. The Pauli susceptibility, Sommerfeld coefficient, Wilson ratio and F_0^a factor of each member of the $(Sr_{1-y}La_y)_3Ru_2O_7$ series.

Equation 1.3 indicates that the paramagnetic susceptibility of a Fermi liquid is renormalised by the $m*$ term *and* the phenomenological $(1+F_0^a)$ factor. Therefore, because $m*$ seems to decrease monotonically with y, any non-monotonic variation of χ with doping must be accounted for by this latter factor. Listed in Table 5.3 is the Pauli susceptibility, the Sommerfeld coefficient, the Wilson ratio and the phenomenological F_0^a factor of $y = 0$, 0.005, 0.01 and 0.02. The Pauli susceptibility of each material has been estimated from the insets to Figures 5.1 and 5.2 and Equation 3.4 has been used to take account of the influence of $SrRuO_3$ and $Sr_4Ru_3O_{10}$ intergrowths on the measured susceptibility. Regarding the Sommerfeld coefficient, account has also been taken of the relatively small electronic heat capacity of these intergrowth phases. All corrections to the susceptibilities and the Sommerfeld coefficients are incorporated within the error bars of the χ_P and γ values listed in Table 5.3. The Wilson ratio is plotted against y in the left inset to Figure 5.14. R_W of $y = 0.005$ is significantly larger than R_W of the other materials. However, a single datum is insufficient evidence for a true peak in $R_W(y)$.

The large Wilson ratio of $y = 0.005$ is concomitant with the relatively large Pauli susceptibility of this material. However, the susceptibility values were estimated from $\Delta M(B)$ data and their reliability must be challenged. As discussed in section 1.2.4.3, in Yamada's theory of itinerant metamagnetism [10,11] T_{max} is proportional to $a|b|/c$ and, hence, inversely proportional to the Pauli susceptibility. It was shown in sections 5.3.2 and 5.3.3 that, for $B \parallel ab$ and $B \parallel c$, T_{max} of $y = 0.005$ *was* smaller than T_{max} of the other materials. It was also argued in section 3.3.2.3 that T_{max} is unlikely to change as a result of magnetic contributions from $SrRuO_3$ and $Sr_4Ru_3O_{10}$ intergrowths. Therefore, the relatively small T_{max} values of $y = 0.005$ lend support to the large (estimated) Pauli susceptibility of this material.

The simplest view of itinerant electron metamagnetism involves the chemical potential of a one-electron band being shifted by an external magnetic field through a peak in $g(E)$. Tuning through a peak in $g(E)$ was achieved by La-doping in the $Sr_{2-y}La_yRuO_4$ series. However, it is unlikely that the lanthanum doping in the study described here tunes the Fermi level through a peak in the one-electron density of states: the Sommerfeld coefficient, predicted to be proportional to $g(E)$, *decreases* steadily with y. On the other hand, a larger Sommerfeld coefficient induced by other lanthanum concentrations cannot be ruled out, either at concentrations greater than or intermediate between the concentrations referred to in this work. However, in the context of a rigid band-shift it may be expected that $k_B T_{max} \approx \mu_B B_M$. This relationship is *not* satisfied in the series of La-doped crystals studied here: T_{max} varies non-monotonically with y while B_M is enhanced monotonically as a function of y.

A relationship between B_M and $\chi^{-1}(T_{max})$ in the context of the Yamada theory [11] is given in Equation 1.9. Displayed in the right inset to Figure 5.14 is B_M as a function of $\chi^{-1}(T_{max})$, for $B \parallel ab$ and $B \parallel c$. For each field orientation a linear relationship between the two quantities is clear, with a slope of 0.059 ± 0.006 and 0.048 ± 0.005 μ_B/Ru for the ab-plane and the c-axis, respectively. If these trendlines are extrapolated to $\chi^{-1}(T_{max}) = 0$, B_M is predicted to be nonzero. This observation is in sharp contrast to the behaviour of the metamagnetism of the cobalt and uranium compounds reported by Yamada and Goto: for these materials $B_M \rightarrow 0$ at some positive value of $\chi^{-1}(T_{max})$; in other words, the B_M-axis intercept of the plot of $(B_M, \chi^{-1}(T_{max})$ of these materials is

negative (this is clear in ref. 11). Therefore, the positive B_M-axis intercepts predicted in the inset to Figure 5.14 indicate that the metamagnetism of the $(Sr_{1-y}La_y)_3Ru_2O_7$ series is not fully accounted for by the theory in refs. 10 and 11.

Three of the predictions of the spin fluctuation extension to the Ginzburg-Landau theory of uniform magnetisation are: (1) T_{max} is proportional to $a|b|/c$; (2) B_M increases as a function of increasing temperature and; (3) a linear relationship exists between B_M and $\chi^{-1}(T_{max})$, with $B_M = 0$ (i.e. a ferromagnetic state) occurring at some finite value of susceptibility. The results reported in this chapter are only in partial agreement with these theoretical predictions. It has been found that T_{max} of these La-doped materials *is* correlated with the Pauli susceptibility, with the smallest T_{max} occurring for $y = 0.005$, the Pauli susceptibility of which is larger than χ_P of the other materials. However, some observations reported here are not consistent with Yamada theory. In particular, the metamagnetic field of these La-doped materials *decreases* as temperature is raised – qualitatively similar behaviour to this has also been observed for undoped $Sr_3Ru_2O_7$ [12]. Furthermore, B_M, which *does* have a linear correlation with $\chi^{-1}(T_{max})$, is predicted to remain finite when $\chi^{-1}(T_{max}) \rightarrow 0$: in other words, metamagnetism is predicted to occur even when the susceptibility (at $\mathbf{q} = 0$) diverges.

The final issue discussed here is the 'crossing points' in Figures 5.7, 5.8 and 5.9. The field at which these crossing points occur, B^*, is always less than B_{ab}. No crossing point is observed in the magnetoresistance of $Sr_3Ru_2O_7$, but a putative B^* for $Sr_3Ru_2O_7$ *has* been extrapolated from the $y = 0.005$, 0.01 and 0.02 data. This B^* is predicted to be slightly larger than B_{ab} of $Sr_3Ru_2O_7$. On the basis of these observations it seems that a crossing point can occur if $B^* < B_{ab}$ but is avoided if $B^* > B_{ab}$. However, the magnetoresistance measurements in section 5.6.1 do not shed any further light on the physical significance of B^* and no further experimental study of these crossing points has been made. Morozov *et al.* [13] report a crossing point in the *c*-axis magnetoresistance of crystals of $Bi_2Sr_2CaCu_2O_{8+\delta}$ (Bi-2212) irradiated by heavy ions. The main consequence of this irradiation is the formation of columnar defects, where the superconductivity of Bi-2212 is suppressed. Bi-2212, like $Sr_3Ru_2O_7$, is a quasi-2D material but, aside from this similarity, there is no obvious connection between the Bi-2212 crossing point and those shown in Figures 5.7, 5.8 and 5.9.

5.8 References

[1] G. Cao, S. C. McCall, J. E. Crow and R. P. Guertin, Phys. Rev. B **56**, 5387 (1997)

[2] N. Kikugawa, A. P. Mackenzie, C. Bergemann, R. A. Borzi, S. A. Grigera and Y. Maeno, Phys. Rev. B **70**, 060508 (2004)

[3] N. Kikugawa, A. P. Mackenzie, C. Bergemann and Y. Maeno, Phys. Rev. B **70**, 174501 (2004)

[4] N. Kikugawa, C. Bergemann, A. P. Mackenzie and Y. Maeno, Phys. Rev. B **70**, 134520 (2004)

[5] K. M. Shen, N. Kikugawa, C. Bergemann, L. Balicas, F. Baumberger, W. Meevasana, N. J. Ingle, Y. Maeno, Z.-X. Shen and A. P. Mackenzie, Phys. Rev. Lett. **99**, 187001 (2007)

[6] G. Cao, S. McCall, M. Shepard, J. E. Crow and R. P. Guertin, Phys. Rev. B **56**, 321 (1997)

[7] G. Cao, S. Chikara, J. W. Brill, P. Schlottmann, Phys. Rev. B **75**, 024429 (2007)

[8] R. S. Perry, unpublished

[9] N. E. Hussey, J. Phys. Soc. Jpn. **74**, 1107 (2005)

[10] H. Yamada, Phys. Rev. B. **47**, 11211 (1993)

[11] H. Yamada and T. Goto, Physica B **346**, 109 (2004)

[12] S. A. Grigera, R. A. Borzi, A. P. Mackenzie, S. R. Julian, R. S. Perry and Y. Maeno, Phys. Rev. B **67**, 214427 (2003)

[13] N. Morozov, L. N. Bulaevskii, M. P. Maley, J. Y. Coulter, A. E. Koshelev and T.-W. Li, Phys. Rev. B **60**, 96 (1999)

6. Summary

The aim of this work was to shed light on some of the electronic physics associated with $Sr_3Ru_2O_7$ by substituting foreign cations into the crystal lattice of this metallic ruthenate. The experimental results presented in chapters 3, 4 and 5 are the basis of a number of conclusions related to this aim. Furthermore, a number of ideas for future research have also emerged from this work.

6.1 Conclusions

The work in Chapter 3 indicates that a spin density wave emerges in the $Sr_3(Ru_{1-x}Ti_x)_2O_7$ series. Doping with a relatively small concentration of titanium cations suppresses the metamagnetic features in the magnetisation and magnetoresistance. The Sommerfeld coefficient of the heat capacity of the $x = 0.025$ and 0.05 materials was found to diverge logarithmically with temperature, hinting at critical magnetic fluctuations in these materials. For larger titanium concentrations a suppression of the Sommerfeld coefficient and an upturn in electrical resistivity imply the formation of a spin density wave, with the ordered magnetic moment aligned along (or close to) the crystalline c-axis. Neutron scattering measurements made by collaborating researchers have confirmed the presence of a spin density wave in these heavily-doped materials.

The effects of substituting a small concentration of chromium cations into $Sr_3Ru_2O_7$ are remarkable. A $1/T$ upturn in the magnetic susceptibility of the $x = 0.006$ material has associated with it an effective magnetic moment of more than 6 μ_B/Cr. It is therefore possible than an island of magnetic polarisation emerges around each Cr cation. An island of polarisation which varies smoothly in real space is expected to arise from a magnetic susceptibility which is sharply peaked in $\mathbf{q}$-space, consistent with the idea that $Sr_3Ru_2O_7$, with a low-field Wilson ratio much larger than 1, has an exchange-enhanced susceptibility. Time-dependent magnetic irreversibility in the $x = 0.02$ material has been observed in at low temperatures: this observation suggests that

the RKKY mechanism may be responsible for interactions between the aforementioned magnetic islands.

Substitution of lanthanum cations onto the strontium lattice sites of $Sr_3Ru_2O_7$ allows the electronic ground state to be 'electron-doped' while the crystalline disorder is kept relatively low. A clear reduction in the mass of some, if not all, of the Landau quasiparticles as a function of La-doping has been indicated by resistivity and heat capacity measurements. The metamagnetic field of the $(Sr_{1-y}La_y)_3Ru_2O_7$ series increases monotonically as a function of La-doping. On the other hand, it is probable that the Pauli susceptibility and T_{max} vary non-monotonically with y. These observations rule out a description of the metamagnetism of $(Sr_{1-y}La_y)_3Ru_2O_7$ by a model involving a rigid shift of a band through a peak in the electronic density of states. Also, a linear relationship between B_M and $\chi^{-1}(T_{max})$ has been found; this relationship is not, however, fully consistent with the theory of Yamada and Goto. The metamagnetic field of these La-doped materials was also observed to *decrease* as a function of increasing temperature – this observation is in contrast to the *increase* in B_M as a function of temperature predicted by theory of Yamada. Overall, it is clear that all aspects of the metamagnetism of $(Sr_{1-y}La_y)_3Ru_2O_7$ cannot be accounted for by Yamada's spin fluctuation extension to the Ginzburg-Landau theory of uniform magnetisation.

6.2 Suggestions for Future Work

An issue that has not been resolved by the work described in this thesis is how the first-order metamagnetic *phase transition* of $Sr_3Ru_2O_7$ evolves with cation doping. Magnetoresistance measurements do not indicate whether the metamagnetic features of the cation-doped materials have associated with them a phase transition or simply a crossover. Therefore, measurements of the susceptibility (AC or DC) of some of the cation-doped crystals referred to in this thesis at temperatures $O(100$ mK$)$ would be interesting.

The hypothesis of an 'island' of magnetic polarisation around each Cr cation in $Sr_3(Ru_{1-x}Cr_x)_2O_7$ ($x = 0.006$) is based upon the effective magnetic moment of more

than 6 μ_B associated with each chromium ion. The detection of such islands, if they exist in the form postulated in Chapter 4, may be possible by a technique which allows real-space variations in an electronic density of states to be measured, namely scanning tunnelling microscopy. The chromium substitution referred to in Chapter 4 is also a source of elastic scattering and, therefore, QPI effects may also be observed in STM measurements on $Sr_3(Ru_{1-x}Cr_x)_2O_7$ samples. Quasiparticle interference due to elastic scattering is *different* to RKKY-type oscillations associated with magnetic impurity ions. How these separate effects coexist or compete with each other is an important question that future STM measurements may be able to answer. In particular, *spin-polarised* scanning tunnelling microscopy on samples of these Cr-doped ruthenates may provide an insight into the coexistence of QPI and RKKY effects in a clean, narrow-band metal.

As discussed in the introduction to Chapter 4, information regarding the orbital degree of freedom in transition metal oxides can often be provided by resonant X-ray scattering measurements. The orbital state in which dopant ions exist may be a source of the significant difference in the behaviour of the $Sr_3(Ru_{1-x}Cr_x)_2O_7$ materials reported in this thesis and the $Sr_3(Ru_{1-x}Mn_x)_2O_7$ samples studied by Mathieu *et al.*, namely that Mn-doping causes a transition into an insulating state. Chromium cations can exist in perovskite TMOs as Cr^{3+} or Cr^{4+}; the e_g orbitals of these cations are nominally unoccupied. By contrast, the e_g orbitals of manganese cations *may* be occupied, but only if these cations are in the Mn^{3+} ($3d^4$) state. A comparison between RXS measurements of $Sr_3(Ru_{1-x}Mn_x)_2O_7$ and $Sr_3(Ru_{1-x}Cr_x)_2O_7$ may shed light on the role of the orbital degree of freedom in these materials.

A striking feature associated with the $(Sr_{1-y}La_y)_3Ru_2O_7$ series is the relatively large Wilson ratio of $y = 0.005$. However, a true peak in $R_w(y)$ (left inset to Figure 5.14) cannot be claimed on the basis of a single datum. Therefore, it may be desirable to investigate members of the $(Sr_{1-y}La_y)_3Ru_2O_7$ series with lanthanum concentrations intermediate between those already studied. A peak in $R_w(y)$ is likely to be inextricable with the metamagnetism of this series, aspects of which remain unresolved by the work described in Chapter 5.

Regarding further out-of-plane cation substitution, it may be possible to dope *holes* into the electronic ground state of $Sr_3Ru_2O_7$ by substituting monovalent cations, such as those of potassium or sodium, onto the strontium lattice sites of this ruthenate. Hole-doping of single crystals of Ruddlesden-Popper ruthenates has never been reported – issues associated with the incompatibility of starting chemicals may be important. A hole-doping study of $Sr_3Ru_2O_7$ would provide a helpful contrast to the electron-doping study reported in Chapter 5 of this thesis.

Another possibility for future work is an extensive investigation of the influence of cation doping on the electronic nematic phase of $Sr_3Ru_2O_7$. Signatures of this phase in magnetoresistance and susceptibility measurements are suppressed by disorder. However, an issue that is yet unresolved is how the *order parameter* of this phase couples to crystalline disorder. Carlson *et al*. (Phys. Rev. Lett. **96**, 097003 (2006)) discuss the influence that disorder has on the electronic nematicity of high-T_c superconductors. In particular they suggest that the random-field effects induced by disorder may cause certain hysteresis and noise features; these effects may be detectable in STM experiments. High-field STM studies of undoped $Sr_3Ru_2O_7$ and $Sr_3Ru_2O_7$ doped with a *very* small concentration of cations may be useful in this respect.

Appendix

The Magnetoresistance ($B \parallel ab$) of Sr$_3$Ru$_2$O$_7$

As discussed in section 1.1, two key features associated with the emergent state of electronic matter in the vicinity of the metamagnetic QCEP in Sr$_3$Ru$_2$O$_7$ are sensitivity to crystalline disorder and an in-plane magnetoresistive anisotropy. Perry *et al.* [1] studied the magnetoresistance of Sr$_3$Ru$_2$O$_7$ with an external magnetic field parallel to the crystalline *ab*-planes and also discovered a disorder- and temperature-sensitive feature in $\rho_{ab}(B)$. At $T = 110$ mK a distinctive hump in the magnetoresistance of ultrapure Sr$_3$Ru$_2$O$_7$ ($\rho_{ab0} = 0.55\mu\Omega$cm) was observed when $B_{ab} \sim$ 6 T; this feature appeared much broader when $T = 320$ mK and was not resolved at temperatures above 600 mK. Features in the DC susceptibility (dM/dB) with a similar sensitivity to temperature were also identified in the field range between 6 and 6.5 T. The unusual feature in $\rho_{ab}(B)$ in the vicinity of 6 T was not observed in a dirtier Sr$_3$Ru$_2$O$_7$ crystal ($\rho_{ab0} = 2.8 \mu\Omega$cm): this sensitivity to crystalline disorder led Perry and co-workers to speculate that this feature may be related to incipient quantum criticality.

The work described in this appendix relates to $\rho_{ab}(B)$ of crystals of Sr$_3$Ru$_2$O$_7$ with a residual resistivity intermediate between ρ_{ab0} of the two crystals studied in ref. 1. All measurements were made in a dilution refrigerator, with the external magnetic field swept at a rate of 20mT/min. Figure A1 shows $\rho_{ab}(B)$ ($B \parallel I \parallel ab$) of Sr$_3Ru_2O_7$ ($\rho_{ab0} = $ 1.15$\mu\Omega$cm) at $T = 100$, 300, 500 and 700 mK. Features in $\rho_{ab}(B)$ at fields close to 5.1 and 5.8 T correspond to the primary and secondary metamagnetic fields, B_M and B_M2, respectively. Both of these features remain quite sharp at temperatures up to 700 mK. By contrast, the peak in $\rho_{ab}(B)$ centred about 6.2 T is less distinctive at higher temperatures: the large, narrow peak seen at $T = 100$ mK is broadened in field range and suppressed in magnitude (relative to the background magnetoresistance) at $T = $

300 mK; a broad kink in $\rho_{ab}(B)$, rather than a peak, is seen at $T = 500$ mK; this kink is less distinctive at $T = 700$ mK. The sensitivity to temperature of this higher-field feature is qualitatively consistent with work in ref. 1. It is also clear from the upper inset to Figure A1 that B_M, assumed to be the low-field at which $\rho_{ab}(B)$ peaks, decreases as a function of temperature, from 5.087 T at $T = 100$ mK to 5.084 T at $T = 700$ mK.
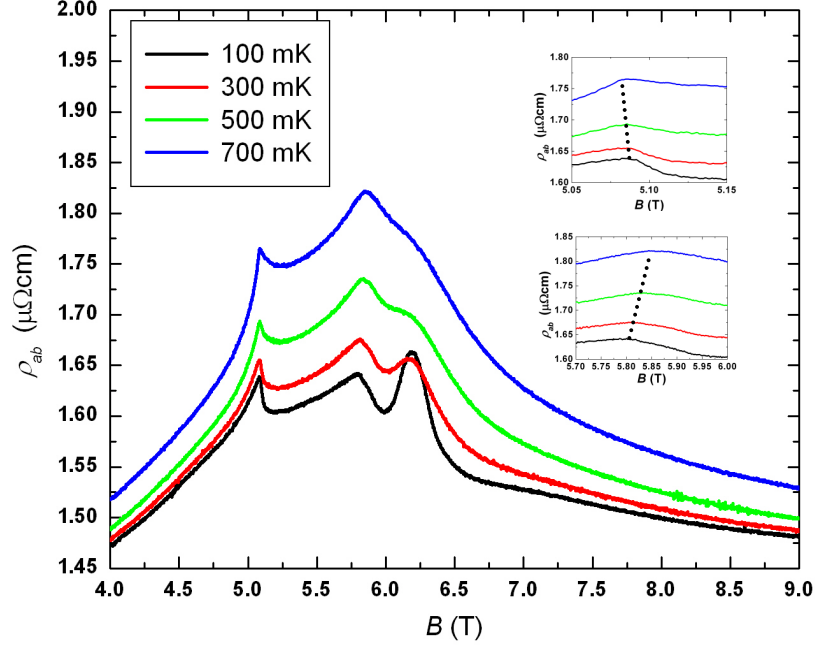

Figure A1. $\rho_{ab}(B)$ ($B \parallel I \parallel ab$) of Sr$_3Ru_2O_7$ ($\rho_{ab0} = 1.15$ μΩcm). The upper and lower insets display $\rho_{ab}(B)$ in the vicinity of B_M and B_{M2}, respectively; the dotted lines are a guide to the eye.

ΔB_M, defined as $B_M(T = 700$ mK$) - B_M(T = 100$ mK$)$, is listed for each crystal in Table A1 and also for both field-current configurations, namely $B \parallel I$ ($\rho^{\parallel}(B)$) and $B \perp I$ ($\rho^{\perp}(B)$). For $B \parallel I$ ΔB_M is equal, within errors, for each of the three crystals. By contrast, when $B \perp I$ ΔB_M is always positive and decreases sharply as a function of increasing ρ_{ab0}. However, ΔB_M is equal, within errors, for the 1.6 and 2.7 μΩcm crystals. The relatively large ΔB_M of the 1.15 μΩcm crystal cannot be ruled out as an outlying result, although there is no particular evidence to suggest this is true.

It was also desirable to investigate how ΔB_{M2} ($= B_{M2}(T = 700$ mK$) - B_{M2}(T = 100$

mK)) varied with temperature. The lower inset to Figure A1 shows $\rho^{\parallel}(B)$ of the 1.15 μΩcm crystal in a limited range of field near B_{M2}, which increases from 5.8 T at $T = 100$ mK to 5.855 T at $T = 700$ mK. ΔB_{M2}, for both field-current orientations and for each of the three crystals, is listed in Table A2. For both orientations ΔB_{M2} is positive and, within errors, is independent of residual resistivity. ΔB_{M2} is significantly larger for $\rho^{\parallel}(B)$ than for $\rho^{\perp}(B)$.

ρ_{ab0} (μΩcm)	ΔB_M (T) for $\rho^{\parallel}(B)$	ΔB_M (T) for $\rho^{\perp}(B)$
1.15	-0.003±0.002	0.033±0.004
1.6	-0.005±0.002	0.012±0.003
2.7	-0.004±0.002	0.010±0.005

Table A1. ΔB_M of the three $Sr_3Ru_2O_7$ crystals.

ρ_{ab0} (μΩcm)	ΔB_{M2} (T) for $\rho^{\parallel}(B)$	ΔB_{M2} (T) for $\rho^{\perp}(B)$
1.15	0.055±0.008	0.013±0.004
1.6	0.055±0.005	0.016±0.006
2.7	0.059±0.007	0.011±0.005

Table A2. ΔB_{M2} of the three $Sr_3Ru_2O_7$ crystals.

For $B \perp I$ the variation of ΔB_{M2} with ρ_{ab0} is of particular interest in the context of ΔB_M (with the same field-current alignment). ΔB_M ($B \perp I$) of the 1.15 μΩcm sample is much larger than ΔB_M of the other two samples. However, on the basis of the three given values, any claim of a dependence on residual resistivity must be treated with caution: the large ΔB_M of the cleanest sample may be anomalous. The numbers in the final column of Table A2 do, however, lend support the numbers in Table A1: ΔB_{M2} (for $\rho^{\perp}(B)$) of the 1.15 μΩcm crystal does *not* seem to be anomalous with respect to ΔB_{M2} ($\rho^{\perp}(B)$) of the dirtier crystals. In principle the ΔB_{M2} ($\rho^{\perp}(B)$) value of the 1.15 μΩcm crystal may also be anomalous (and there may, therefore, be a genuine sensitivity of ΔB_{M2} to ρ_{ab0}, not revealed in the final column of Table A2) but this is improbable. It is unlikely, although not impossible, that some unknown factor could be responsible for inducing a false ρ_{ab0}-dependency into the ΔB_M data yet could

exactly cancel out an intrinsic ρ_{ab0}-dependence in the ΔB_{M2} data. Overall, the observation that ΔB_{M2} is independent of residual resistivity implies that the observation of a ρ_{ab0}-dependent ΔB_M is likely to be (but not certain to be) genuine.

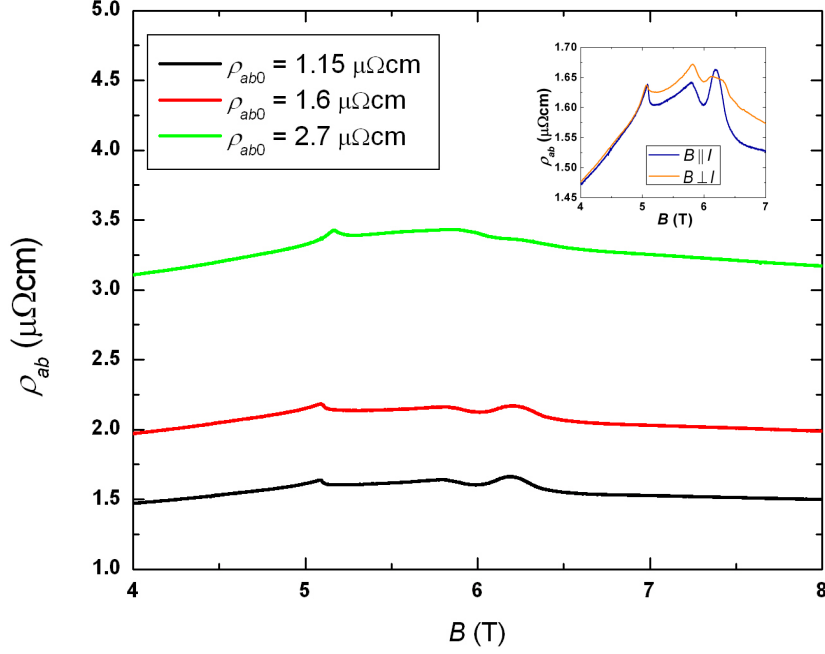**Figure A2. $\rho^{\parallel}(B)$ of three different Sr$_3$Ru$_2$O$_7$ crystals at $T = 100$ mK. The inset displays $\rho^{\parallel}(B)$ and $\rho^{\perp}(B)$ of the 1.15 μΩcm crystal, also at $T = 100$ mK.**

Figure A2 shows $\rho^{\parallel}(B)$ of three different Sr$_3$Ru$_2$O$_7$ crystals at $T = 100$ mK. Peaks in $\rho_{ab}(B)$ of each crystal at $B \sim 5.1$ and 5.8 T are clear. The high-field peak in $\rho^{\parallel}(B)$ of the 1.6 μΩcm sample, centred at 6.2 T, is broadened with respect to the equivalent peak in $\rho^{\parallel}(B)$ of the 1.15 μΩcm sample. A kink, rather than a peak, in $\rho^{\parallel}(B)$ of the 2.7 μΩcm sample is also seen at 6.2 T. It is therefore clear that the feature in $\rho^{\parallel}(B)$ centred about $B_{ab} = 6.2$ T is 'washed away' by crystalline disorder. This observation is consistent with the earlier study in ref.1.

$\rho^{\perp}(B)$ and $\rho^{\parallel}(B)$ of the 1.15 μΩcm crystal at $T = 100$ mK is shown in the inset to Figure A2. Sharp peaks in $\rho(B)$ are evident at fields of 5.1 and 5.8 T for both field orientations but the distinctive peak in $\rho^{\parallel}(B)$ at 6.2 T is suppressed when the in-plane magnetic field is aligned perpendicular to the current. Although the electronic mean

free path of this crystal is approximately 2.5 times less than the ultraclean crystals studied in ref. 2 an in-plane magnetoresistive anisotropy is still observed.

References

[1] R. S. Perry, T. Tayama, K. Kitagawa, T. Sakakibara, K. Ishida and Y. Maeno, J. Phys. Soc. Jpn. **74**, 1270 (2005)

[2] R. A. Borzi, S. A. Grigera, J. Farrell, R. S. Perry, S. J. S. Lister, S. L. Lee, D. A. Tennant, Y. Maeno and A. P. Mackenzie, Science **315**, 214 (2006)